

2002

Large eddy simulation of wall bounded turbulent flows with heat transfer

Yang Liu
Iowa State University

Follow this and additional works at: <https://lib.dr.iastate.edu/rtd>

 Part of the [Mechanical Engineering Commons](#)

Recommended Citation

Liu, Yang, "Large eddy simulation of wall bounded turbulent flows with heat transfer" (2002). *Retrospective Theses and Dissertations*. 17014.

<https://lib.dr.iastate.edu/rtd/17014>

This Thesis is brought to you for free and open access by the Iowa State University Capstones, Theses and Dissertations at Iowa State University Digital Repository. It has been accepted for inclusion in Retrospective Theses and Dissertations by an authorized administrator of Iowa State University Digital Repository. For more information, please contact digirep@iastate.edu.

**Large eddy simulation of wall bounded turbulent
flows with heat transfer**

by

Yang Liu

A thesis submitted to the graduate faculty
in partial fulfillment of the requirements for the degree of
MASTER OF SCIENCE

Major: Mechanical Engineering

Program of Study Committee:
Richard H. Pletcher (Major Professor)
John Tannehill
Gerald M. Colver
Gary Tuttle

Iowa State University

Ames, Iowa

2002

Copyright © Yang Liu, 2002. All rights reserved.

Graduate College
Iowa State University

This is to certify that the master's thesis of

Yang Liu

has met the thesis requirements of Iowa State University

Major Professor

For the Major Program

TABLE OF CONTENTS

NOMENCLATURE.....	X
ABSTRACT.....	xvii
CHAPTER 1. INTRODUCTION.....	1
1.1 Motivation.....	1
1.2 Literature Review of Large Eddy Simulation.....	4
1.3 Thesis Organization.....	8
CHAPTER 2. MATHEMATICAL FORMULATION AND FINITE VOLUME REPRESENTATION.....	10
2.1 Compressible Navier-Stokes Equations.....	10
2.2 Filtering.....	12
2.3 Favre Filtered Governing Equations.....	13
2.4 Subgrid Scale Model.....	16
2.4.1 Gradient-Diffusion Models.....	17
2.2.2 Smagorinsky Model.....	18
2.2.3 Isotropic Part of the SGS Model.....	19
2.2.4 Scale Similarity Model.....	20
2.2.5 Mixed Model.....	21
2.2.6 Dynamic Procedure.....	22
2.2.7 Localization Method for SGS Models.....	26
2.5 Integral-Vector Form of the Equations.....	28
2.6 Finite Volume Approach.....	32
2.7 Dependent Variables.....	33
2.8 Integral Approximations.....	33

2.9	Gradients.....	34
2.10	Low Mach Number Preconditioning.....	35
2.11	Lower-Upper Symmetric Gauss-Seidel.....	36
2.12	Convergence Criteria.....	42
2.13	Boundary Conditions.....	42
2.13.1	Solid Wall Boundary Conditions.....	42
2.13.2	Periodic Boundary Condition.....	43
2.13.3	Symmetry Boundary Condition.....	44
2.14.4	Thermal Boundary Condition.....	44
CHAPTER 3. LARGE EDDY SIMULATION OF		
INCOMPRESSIBLE TURBULENT FLOW IN A DUCT OF		
SQUARE CROSS-SECTION.....		46
3.1	Introduction.....	46
3.2	Problem Description.....	48
3.3	Simulation Details.....	52
3.4	Results and Discussion.....	56
3.4.1	Mean Velocity Field.....	56
3.4.2	Turbulent Statistics.....	66
3.5	Conclusions.....	73
CHAPTER 4. LARGE EDDY SIMULATION OF FULLY		
DEVELOPED TURBULENT ROTATING DUCT FLOWS.....		75
4.1	Introduction.....	75
4.2	Problem Description.....	76
4.3	Simulation Details.....	80
4.4	Results and Discussion.....	81
4.4.1	Effects of Rotation on Mean Flow Structure.....	81
4.4.2	Effects of Rotation on Turbulence Statistics.....	88
4.4.3	Effects of Reynolds Number on Rotating Duct Flow.....	93

4.5	Conclusions.....	96
CHAPTER 5. LARGE EDDY SIMULATION OF THE		
EFFECTS OF RIBS AND ROTATION ON HEAT		
TRANSFER IN A RIBBED CHANNEL.....98		
5.1	Introduction.....	98
5.2	Simulation Details.....	100
5.3	Results and Discussion.....	103
5.3.1	Effects of Ribs on Flow Field.....	103
5.3.2	Heat Transfer in a Ribbed Channel Without Rotation.....	106
5.3.3	Heat Transfer in a Ribbed Channel With Rotation.....	109
5.4	Conclusions.....	114
CHAPTER 6. CONCLUSIONS.....115		
6.1	Summary.....	115
6.2	Recommendations for Future Work.....	117
APPENDIX A JACOBIAN MATRICES.....118		
APPENDIX B DISCRETE TEST FILTERS.....120		
BIBLIOGRAPHY.....123		
ACKNOWLEDGEMENTS.....136		

LIST OF TABLES

Table 3.1	Simulation domain dimensions and grid sizes.....	55
Table 4.1	Case description for rotating duct simulation.....	80
Table 5.1	Case summary for ribbed channel simulation.....	103

LIST OF FIGURES

Figure 2.1	Typical ghost cell.....	41
Figure 3.1	Geometry of the domain.....	49
Figure 3.2	Mesh of a quadrant of the cross-section.....	53
Figure 3.3	Mean streamwise velocity along the bisector A.....	58
Figure 3.4	u^+ distribution with respect to logarithmic coordinate.....	59
Figure 3.5	Contours of streamwise velocity normalized by friction velocity.....	61
Figure 3.6	Secondary flow field in the cross-section.....	61
Figure 3.7	Streamwise velocity contour and secondary flow field in a quadrant.....	62
Figure 3.8	Friction velocity distribution along the wall.....	63
Figure 3.9	Instantaneous secondary flow field.....	65
Figure 3.10	u_{rms} along the bisector A, $Re_h = 6000$	67
Figure 3.11	u_{rms} along the bisector A in wall units for $Re_h = 6000$	68
Figure 3.12	u_{rms} along the bisector A, $Re_h = 8000$	68
Figure 3.13	u_{rms} along the bisector A in wall units for $Re_h = 8000$	69
Figure 3.14	v_{rms} along the bisector A, $Re_h = 6000$	69
Figure 3.15	v_{rms} along the bisector A, $Re_h = 8000$	70
Figure 3.16	w_{rms} along the bisector A, $Re_h = 6000$	70
Figure 3.17	w_{rms} along the bisector A, $Re_h = 8000$	71
Figure 3.18	Contour of $\overline{u'v'}$ in the cross section.....	72

Figure 4.1	Geometry of the domain.....	77
Figure 4.2	Streamwise velocity along bisector B for $Ro = 0.048$	84
Figure 4.3	Streamwise velocity along bisector B for $Ro = 0.144$	84
Figure 4.4	Friction velocity distributions for $Ro = 0.048$	85
Figure 4.5	Friction velocity distributions for $Ro = 0.144$	85
Figure 4.6	Streamwise velocity contours in the cross-section for $Ro = 0.048$	86
Figure 4.7	Secondary flow in the cross-section for $Ro = 0.048$	86
Figure 4.8	Streamwise velocity contours in the cross-section for $Ro = 0.144$	87
Figure 4.9	Secondary flow in the cross-section for $Ro = 0.144$	87
Figure 4.10	Distributions of turbulence intensities along bisector B for $Ro = 0.048$	89
Figure 4.11	Distributions of turbulence intensities along bisector B for $Ro = 0.144$	90
Figure 4.12	Contour of $\overline{u'v'}$ for $Ro = 0.048$	91
Figure 4.13	Contour of $\overline{u'v'}$ for $Ro = 0.144$	92
Figure 4.14	Streamwsie velocity along bisector B.....	94
Figure 4.15	u_{rms} along the bisector B.....	94
Figure 4.16	v_{rms} along the bisector B.....	95
Figure 4.17	w_{rms} along the bisector B.....	95
Figure 4.18	$\overline{u'v'}$ along the bisector B.....	96
Figure 5.1	Schematic of the computational domain for the ribbed channel.....	100
Figure 5.2	Streamlines in the incompressible non-rotating ribbed channel.....	104

Figure 5.3	Contour of turbulent kinetic energy in incompressible non-rotating ribbed channel.....	105
Figure 5.4	Nusselt number distribution along the channel.....	108
Figure 5.5	Wall temperature distribution along the channel.....	108
Figure 5.6	Velocity field in rotating compressible ribbed channel.....	110
Figure 5.7	Streamlines in rotating compressible ribbed channel.....	110
Figure 5.8	Turbulent kinetic energy in compressible rotating ribbed channel.....	111
Figure 5.9	Distribution of Nu along the ribbed channel with heat transfer and system rotation.....	112
Figure 5.10	Distribution of wall temperature along the ribbed channel with heat transfer and system rotation.....	113

NOMENCLATURE

Roman Symbols

$[A],[B],[C]$	inviscid flux Jacobians
A_c	channel and duct cross-sectional area ($= L_y L_z$)
C	discretized convective and viscous flux vector
C_d, C_i	dynamic subgrid-scale model coefficients
C_s	Smagorinsky subgrid-scale model coefficient
c_p	constant pressure specific heat
c_v	constant volume specific heat
D	height of duct ($= 2\sigma$)
D_h	hydraulic diameter
E	specific total energy ($= e + u_i u_i / 2$)
E, F, G	flux vectors
$E(k)$	turbulent energy spectrum
e	specific internal energy ($= c_v T$)
f	friction coefficient
G	filter function
g	gravitational constant
H	total enthalpy ($= h + u_i u_i / 2$), or channel height ($= 2\sigma$)

h	rib height, heat transfer coefficient or specific enthalpy
$\vec{i}, \vec{j}, \vec{k}$	unit vectors
K	subgrid-scale term in energy equation
k	thermal conductivity or turbulent kinetic energy
$[L], [D], [U]$	approximate factorization matrices for LU-SGS scheme
L_{ij}	resolved or Leonard turbulent stress tensor
L_r	reference length
L_x, L_y, L_z	dimensions of the channel or duct
m	pseudo time index
\dot{m}	mass flow rate
Nu	generic Nusselt number
Nu_D	Nusselt number based on hydraulic diameter ($= hD_h/k$)
n	physical time index
\vec{n}	unit normal vector
n_x, n_y, n_z	components of unit normal vector
P	rib spacing or pitch or perimeter of the duct
Pr	Prandtl number ($= \mu c_p/k$)
Pr_t	turbulent Prandtl number
p	thermodynamic pressure
\mathbf{Q}_j	subgrid-scale turbulent heat flux vector
q_j	heat flux vector
q^2	subgrid-scale turbulent kinetic energy
R	gas constant
\mathbf{R}	residual vector
\mathfrak{R}	preconditioned residual vector

Ra	Rayleigh number
Re	generic Reynolds number
Re_b	bulk Reynolds number based on duct height ($= \rho_b u_b D / \mu_b$)
Re_D	bulk Reynolds number based on hydraulic diameter ($= \rho_b u_b D_h / \mu_b$)
Re_H	bulk Reynolds number based on channel height ($= \rho_b u_b H / \mu_b$)
Re_r	Re based on reference quantities ($= \rho_r u_r L_r / \mu_r$)
Re_δ	bulk Reynolds number based on half channel height ($= \rho_b u_b \delta / \mu_b$)
r_A, r_B, r_C	relaxation factors in LU-SGS scheme
S	magnitude of cell face area vector
\vec{S}	cell face area vector
S_{ij}	strain rate tensor
T	thermodynamic temperature
$[T]$	time derivative Jacobian ($= \partial U / \partial W$)
TKE	turbulent kinetic energy
t	physical time
t_e	large eddy turnover time ($= \delta / u_\tau$)
U	contravariant velocity
U	vector of conserved variables ($\rho, \rho u, \rho v, \rho w, \rho E$) ^T
u_τ	friction velocity ($= \tau_w / \rho_w$)
u, v, w	Cartesian velocity components in x, y, z directions
u^+	velocity in wall coordinates ($= u / u_\tau$)
V_r	reference velocity

W	vector of primitive variables $(p, u, v, w, T)^T$
x, y, z	Cartesian coordinates
y^+	distance to wall in wall coordinates $(= \delta_y u_\tau / \nu_w)$

Greek Symbols

α, π, ε	subgrid-scale terms in energy equations
β	pressure gradient parameter
$\beta_x, \beta_y, \beta_z$	scale factors in implicit residual averaging
Γ	time derivative preconditioning matrix
γ	ratio of specific heats
$\gamma_A, \gamma_B, \gamma_c$	eigenvalue scaling factors in LU-SGS scheme
Δ	grid filter width
Δ_t	test filter width
δ	channel half height
θ	temperature difference $(T_w - T)$
μ	molecular dynamic viscosity
μ_t	subgrid-scale turbulent viscosity
ν	molecular kinematic viscosity $(= \mu / \rho)$
ν_t	subgrid-scale turbulent kinematic viscosity $(= \mu_t / \rho)$
ρ	thermodynamic density
σ_{ij}	shear stress tensor
τ	pseudo time

τ_{ij}	subgrid-scale stress tensor
t_{ij}	solution-grid turbulent stress
T_{ij}	test-grid turbulent stress
Φ	temperature gradient parameter
Ω	cell volume
ω	relaxation factor in LU-SGS scheme

Subscripts

b	bulk property
con	conduction contribution
g	ghost cell quantity
i	inviscid contribution
i, j, k	indices for Cartesian coordinates
nw	near wall cell quantity
p	periodic component
r	reference quantity
res	resolved contribution
rms	root-mean-square
s or sgs	subgrid-scale contribution
v or vis	viscous contribution
w	wall value
x, y, z	associated with Cartesian direction
β	cell face index
ξ, η, ζ	associated with i, j, k directions

Superscripts and Other Symbols

*	dimensional variable
+	wall coordinates
'	fluctuations with respect to ensemble average, or subgrid-scale component or filtered quantity
"	fluctuations with respect to Favre ensemble average, or subgrid-scale component or Favre filtered quantity
→	vector quantity
–	large scale component of filtered quantity
~	large scale component of Favre filtered quantity
^	quantity that is nonlinear function of Favre filtered quantities
≅	test filtered quantity
$\langle \rangle$	ensemble averaged quantity
$\langle \rangle_x$	ensemble average in x directions
$\langle \rangle_z$	ensemble average in z directions
$\langle \rangle_t$	ensemble average in time

Abbreviations

<i>CFD</i>	computational fluid dynamics
<i>DNS</i>	direct numerical simulation
<i>FD</i>	finite difference

<i>FV</i>	finite volume
<i>LES</i>	large eddy simulation
<i>LU – SGS</i>	lower-upper symmetric-Gauss-Seidel
PVM	parallel virtual machine
<i>MPI</i>	message passing interface
<i>RANS</i>	Reynolds-averaged Navier-Stokes
<i>SGS</i>	subgrid-scale

ABSTRACT

In this thesis work, large eddy simulation was used to study a variety of wall-bounded turbulent flows using a compressible finite volume formulation. The features of this formulation include time derivative preconditioning, an implicit lower-upper symmetric Gauss-Seidel scheme, and parallelization using the message passing interface (MPI). Subgrid scale terms in both momentum and energy equations were modeled dynamically. Furthermore, due to the inhomogeneity of wall-bounded flows, the model was further localized to better represent the physics of the problem.

The localized dynamic model was first applied to study the incompressible turbulent flow through a duct with square cross-section. Mean flow, law of the wall, and turbulence statistics were compared with the benchmark results of direct numerical simulation and excellent agreement was achieved. The secondary flow of Prandtl's second kind in the cross-section was captured through the simulation. It is composed of four pairs of counter-rotating cells. The interaction between the mean flow field and the secondary flow field creates some important features and they were studied in this work.

Based on the work of incompressible duct flow, system rotation was applied to investigate the effects of rotation on the turbulent flow field. The spanwise system rotation was found to suppress turbulence production and reduce the turbulence level on the leading side, while enhancing turbulence production and increasing the turbulence level on the trailing side. In the global sense, rotation decreases the turbulent kinetic energy significantly. Because of the rotation, the secondary flow field in non-rotating duct was found to be diminished at weaker rotation and even eliminated at stronger rotation. Instead, a pair of counter rotating cells called Taylor-

Görtler vortices, as well as the Taylor-Proudman regime, were found to exist in the cross-section, which is consistent with the results in the literature.

Large eddy simulation was also applied to investigate the effects of ribs and system rotation on heat transfer in a channel. It was found that a rib creates a larger recirculation zone on the rear side and a smaller recirculation zone on the front side. The turbulence level was at its maximum near the ribs. The existence of ribs enhances heat transfer significantly over the plane channel, as well as creates a low-heat-transfer-coefficient region in the recirculation zones. This means a balance is needed between global enhancement and local suppression. With system rotation, heat transfer is greatly enhanced on the trailing side, while significantly reduced on the leading side.

CHAPTER 1. INTRODUCTION

1.1 Motivation

Turbulence refers to the extremely complicated motions in fluids, which usually are unsteady, irregular, and three-dimensional. Turbulence can be observed in our everyday life such as in the water torrent in the river or the gas flow out of a chimney. It is the prevalent mode of motion in fluids. In other words, turbulence is the rule, rather the exception. It accounts for the majority of the transport of mass, momentum and heat in the fluid, which makes itself a two-fold sword. For heat exchanger designers who wish to achieve heat transfer coefficients as large as possible, turbulence is ensured by adding turbulence promoters. On the other hand, aircraft designers may wish to decrease the turbulence level around the plane body and wings so that drag over the plane can be decreased, which leads to a huge amount of savings in costs. So under different situations, it is desired to either enhance or suppress turbulence. The prerequisite of this is a deep and comprehensive understanding of the physics of turbulence.

According to Lumley (1996), “man has been curious about turbulence for at least 500 years, and has been actively trying to understand it for a little over 100”. However, even in this modern era, our knowledge of turbulence is still very primitive. Up to now, analytical solutions of turbulent flows are only available for very simple flows, such as homogeneous decaying turbulence, which have very little practical applications in engineering. Fortunately, the development of computers, especially in the recent twenty years, has enabled us to gain valuable insights into the phenomena and mechanisms of turbulence. Now, it is possible to conduct ‘numerical experiments’ on turbulent flow and heat transfer problems by using a personal

computer, workstation, or supercomputer depending on the nature of the problem. Meanwhile, the trend is now clear that both industry and academia will rely more and more on the capability brought by simulation.

Bardina et al. (1980) classified the approaches to predicting turbulent flows in the following six sub-categories:

- The first involves the use of correlations such as the friction factor as a function of the Reynolds number or the Nusselt number for heat transfer as a function of the Reynolds and Prandtl numbers. This method is useful but limited to simple types of flows where designers only care about the simple characteristics of the flow as mentioned above.
- The second uses integral equations that can be derived from the equations of motion by integrating over one or more coordinates using approximate profiles. Usually this reduces the problem to one or more ordinary differential equations that are easily solved.
- The third is based on equations obtained by averaging the equations of motion over time (if the flow is statistically steady), over a coordinate in which the mean flow does not vary, or over an ensemble of realizations (an imagined set of flows in which all controllable factors are kept fixed). This approach is called one-point closure and leads to a set of partial differential equations called the Reynolds averaged Navier-Stokes (RANS) equations. However, these equations do not form a closed set themselves and the introduction of some sort of approximations has to be made to close the modelling problem.
- The fourth set of methods is called two-point closures and uses equations for the correlations of velocity components at two distinct points or, more often, the Fourier transform of these equations.
- The fifth is large eddy simulation (LES), in which large scale motions are solved while small scale motions are modeled. Since this method is the focus of this thesis, it will be further explained in the following paragraphs.

- The sixth, and the last one, is the direct numerical simulation (DNS). This method solves the Navier-Stokes equations fully without any compromise and all scales of motions of turbulent flows are decomposed in the computation. So these computations will be able to obtain all the information that is carried by the flow.

As one progresses down the list, more and more information can be gained by the computation and fewer approximations are made. The fifth method of the list, large eddy simulation, is the focus of this thesis and will be discussed here.

According to Hartel (1996), the concept of LES relies on two facts of turbulent flows. Firstly, most of the global features of turbulent flows, such as averaged mixing rates or averaged losses, are governed by the dynamics of the largest scales and depend only little on the small-scale turbulence. From the practical point of view, just the large-scale information is of major interest and usually simulation of large scales will be able to provide enough information for general purposes. On the other hand, the small-scale turbulence, especially at high Reynolds numbers, becomes independent of the strong inhomogeneities of the energy-containing eddies and tends to be locally isotropic due to the viscous effects. For this reason, models for small-scale turbulence should be much simpler than those in the statistical simulation. Since the large scales are computed explicitly, which accounts for the majority of the energy and information of the flow, the small-scale turbulence models will be more universally applicable. The difference between large-scale and small-scale turbulence is not absolute. One of the criteria requires that large scales contain 80% to 90% of the kinetic energy, while small scales account for 80% to 90% of the viscous dissipation (Ferziger, 1977).

So it can be seen that the LES approach is at an intermediate position between DNS and statistical simulations based on RANS equations. Computationally LES is obviously less costly than DNS. However, it is usually much more expensive than statistical simulations of the same flow. This is because LES is trying to capture the

details of turbulence, which in nature are always three-dimensional and transient, although they could be only two- or one-dimensional on the average and be statistically steady. What is more, large eddy simulation, like DNS, needs to be conducted over long periods of time to obtain stable and significant statistics. So the application of LES should prove most fruitful for the analysis of complex three-dimensional flows and time-dependent problems where statistical simulations usually fail. It is expected that with LES, some further information can be obtained over that obtained from the statistical simulations.

The motivation of this research is to extend the regime of LES into flows bounded by walls with the consideration of complex geometry, system rotation, heat transfer, and variable properties. The flows can be either partially or fully bounded by the wall, which creates inhomogeneities in the flows and difficulty for the simulation. It is expected that LES should perform well even under these difficult conditions. Practical applications of such simulations include guiding the design of internal cooling passages of the gas turbine blade, heat exchangers and electronic cooling devices.

1.2 Literature Review of Large Eddy Simulation

Large eddy simulation was originally developed and applied for three-dimensional and time-dependent simulations of atmospheric flows (Smagorinsky, 1963). Its first application to engineering problem was to the incompressible turbulent channel flow in the study of Deardorff (1970). Since these forerunning investigations, a lot of work has been done to expand both the capabilities and applications of LES. In this section, a brief survey will be presented on the development of LES, especially for the recent 20 years. Since direct numerical simulation is closely related to LES, some DNS work has also been addressed in the survey. This survey is mainly concerned about the studies conducted using LES since its birth, and does not intend

to be a summary of its development of fundamental principles and future trends. Reviews by Ferziger (1996), Hartel (1996), and Moin (1996) are excellent examples of the latter.

Fundamental studies using LES logically began with homogeneous turbulence. Large eddy simulations of incompressible homogeneous turbulence were performed by Bardina et al. (1980), Dang (1985), Lesieur and Rogallo (1989), Chasnov (1991), Moin et al. (1991), and Metais and Lesieur (1992). Homogeneous incompressible turbulence suddenly exposed to system rotation was studied using LES by Bardina et al. (1985), Dang and Roy (1985a), and Squires (1993). Another homogeneous flow that was extensively studied by large eddy simulation is incompressible turbulence subject to homogeneous shear. Large eddy simulations of this problem were made by Cambaon et al. (1981), Dang (1985), Dang and Roy (1985b), Aupoix (1986), and Laurence (1986).

An unbounded but inhomogeneous turbulent flow that has repeatedly been investigated is the turbulent mixing layer. Large eddy simulations of mixing layers were conducted by Mansour et al. (1978), Marayuma (1988), and Comte et al. (1990) for incompressible flow. And by Leith (1990), Ragab and Sheen (1991), and Sheen et al. (1993) for compressible flow. Further large eddy simulations of the compressible mixing layer were performed by Vremen et al. (1994). Closely related to the turbulent mixing layer is the turbulent jet, which was studied using LES by Baron and Laurence (1983), Pourquie and Eggels (1993), and Voke and Gao (1993).

The majority of the more recent investigations have been concerned with wall-bounded turbulent flows in various geometries. For example, Biringen and Reynolds (1981) used large eddy simulation to study incompressible decaying turbulence in the presence of a solid wall: the so-called "shear-free" boundary layer. Large eddy simulations of "regular" incompressible boundary layers were conducted by Schmitt and Friedrich (1984), Esmaili and Piomelli (1992), and Mason and Thomson (1992). Direct numerical simulations of turbulent boundary layers were reported by Spalart (1988) and Spalart and Watmuff (1993) for incompressible flows, and by Guo and

Adams (1994) for supersonic flows. Large eddy simulations of a supersonic boundary layer were conducted by Kral and Zang (1992). Further studies on turbulent boundary layers were concerned with the flow over curved walls. For instance, Friedrich and Su (1982) and Moin et al. (1994) performed large eddy simulations of an incompressible boundary layer with longitudinal curvature. A direct numerical simulation of transversely curved boundary layer was presented by Neves et al. (1992).

A very extensive application of DNS and LES has been directed toward the simulation of turbulent flow in a plane channel. Large eddy simulations of this flow were conducted, among many others, by Deardorff (1970), Schumann (1973, 1975), Moin and Kim (1982), Horiuti (1985), Mason and Callen (1986), Piomelli et al. (1989), Yakhov et al. (1989), Germano et al. (1991), Hartel and Kleiser (1992), and Hartel et al. (1994). Direct numerical simulations of turbulent channel flows were reported by Kim et al. (1987), Gilbert and Kleiser (1991), and Hartel, et al. (1994). More recent research on channel flow took into account the heat transfer using compressible formulations. The plane channel flow with variable properties was calculated using LES by Wang and Pletcher (1996), Dailey and Pletcher (1998), and Meng et al. (2000), and using DNS by Nicoud (1998).

Several flow problems that are closely associated with plane channel flow have occasionally been addressed in the past. Examples are the flow in a straight pipe, which was investigated by Unger and Friedrich (1993) using LES, and by Eggels et al. (1994) using DNS, and the flow in an annular tube by Schumann (1975) and Grotzbach (1987). Another related problem is the flow in a rotating channel, which was investigated using LES by Kim (1983) and Piomelli and Liu (1995). Direct numerical simulations of rotating channel flow were reported by Kristoffersen and Andersson (1993) and Piomelli and Liu (1995).

Turbulent flows in a square duct represent a more difficult problem than those in a plane channel. The flows are bounded in two directions and are more inhomogeneous than channel flow. With the addition of heat transfer and system rotation, the flow can become totally inhomogeneous in all three directions. Large eddy simulations of

incompressible duct flows were performed by Madabhushi and Vanka (1991), Balaras and Benocci (1994), and Su and Friedrich (1994); DNS results for this flow were reported by Gavrilakis (1992) and Huser and Biringen (1993). Meanwhile, turbulent duct flow under system rotation has been studied by Pallares and Davidson (2000), and under both rotation and heat transfer by Murata and Mochizuki (2000, 2001).

A more complex flow problem that was studied by a number of authors is the flow over a backward-facing step. This flow exhibits several complicated features such as solid wall, separation, and reattachment. Moreover, for this problem a careful choice of suitable inflow and outflow boundary conditions is of particular importance. Large eddy simulations of the backward-facing step flow were reported by Friedrich and Arnal (1990), Karniadakis et al. (1990), Morinishi and Kobayashi (1990), Silveira Neto et al. (1990), Akselvoll and Moin (1993), and Avancha (2001). DNS studies of this flow were performed by Lee and Moin (see Akselvoll and Moin, 1993). Related problems are the sudden expansion, which was studied using DNS by Wagner and Friedrich (1994), and the flow of the confined coannular jet, which was investigated by Akselvoll and Moin (1995) using LES. Another type of flow where separation plays a key role, but where boundary conditions can be chosen in a natural way, is the driven cavity flow. LES studies of this problem were conducted by Jordan and Ragab (1993), who also performed a direct numerical simulation, and by Zang et al. (1993). Further examples of the applications of LES to more complex problems are the flow over square ribs, which was studied by Werner and Wengle (1989) and Yang and Ferziger (1993), and the flow over and around a cube in a plane channel which was studied by Kobayashi et al. (1984), He and Song (1993), and Werner and Wengle (1993). In addition to the simulation of the flow around a tube, He and Song (1993) presented LES results for several other interesting applications including diffuser flows or flows in bifurcation pipes and draft tubes which are used in power engineering. Another more complex application of LES is the flow around turbulence-control devices (LEBU devices) which was studied by Klein and Friedrich

(1990). Typical examples of recent DNS applications for more complex problems are the flow over surface-mounted riblets, which was simulated by Chu et al. (1992) and Choi et al. (1993), and the grooved-channel flow by Amon (1992).

It is worth mentioning here that the expansion of applications of LES has been accompanied by the development of the models for small-scale turbulence, or so called subgrid scale models, which is the enabling factor for large eddy simulation and its major difference from direct numerical simulation. The first subgrid scale model for LES was introduced by Smagorinsky (1963) around 40 years ago. And Bardina (1980) proposed the scale similarity model for small-scale turbulence. Based on these two models, a lot of variants have been developed and made. One of the most noteworthy is by Germano et al. (1990), who introduced the first dynamic subgrid scale model based on the Smagorinsky model which greatly enhances the capability of LES. Based on the same idea, Zang et al. (1993) developed a dynamic procedure for the scale similarity model. In recent years, a lot of work has been done to improve the capability of the models by researchers, such as Ghosal et al. (1995), Piomelli and Liu (1995) and Horiuti (1997). These will be discussed in further details in Chapter 2 of this thesis.

1.3 Thesis Organization

Chapter 2 of this thesis contains the mathematical formulation for the LES of compressible turbulent flows. Favre filtered variables are used for non-dimensional compressible Navier-Stokes equations. An integral-vector form is illustrated to facilitate the development of the finite volume formulation, which is also given in this chapter. The numerical scheme, together with the discretization method, are presented briefly. Formulation of subgrid scale model is discussed and a short review of subgrid scale models is also included.

The simulation results of incompressible turbulent duct flow are presented in Chapter 3. A localized dynamic subgrid scale model was used to account for the subgrid scale effects, which is one of the major contributions of this thesis. The characteristics of turbulent duct flow are discussed in detail, with an emphasis on the phenomena and mechanisms of secondary flow, which is the major difference of the duct flow from the plane channel flow. The results are compared with the DNS results of Gavrilakis (1992).

Chapter 4 reports on the incompressible turbulent duct flow under system rotation. The discussion is mainly on the effects of Coriolis force together with the secondary flow. Since there are no detailed DNS or experimental results available at the Reynolds number of this work, no comparison can be made at this stage.

In Chapter 5, results of rotating rib-roughened channel flow with heat transfer are reported. The subgrid scale heat transfer effect is also taken into account by subgrid scale models. Effects of rotation and ribs are discussed to show their influence on the heat transfer in the system, as well as the hydrodynamic characteristics of the flow.

The thesis is summarized in Chapter 6, with the significant contributions of this work listed. Finally, the recommendations for future work are given.

CHAPTER 2. MATHEMATICAL FORMULATION AND FINITE VOLUME REPRESENTATION

In this chapter, the governing equations of LES are developed. The subgrid scale models necessary to close the system of equations are discussed. The equations are recast in integral-vector form, which is the basis for discretizing the partial differential equations into algebraic ones using the finite volume technique. Then the finite volume formulation used for this research is described. The spatial and temporal discretization procedures are explained in detail.

2.1 Compressible Navier-Stokes Equations

The conservation of mass, momentum, and energy is expressed as

$$\frac{\partial \rho}{\partial t} + \frac{\partial(\rho u_j)}{\partial x_j} = 0 \quad (2.1)$$

$$\frac{\partial(\rho u_i)}{\partial t} + \frac{\partial(\rho u_i u_j)}{\partial x_j} = -\frac{\partial p}{\partial x_i} + \frac{\partial \sigma_{ij}}{\partial x_j} \quad (2.2)$$

$$\frac{\partial(\rho E)}{\partial t} + \frac{\partial(\rho E u_j)}{\partial x_j} = -\frac{\partial(p u_j)}{\partial x_j} - \frac{\partial q_j}{\partial x_j} + \frac{\partial(\sigma_{ij} u_i)}{\partial x_j}, \quad (2.3)$$

where the total specific energy is $E = e + \frac{1}{2} u_i u_i$. The variables in above equations have been nondimensionalized with respect to dimensional reference quantities, denoted with a subscript r, as

$$x_i = \frac{x_i^*}{L_r} \quad t = \frac{t^*}{L_r/V_r} \quad u_i = \frac{u_i^*}{V_r} \quad (2.4)$$

$$p = \frac{p^*}{\rho_r V_r^2} \quad \rho = \frac{\rho^*}{\rho_r} \quad T = \frac{T^*}{T_r} \quad e = \frac{e^*}{V_r^2} \quad (2.5)$$

$$R = \frac{R^*}{V_r^2/T_r} \quad c_p = \frac{c_p^*}{V_r^2/T_r} \quad c_v = \frac{c_v^*}{V_r^2/T_r} \quad \mu = \frac{\mu^*}{\mu_r} \quad (2.6)$$

Dimensional variables are denoted with a superscript asterisk, and all other variables are nondimensional.

For a Newtonian fluid, the shear stress tensor is

$$\sigma_{ij} = \frac{2\mu}{\text{Re}_r} (S_{ij} - \frac{1}{3} S_{kk} \delta_{ij}), \quad (2.7)$$

where the strain rate tensor is

$$S_{ij} = \frac{1}{2} \left(\frac{\partial u_i}{\partial x_j} + \frac{\partial u_j}{\partial x_i} \right), \quad (2.8)$$

and the Reynolds number based on reference quantities is $\text{Re}_r = \rho_r V_r L_r / \mu_r$. Equation (2.7) makes use of Stokes' hypothesis, $\lambda + \frac{2}{3}\mu = 0$, where λ is the coefficient of bulk viscosity.

The heat flux vector is given by Fourier's law of heat conduction as

$$q_j = -\frac{c_p}{\text{Re}_r} \frac{\mu}{\text{Pr}} \frac{\partial T}{\partial x_j}, \quad (2.9)$$

where the molecular Prandtl number is $\text{Pr} = \mu^* c_p^* / k^*$ and the reference Mach number is $M_r = V_r / \sqrt{\gamma R^* T_r}$.

For an ideal gas, the pressure, temperature, and density are related by the equation of state as

$$p = \rho R T = \frac{\rho T}{\gamma M_r^2} = (\gamma - 1) \rho e \quad (2.10)$$

For air, the nondimensional molecular viscosity is given as a function of temperature by Sutherland's law as

$$\mu = \frac{1+S}{T+S} T^{\frac{3}{2}} \quad S = \frac{S^*}{T_r}, \quad (2.11)$$

where $S^* = 111K$, or by the power law as

$$\mu = T^n, \quad (2.12)$$

where typically $n = 0.7$. Sutherland's law is slightly more accurate over a large temperature range, but the power law is less computationally demanding. The power law molecular viscosity was used for the research reported in this thesis. A perfect gas was assumed such that the specific heat capacities, c_p and c_v , were constants, and the molecular Prandtl number was assumed to have a constant value of 0.71.

2.2 Filtering

To separate the large scales from the small scales, a filter is defined as

$$\bar{f}(x, t) = \int_D f(x', t) G(x, x'; \bar{\Delta}) dx', \quad (2.14)$$

where D is the entire domain, G is the filter function, and $\bar{\Delta}$ is the filter width, i.e., the wavelength of the smallest scale retained by the filtering operation. The filter function determines the size and structure of the small scales that will be modeled.

The most commonly used filters for LES are the spectral cut-off filter, Gaussian filter, and top-hat filter. The simplest is the spectral cut-off filter, defined in wavenumber space, or \vec{k} space, as

$$\begin{aligned} G(\vec{k}) &= 1 \quad \text{for } |k_i| < k_c \\ G(\vec{k}) &= 0 \quad \text{for } |k_i| > k_c, \end{aligned} \quad (2.15)$$

where k_c is the cut-off wavenumber, and k_i is the i th component of the wavenumber vector \vec{k} . This filter eliminates the contributions of the high wavenumbers (or small scales). It is used often with spectral methods; however, it is difficult to implement

for finite difference or finite volume methods because it is not easily defined in physical space.

The Gaussian filter is preferred by some researchers because it approximates the cut-off filter, yet has very similar definitions in both wavenumber and physical space. In physical space, it is given by

$$G(\vec{x}, \vec{\xi}) = \left[\frac{\sqrt{c/\pi}}{\Delta} \right]^n \exp \left\{ - \left[\frac{\sqrt{c}}{\Delta} \right]^n (\vec{x} - \vec{\xi})^2 \right\}, \quad (2.16)$$

where c is constant, Δ is the filter width, and n is the number of dimensions to be filtered. In wavenumber space, the same filter is

$$G(\vec{k}) = \exp \left[- \frac{\Delta^2 k^2}{4c} \right], \quad (2.17)$$

where k is the magnitude of wavenumber vector, \vec{k} .

The top-hat, or box filter, is defined in physical space as

$$\begin{aligned} G(\vec{x}, \vec{\xi}) &= 1/\Delta^3 && \text{for } |x_i - \xi_i| \leq \Delta/2 (i=1, 2, 3) \\ G(\vec{x}, \vec{\xi}) &= 0 && \text{for } |x_i - \xi_i| > \Delta/2 (i=1, 2, 3) \end{aligned} \quad (2.18)$$

The top-hat filter, which was used in this thesis work, reduces to volume averaging, and is the logical choice for LES employing finite volume methods.

2.3 Favre Filtered Governing Equations

The filtering operation discussed above can be applied to the governing equations.

If G is a function of $\vec{x} - \vec{\xi}$ only, differentiation and filtering operation commute for uniform grids (Leonard, 1974).

$$\overline{\frac{\partial f}{\partial t}} = \frac{\partial \overline{f}}{\partial t}, \quad \overline{\frac{\partial f}{\partial x}} = \frac{\partial \overline{f}}{\partial x} \quad (2.19)$$

Ghosal et al. (1995) pointed out that when stretched grids are used, the operation of differentiation does not exactly commute, and a small approximation is introduced.

This leads to the following set of filtered governing equations

$$\frac{\partial \overline{\rho}}{\partial t} + \frac{\partial (\overline{\rho u_i})}{\partial x_i} = 0 \quad (2.20)$$

$$\frac{\partial \overline{\rho u_i}}{\partial t} + \frac{\partial \overline{\rho u_i u_j}}{\partial x_j} = -\frac{\partial \overline{p}}{\partial x_i} + \frac{\partial \overline{\sigma_{ij}}}{\partial x_j} \quad (2.21)$$

$$\frac{\partial \overline{\rho E}}{\partial t} + \frac{\partial \overline{\rho E u_j}}{\partial x_j} = -\frac{\partial \overline{\rho u_j}}{\partial x_j} - \frac{\partial \overline{q_j}}{\partial x_j} + \frac{\partial \overline{\sigma_{ij} u_i}}{\partial x_j}, \quad (2.22)$$

where

$$\overline{\sigma_{ij}} = \frac{2\mu}{\text{Re}_r} \overline{(S_{ij} - \frac{1}{3} S_{kk} \delta_{ij})}, \quad (2.23)$$

$$\overline{q_j} = -\frac{c_p \mu}{\text{Re}_r \text{Pr}} \frac{\partial \overline{T}}{\partial x_j}, \quad (2.24)$$

and the equation of state becomes

$$\overline{p} = R \overline{\rho T}. \quad (2.25)$$

For compressible flows, it is advantageous to use the filter introduced by Favre (1983), defined by

$$\tilde{f} = \frac{\overline{\rho f}}{\overline{\rho}}, \quad (2.26)$$

which implies the decomposition $f = \tilde{f} + f''$, where \tilde{f} is the resolved component, and f'' is the unresolved component. The Favre filtering yields the flow variables $\tilde{u}, \tilde{v}, \tilde{w}, \tilde{T}$, and \tilde{p} . The fact that \tilde{p} is used and not $\tilde{\rho}$ may appear confusing, but is a natural result from filtering the Navier-Stokes equations and re-organizing it by the definition of Favre-averaging.

It should be added that some relationships between variables in filtering are distinct from those used in Reynolds averaging. One distinction is that, in general, a Favre averaged variable, \bar{f} is not independent of the filtering operation, that is

$$\bar{\tilde{f}} = \frac{\overline{\rho \tilde{f}}}{\bar{\rho}} \neq \tilde{f} \quad (2.27)$$

Consequently, the Favre filtered governing equations are

$$\frac{\partial \bar{\rho}}{\partial t} + \frac{\partial \bar{\rho} \tilde{u}_i}{\partial x_i} = 0 \quad (2.28)$$

$$\frac{\partial \bar{\rho} \tilde{u}_i}{\partial t} + \frac{\partial \bar{\rho} \tilde{u}_i \tilde{u}_j}{\partial x_j} = -\frac{\partial \bar{p}}{\partial x_i} + \frac{\partial \hat{\sigma}_{ij}}{\partial x_j} - \frac{\partial \tau_{ij}}{\partial x_j} \quad (2.29)$$

$$\frac{\partial \bar{\rho} \hat{E}}{\partial t} + \frac{\partial \left[(\bar{\rho} \hat{E} + \bar{p}) \tilde{u}_j \right]}{\partial x_j} = -\frac{\partial \tilde{u}_i \hat{\sigma}_{ij}}{\partial x_j} - \frac{\partial \hat{q}_j}{\partial x_j} - \frac{\partial Q_j}{\partial x_j} - \alpha - \pi + \varepsilon \quad (2.30)$$

The viscous stress tensor is given by

$$\hat{\sigma}_{ij} = \frac{2\mu}{\text{Re}_r} (\tilde{S}_{ij} - \frac{1}{3} \tilde{S}_{kk} \delta_{ij}), \quad (2.31)$$

where the strain rate tensor and heat flux are given by

$$\tilde{S}_{ij} = \frac{1}{2} \left(\frac{\partial \tilde{u}_i}{\partial x_j} + \frac{\partial \tilde{u}_j}{\partial x_i} \right) \quad (2.32)$$

$$\hat{q}_j = -\frac{c_p \mu}{\text{Re}_r \text{Pr}} \frac{\partial \tilde{T}}{\partial x_j} \quad (2.33)$$

The effects of the small scales are present in the above equations through the SGS stress tensor in the filtered momentum equation,

$$\tau_{ij} = \bar{\rho} (\widetilde{u_i u_j} - \tilde{u}_i \tilde{u}_j), \quad (2.34)$$

and the SGS terms in the filtered energy equation (Vreman et al. 1995),

$$Q_j = \bar{\rho} c_v (\widetilde{T u_j} - \tilde{T} \tilde{u}_j) \quad (2.35)$$

$$\alpha = \tilde{u}_i \frac{\partial \tau_{ij}}{\partial x_j} \quad (2.36)$$

$$\pi = \overline{p \frac{\partial u_j}{\partial x_j}} - \bar{p} \frac{\partial \tilde{u}_j}{\partial x_j} \quad (2.37)$$

$$\varepsilon = \overline{\sigma_{ij} \frac{\partial u_i}{\partial x_j}} - \bar{\sigma}_{ij} \frac{\partial \tilde{u}_i}{\partial x_j} . \quad (2.38)$$

The total energy density of the Favre filtered variables is

$$\hat{E} = c_v \bar{T} + \frac{1}{2} \tilde{u}_i \tilde{u}_i \quad (2.39)$$

For this study, all subgrid scale contributions (α , π and ε) except the heat flux to the total energy equation were neglected since only low Mach numbers were considered. Vreman et al. (1995) demonstrated that this assumption was appropriate for Mach numbers below 0.2. For higher Mach number flows, models for these terms must be included.

2.4 Subgrid Scale Model

The subgrid scale models for LES must represent the additional terms generated by filtering. Basically, the filtering process decomposes the flow into two scales – resolved scale (grid scale) and unresolved scale (subgrid scale). An SGS model should mimic realistically the interactions between these scales, just like RANS models must approximate the Reynolds stresses that appear in the Reynolds decomposed equations. In general, the interactions can be classified into local and non-local interactions in wavenumber space. Local interactions occur among a small band of neighboring scales (wavenumbers), while non-local interactions occur between widely separated scales (wavenumbers). Comparatively, non-local interactions are easier to analyze and model and one of the most important classes of models, eddy viscosity models, is based on the assumption that energy transfer

between resolved scales and unresolved scales is governed by the non-local interactions.

2.4.1 Gradient-Diffusion Models

Many LES models are based on the gradient-diffusion assumption. In this hypothesis, the anisotropic part of the residual stress tensor, τ_{ij} , is assumed to be proportional to the resolved strain rate tensor \tilde{S}_{ij} by

$$\tau_{ij} - \frac{1}{3}\delta_{ij}q^2 = -2\mu_s \left(\tilde{S}_{ij} - \frac{1}{3}\delta_{ij}\tilde{S}_{kk} \right), \quad (2.40)$$

where μ_s is the subgrid viscosity, δ_{ij} is the Kronecker delta, and $q^2 = \tau_{kk}$ is the isotropic part of τ_{ij} . The turbulent, or eddy viscosity is

$$\mu_t = \mu_s = C_d \bar{\rho} \Delta^2 |\tilde{S}_{ij}|, \quad (2.41)$$

where the magnitude of the strain rate tensor is

$$|\tilde{S}| = \sqrt{2\tilde{S}_{ij}\tilde{S}_{ij}}. \quad (2.42)$$

The filter width, Δ , is usually given by $\Delta = (\Delta_x \Delta_y \Delta_z)^{1/3}$, where Δ_x, Δ_y , and Δ_z are the control volume dimensions in the x, y and z directions, respectively, and C_d is a coefficient to be determined.

The proposed subgrid scale models belonging to the gradient-diffusion family can be summarized under the general form

$$\mu_s = \rho c \Delta q, \quad (2.43)$$

in which c is a dimensionless constant, Δ is a length scale, and q is a velocity scale (Ciafalo, 1994). These models can be classified into one of the several models:

1. constant μ_s model: $\mu_s = \rho c_0$
2. strain model: $\mu_s = \rho c_1 \Delta^2 \hat{S}$

3. vorticity model: $\mu_s = \rho c_2 \Delta^2 \hat{\omega}$
4. unresolved energy model: $\mu_s = \rho c_3 \Delta E_s^{1/2}$

2.4.2 Smagorinsky Model

The strain model is by far the most popular subgrid scale model. It was first derived by Smagorinsky (1963). Today this model and its variants are still widely used. This model assumes that the SGS turbulence is locally in a state of equilibrium between production and dissipation. The production of turbulent kinetic energy comes from the cascading of energy from large scales to the small scales, which is then dissipated at the smallest scales. Based on this assumption, Smagorinsky (1963) derived that

$$\nu_t = L^2 |S|, \quad (2.44)$$

in which

$$L = C_s \Delta, \quad (2.45)$$

where C_s is known as the Smagorinsky constant. Lilly (1967) showed that under realized conditions, the Smagorinsky model is consistent with an infinitely extended inertial subrange where the $-5/3$ law holds (Tennekes and Lumley, 1972). He derived that

$$C_s = \frac{1}{\pi} \left(\frac{2}{3\alpha} \right)^{\frac{3}{4}}. \quad (2.49)$$

Assuming the Kolmogorov constant $\alpha = 1.5$, it can be shown that $C_s \approx 0.17$.

Since the birth of Smagorinsky model, it has been applied in many studies with success. However, its further application is limited by one of the major drawbacks – the model constant has to be decided a priori. With the a priori assigned model constants, the model cannot adapt to the physics in local regions of the flow and

differentiate different types of flows. For example, in wall bounded flows the near wall region is not accurately represented. Transitional flows and regions with recirculation zones are also poorly represented. Although some of these problems can be partially overcome by using corrections such as van Driest (1965) damping or intermittency functions (Piomelli et al., 1990), the Smagorinsky model is still far from being universally applicable. Nowadays, the Smagorinsky model is used in the early stage of code development in order to understand the functionality of the code or help validate the implementation of the dynamic SGS models. Due to its limited capability, the original Smagorinsky model was not used in this work.

2.4.3 Isotropic Part of the SGS Model

The isotropic part of the subgrid scale stress tensor, $\tau_{kk} = q^2$, is treated separately from the anisotropic part. For incompressible flows, q^2 may be absorbed into the pressure by defining a modified pressure. For compressible flows, the parameterization of Yoshizawa (1986) is often used

$$q^2 = \tau_{kk} = 2C_i \bar{\rho} \Delta^2 |\tilde{S}|^2. \quad (2.50)$$

The parameterization for q^2 has not been met with agreement in the scientific community. Many researchers have neglected q^2 because it is negligible compared to the thermodynamic pressure (Moin et al., 1991; Spyropoulos and Blaisdell, 1995; Erlebacher et al., 1992). Likewise Vreman et al. (1995) found the dynamic model was unstable unless q^2 was neglected. For the simulations of current work q^2 has been neglected.

2.4.4 Scale Similarity Model

According to Meneveau and Katz (2000), it can be assumed that the structure of the velocity field of the turbulent flow at scales below Δ is postulated to be similar to that at scales above Δ . This concept of scale invariance leads to the scale similarity model, which was first introduced by Bardina et al. (1980). The idea behind this model is that the important interactions between resolved scales and unresolved scales involve the smallest eddies of resolved scales and largest eddies of unresolved scales. The interaction can be modeled as

$$\tau_{ij} = C_B (\tilde{u}_i \tilde{u}_j - \tilde{\tilde{u}}_i \tilde{\tilde{u}}_j), \quad (2.51)$$

where C_B is the model coefficient. However, it is shown by Speziale (1985) that this coefficient has to be 1 to preserve Galilean invariance.

One of the biggest advantages of the scale similarity model is that it can predict energy flux in both directions, i.e., from large scales to small scales and from small scales to large scales. The Smagorinsky model, dissipative in nature, does not possess this trait. It is believed that in an average sense, energy flux is from large scale to small scale. However, backscatter – energy flow from small scales to large scales – does exist and play an important role under certain circumstances such as transitional flows. So it is expected that the scale similarity model can predict the backscatter phenomena much better than the Smagorinsky model.

However, because the scale similarity model lacks a dissipation mechanism, it cannot drain the turbulent kinetic energy, which is transported through the cascade. This is the biggest drawback of this model. It was found by Ferziger (1996) that when the scale similarity model is applied in a large eddy simulation, it hardly dissipates any energy and cannot serve as a ‘stand alone’ SGS model. This has greatly limited the use of the scale similarity model.

2.4.5 Mixed Model

It is known that the Smagorinsky model is dissipative, meanwhile the scale similarity model is capable of capturing many important characteristics of turbulent flow, except being dissipative. So a combination of these two models seems to be reasonable. The ability of the scale similarity part to predict backscatter will enable the model to be applicable on more occasions, while the Smagorinsky part will provide the energy drain. This combination forms the mixed model, put forward by Zang et al. (1993). Although the model was introduced in the dynamic context, it is felt by the author that the essential implication of mixed model is that it combines a scale similarity term and a dissipative term. So the dynamic method is firstly neglected here and will be presented in next section.

According to Germano (1986), subgrid scale stress tensor can be decomposed into three components:

$$\tau_{ij} = \bar{\rho}(\widetilde{u_i u_j} - \tilde{u}_i \tilde{u}_j) = L_{ij}^m + C_{ij}^m + R_{ij}^m, \quad (2.52)$$

where

$$L_{ij}^m = \bar{\rho}(\widetilde{\tilde{u}_i \tilde{u}_j} - \tilde{u}_i \tilde{u}_j) \quad (2.53)$$

$$C_{ij}^m = \bar{\rho}(\widetilde{u_i' \tilde{u}_j'} + \widetilde{\tilde{u}_i' u_j'} - \tilde{u}_i' \tilde{u}_j' - \tilde{u}_i' \tilde{u}_j') \quad (2.54)$$

$$R_{ij}^m = \bar{\rho}(\widetilde{u_i' u_j'} - \tilde{u}_i' \tilde{u}_j'), \quad (2.55)$$

are termed, respectively, the modified Leonard stress tensor, the modified cross-term and the modified SGS Reynolds stress tensor. Modified Leonard stress tensor can be regarded as the addition of a scale similarity term and Leonard stress tensor,

$$L_{ij} = \bar{\rho}(\widetilde{\tilde{u}_i \tilde{u}_j} - \tilde{u}_i \tilde{u}_j), \quad (2.56)$$

and it can be computed explicitly. If the first term in R_{ij}^m is modeled using the

Smagorinsky model and second term in R_{ij}^m , plus the whole C_{ij}^m term, is neglected, the mixed model can be represented as

$$\tau_{ij} - \frac{1}{3} \delta_{ij} \tau_{kk} = -2C_s \Delta^2 \bar{\rho} |\tilde{S}| \tilde{S}_{ij} + L_{ij}^m - \frac{1}{3} \delta_{ij} L_{kk}^m. \quad (2.57)$$

Due to the inherent good characteristics of the mixed model, it has received much attention and proved to be a very effective tool in large eddy simulation, especially when it is combined with a dynamic procedure. Examples include Zang (1993), Liu et al. (1994), Salvetti and Banerjee (1995), Horiuti (1997), Sarghini et al. (1998), and O'Sullivan et al. (1998). Some of these researchers believe that mixed model is physically superior to both Smagorinsky model and scale similarity model.

2.4.6 Dynamic Procedure

The dynamic procedure, also known as dynamic model, was first introduced by Germano et al. (1991) to alleviate some of the shortcomings with the Smagorinsky model. In the dynamic model, the model coefficient C_s is computed dynamically instead of being input a priori so that the model can adapt better to the local situation of the turbulent flows both spatially and temporarily. However, the term 'dynamic procedure' is preferred here since instead of confining the choice to the Smagorinsky model, many models can be used as the base model for the dynamic procedure. From this point of view, the dynamic procedure is a method, rather than the physical model itself. This procedure will be illustrated below using the Smagorinsky model as the base model since this is the method used for this work and the same procedure will work for other base models.

The dynamic procedure utilizes the idea of scale invariance in turbulent flows, which means that the structures of the flow field at different scales are similar to each other. The idea is accomplished by introducing a test filter whose width $\hat{\Delta}$ is larger

than the grid filter width $\bar{\Delta}$. By assuming the same model for both sub-grid filter scale stress and sub-test filter scale stress, the model coefficient can be computed dynamically. The model coefficient can be dependent on space and time. However, when the model coefficient is function of all three directions and time, the accompanying coefficient fluctuation over the space can cause serious numerical instabilities. So for totally or partially homogeneous turbulent flows, the model coefficient can be averaged over the homogeneous direction(s). This formulation has been successfully applied to a variety of flows, yielding more accurate results than the Smagorinsky model.

2.4.6.1 Subgrid Stress

Using the Boussinesq assumption, the Smagorinsky model parameterization for the SGS stress tensor is

$$\tau_{ij} - \frac{2}{3} \delta_{ij} q^2 = -2C_d \bar{\rho} \Delta^2 |\tilde{S}| \left(\tilde{S}_{ij} - \frac{1}{3} \delta_{ij} \tilde{S}_{kk} \right) \quad (2.58)$$

$$q^2 = \frac{1}{2} \tau_{kk} = C_t \bar{\rho} \Delta^2 |\tilde{S}|^2, \quad (2.59)$$

where

$$|\tilde{S}| = \left(2\tilde{S}_{ij}\tilde{S}_{ij} \right)^{1/2} \quad (2.60)$$

$$\bar{\Delta} = (\Delta_x \Delta_y \Delta_z)^{1/3}. \quad (2.61)$$

In this model, τ_{kk} is neglected by setting $C_t = 0.0$. The dynamic procedure uses the information at two different filter levels (grid filter and test filter) to dynamically determine the coefficient C_d . Let

$$t_{ij} = \overline{\rho u_i u_j} - \bar{\rho} \tilde{u}_i \tilde{u}_j, \quad (2.62)$$

which is the stress term after applying the grid filter. In a similar manner, we can compute

$$T_{ij} = \overline{\overline{\rho u_i u_j}} - \frac{\overline{\overline{\rho u_i \rho u_j}}}{\overline{\overline{\rho}}}, \quad (2.63)$$

which is the stress term after applying the test filter which is usually two times as large as the grid filter. The algebraic identity of Germano et al. (1992) in the compressible case gives

$$D_{ij} = T_{ij} - \hat{t}_{ij} = \frac{\overline{\overline{\rho u_i \rho u_j}}}{\overline{\overline{\rho}}} - \frac{\overline{\overline{\rho u_i \rho u_j}}}{\hat{\rho}}. \quad (2.64)$$

Assuming that t_{ij} and T_{ij} can be modeled by the same functional form and a coefficient, C_d

$$t_{ij} - \frac{1}{3} \delta_{ij} t_{kk} \approx \tau_{ij} = -2C_d \overline{\overline{\rho}} \Delta^2 |\tilde{S}| \left(\tilde{S}_{ij} - \frac{1}{3} \delta_{ij} \tilde{S}_{kk} \right), \quad (2.65)$$

and

$$T_{ij} - \frac{1}{3} \delta_{ij} T_{kk} \approx M_{ij} = -2C_d \hat{\rho} \hat{\Delta}^2 |\hat{S}| \left(\hat{S}_{ij} - \frac{1}{3} \delta_{ij} \hat{S}_{kk} \right), \quad (2.66)$$

where

$$\hat{S}_{ij} = \frac{1}{2} \left(\frac{\partial \hat{u}_i}{\partial x_j} + \frac{\partial \hat{u}_j}{\partial x_i} \right), \quad (2.67)$$

and

$$|\hat{S}| = \sqrt{2 \hat{S}_{ij} \hat{S}_{ij}}, \quad (2.68)$$

in which C_d is a coefficient to be computed. Substituting Eq. 2.64 and Eq. 2.65 into Eq. 2.63 yields

$$D_{ij} - \frac{1}{3} \delta_{ij} D_{kk} = 2C_d \left(\overline{\overline{\overline{\overline{\rho \Delta^2 |\tilde{S}| \left(\tilde{S}_{ij} - \frac{1}{3} \delta_{ij} \tilde{S}_{kk} \right)}}}} - \hat{\rho} \hat{\Delta}^2 |\hat{S}| \left(\hat{S}_{ij} - \frac{1}{3} \delta_{ij} \hat{S}_{kk} \right) \right) = 2C_d P_{ij} \quad (2.69)$$

A least-square approach suggested by Lilly (1992) is used to calculate C_d in Eq. 2.69

$$C_d = \frac{1}{2} \frac{\langle D_{ij} P_{ij} \rangle}{\langle P_{ij} P_{ij} \rangle}. \quad (2.70)$$

2.4.6.2 Dynamic Turbulent Prandtl Number

A gradient transport formulation is usually a convenient and efficient way to approximate the turbulent heat flux. So, the heat flux $q_{ij} = c_v (\overline{\rho u_j T} - \bar{\rho} \tilde{u}_j \tilde{T})$ can be expressed as

$$q_{ij} = -\frac{\mu_t c_p}{Pr_t} \frac{\partial \tilde{T}}{\partial x_j}, \quad (2.71)$$

where Pr_t is the SGS turbulent Prandtl number, and μ_t is the SGS eddy viscosity.

The turbulent Prandtl number can be determined by the information from two different grid resolutions, test filtered and grid filtered. For the test filtered scalar flux

$$Q_{ij} = c_v \left(\overline{\widehat{\rho u_j T}} - \hat{\rho} \hat{u}_j \hat{T} \right), \quad (2.72)$$

and grid filtered scalar flux

$$q_{ij} = c_v \left(\overline{\rho u_j T} - \bar{\rho} \tilde{u}_j \tilde{T} \right), \quad (2.73)$$

an algebraic identity exists

$$\begin{aligned} H_j &= Q_{ij} - \hat{q}_{ij} = c_v \left(\overline{\widehat{\rho u_j T}} - \hat{\rho} \hat{u}_j \hat{T} \right) - c_v \left(\overline{\rho u_j T} - \bar{\rho} \tilde{u}_j \tilde{T} \right) \\ &= c_v \left(\overline{\widehat{\rho \tilde{u}_j \tilde{T}}} - \hat{\rho} \hat{u}_j \hat{T} \right). \end{aligned} \quad (2.74)$$

Using a gradient transport form for the turbulent heat flux and SGS eddy viscosity determined from dynamic SGS model for momentum equation,

$$\begin{aligned}
H_j &= -\frac{c_p}{\text{Pr}_t} \left(\widehat{\hat{\mu}}_t \frac{\partial \hat{T}}{\partial x_j} - \widehat{\tilde{\mu}}_t \frac{\partial \tilde{T}}{\partial x_j} \right) \\
&= \frac{c_p C_d}{\text{Pr}_t} \left(\widehat{\hat{\rho} \Delta^2} \left| \hat{S} \right| \frac{\partial \hat{T}}{\partial x_j} - \widehat{\bar{\rho}} \left| \tilde{S} \right| \frac{\partial \tilde{T}}{\partial x_j} \right). \tag{2.75}
\end{aligned}$$

Writing the above vector equation in symbolic form gives

$$E_j = -\frac{C_d \bar{\Delta}^2}{\text{Pr}_t} \frac{c_p}{c_v} F_j, \tag{2.76}$$

where

$$E_j = \widehat{\bar{\rho} \tilde{u}_j \tilde{T}} - \widehat{\hat{\rho} \hat{u}_j \hat{T}}, \tag{2.77}$$

and

$$F_j = \widehat{\hat{\rho} \alpha} \left| \hat{S} \right| \frac{\partial \hat{T}}{\partial x_j} - \widehat{\bar{\rho}} \left| \tilde{S} \right| \frac{\partial \tilde{T}}{\partial x_j}, \tag{2.78}$$

where α is the square of the ratio of these different filters, which means

$$\alpha = \frac{\hat{\Delta}^2}{\bar{\Delta}^2}. \tag{2.79}$$

Using the least square approach, we can compute the turbulent Prandtl number as

$$\text{Pr}_t = -C_d \bar{\Delta}^2 \frac{c_p}{c_v} \frac{\langle F_k F_k \rangle}{\langle E_k F_k \rangle}. \tag{2.80}$$

2.4.7 Localization Method for SGS Models

The dynamic procedure has been applied to homogeneous or partially homogeneous turbulent flows with success. However, when the model coefficient is computed and applied locally, numerical instabilities may occur because of the large spatial fluctuations in the model coefficient. This drawback, if unresolved, will greatly limit the prospect of the dynamic procedure, especially when the simulation is

applied to inhomogeneous flows, such as duct flow with transverse ribs. To overcome this problem, Ghosal et al. (1995) proposed a localization method. It is obvious that Eq. 2.69 includes an approximation in that the model coefficient C_d is regarded as constant throughout the test filter volume, which is inaccurate mathematically. So let

$$\alpha_{ij} = \bar{\rho} \bar{\Delta}^2 \left| \tilde{S} \right| \left(\tilde{S}_{ij} - \frac{1}{3} \delta_{ij} \tilde{S}_{kk} \right) \quad (2.81)$$

$$\beta_{ij} = \hat{\rho} \hat{\Delta}^2 \left| \hat{S} \right| \left(\hat{S}_{ij} - \frac{1}{3} \delta_{ij} \hat{S}_{kk} \right) \quad (2.82)$$

$$L_{ij} = D_{ij} - \frac{1}{3} \delta_{ij} D_{kk}. \quad (2.83)$$

The accurate representation of Eq. 2.69 should be

$$L_{ij} = 2C_d \alpha_{ij} - 2\widehat{C_d \beta_{ij}}, \quad (2.84)$$

the accurate solution of which will be a Fredholm's integral equation of the second kind. The computer resources involved with its solution will be formidable.

To lessen this problem, Piomelli and Liu (1995) introduced a new method to compute the model coefficient C_d . C_d in Eq. 2.84 can be regarded as function of L_{ij} , α_{ij} , β_{ij} and C_d itself. If the model coefficient under the test filter can be regarded as given, an iterative scheme can be devised to compute C_d . Using a least square method, this scheme can be summarized as

$$C_d = -\frac{1}{2} \frac{\left(L_{ij} - 2\widehat{C_d \beta_{ij}} \right) \alpha_{ij}}{\alpha_{mn} \alpha_{mn}}. \quad (2.85)$$

This model was applied to the large eddy simulation of turbulent rotating channel flow with the additional requirement that total viscosity $\nu + \nu_t$ is no less than 0. Very good agreement with DNS results was achieved, which shows that localization method can be used successfully when proper caution is applied.

Meneveau et al. (1996) developed a Lagrangian formulation of the dynamic procedure, in which localization is implemented through the averaging of the model

coefficient along the particle path-lines. This method will also allow the model to be applied in a fully local sense.

In this work, turbulent duct flow will be studied using large eddy simulation, which is inhomogeneous in two directions. In future work, heat transfer will be added to the duct flow, which makes the flow totally inhomogeneous. So a localized model can better meet the needs of both current and future research work. As a trial, the model coefficient C_d was averaged over the test filter volume surrounding the local grid, and then the turbulent viscosity was adjusted to make sure that total viscosity was larger than 0. Through some numerical experiments, it was found that this method could also work very well under the framework of the current LES code. Moreover, the model shows very good asymptotic behavior near the wall. The average value of C_d in the first layer of the cell is on the order of 10^{-6} , and its standard deviation is on the same order. It is fully expected that the dynamic Smagorinsky model with this simple localization method will perform well in simulating the inhomogeneous turbulent duct flow with rotation and heat transfer.

2.5 Integral-Vector Form of the Equations

The nondimensional governing equations can be written in terms of the primitive variables ($\bar{p}, \tilde{u}, \tilde{v}, \tilde{w}$ and \tilde{T}) using the ideal gas law. The equations are multiplied by the nondimensional gas constant, R , for simplification. The governing equations in vector form are

$$[T] \frac{\partial W}{\partial t} + \frac{\partial E}{\partial x} + \frac{\partial F}{\partial y} + \frac{\partial G}{\partial z} = B. \quad (2.86)$$

The nondimensional governing equations can be written in conservative form as

$$\int_{\Omega} [T] \frac{\partial W}{\partial t} d\Omega + \int_{\partial\Omega} [E\hat{i} + F\hat{j} + G\hat{k}] dS = \int_{\Omega} B d\Omega, \quad (2.87)$$

where $[T] = \frac{\partial U}{\partial W}$ is the time derivative Jacobian matrix, which is shown in Appendix

A.

The primitive variables, W , and the conservative variables, U , are

$$W = \begin{bmatrix} \bar{p} \\ \tilde{u} \\ \tilde{v} \\ \tilde{w} \\ \tilde{T} \end{bmatrix}; \quad U = \begin{bmatrix} \bar{p}/\tilde{T} \\ \bar{p}\tilde{u}/\tilde{T} \\ \bar{p}\tilde{v}/\tilde{T} \\ \bar{p}\tilde{w}/\tilde{T} \\ \bar{p}/\tilde{T} \left[c_v \tilde{T} + \frac{1}{2} (\tilde{u}^2 + \tilde{v}^2 + \tilde{w}^2) \right] \end{bmatrix} \quad (2.88)$$

The flux vector may be thought of as being comprised of inviscid, viscous and subgrid scale components, for example

$$E = E_i - E_v + E_s. \quad (2.89)$$

The inviscid components of the flux vector are given by

$$E_i = \begin{bmatrix} \bar{p}\tilde{u}/\tilde{T} \\ \bar{p}\tilde{u}^2/\tilde{T} + R\bar{p} \\ \bar{p}\tilde{u}\tilde{v}/\tilde{T} \\ \bar{p}\tilde{u}\tilde{w}/\tilde{T} \\ (\bar{p}\tilde{u}/\tilde{T})\tilde{H} \end{bmatrix}; \quad F_i = \begin{bmatrix} \bar{p}\tilde{v}/\tilde{T} \\ \bar{p}\tilde{u}\tilde{v}/\tilde{T} + R\bar{p} \\ \bar{p}\tilde{v}^2/\tilde{T} \\ \bar{p}\tilde{v}\tilde{w}/\tilde{T} \\ (\bar{p}\tilde{v}/\tilde{T})\tilde{H} \end{bmatrix}; \quad G_i = \begin{bmatrix} \bar{p}\tilde{w}/\tilde{T} \\ \bar{p}\tilde{u}\tilde{w}/\tilde{T} + R\bar{p} \\ \bar{p}\tilde{v}\tilde{w}/\tilde{T} \\ \bar{p}\tilde{w}^2/\tilde{T} \\ (\bar{p}\tilde{w}^2/\tilde{T})\tilde{H} \end{bmatrix}. \quad (2.90)$$

And the viscous components of the flux vector are given by

$$E_v = \begin{bmatrix} 0 \\ \hat{\sigma}_{xx} \\ \hat{\sigma}_{xy} \\ \hat{\sigma}_{xz} \\ \tilde{u}\hat{\sigma}_{xx} + \tilde{v}\hat{\sigma}_{xy} + \tilde{w}\hat{\sigma}_{xz} - \hat{q}_x \end{bmatrix}; \quad F_v = \begin{bmatrix} 0 \\ \hat{\sigma}_{xy} \\ \hat{\sigma}_{yy} \\ \hat{\sigma}_{yz} \\ \tilde{u}\hat{\sigma}_{xy} + \tilde{v}\hat{\sigma}_{yy} + \tilde{w}\hat{\sigma}_{yz} - \hat{q}_y \end{bmatrix};$$

$$G_y = \begin{bmatrix} 0 \\ \hat{\sigma}_{xz} \\ \hat{\sigma}_{yz} \\ \hat{\sigma}_{zz} \\ \tilde{u}\hat{\sigma}_{xz} + \tilde{v}\hat{\sigma}_{yz} + \tilde{w}\hat{\sigma}_{zz} - \hat{q}_z \end{bmatrix}. \quad (2.91)$$

The subgrid scale stress components of the flux vector are given by

$$E_s = \begin{bmatrix} 0 \\ \tau_{xy} \\ \tau_{xz} \\ Q_x \end{bmatrix}; \quad F_s = \begin{bmatrix} 0 \\ \tau_{xy} \\ \tau_{yz} \\ Q_y \end{bmatrix}; \quad G_s = \begin{bmatrix} 0 \\ \tau_{xz} \\ \tau_{zz} \\ Q_z \end{bmatrix}, \quad (2.92)$$

where the resolved total enthalpy is

$$\hat{H} = c_p \tilde{T} + \frac{1}{2}(\tilde{u}^2 + \tilde{v}^2 + \tilde{w}^2). \quad (2.93)$$

The viscous stress tensor is given by

$$\begin{aligned} \sigma_{xx} &= \frac{2\mu R}{3\text{Re}_r} \left(2 \frac{\partial \tilde{u}}{\partial x} - \frac{\partial \tilde{v}}{\partial y} - \frac{\partial \tilde{w}}{\partial z} \right) \\ \sigma_{yy} &= \frac{2\mu R}{3\text{Re}_r} \left(2 \frac{\partial \tilde{v}}{\partial y} - \frac{\partial \tilde{u}}{\partial x} - \frac{\partial \tilde{w}}{\partial z} \right) \\ \sigma_{zz} &= \frac{2\mu R}{3\text{Re}_r} \left(2 \frac{\partial \tilde{w}}{\partial z} - \frac{\partial \tilde{u}}{\partial x} - \frac{\partial \tilde{v}}{\partial y} \right) \\ \hat{\sigma}_{xy} &= \frac{\mu R}{\text{Re}_r} \left(\frac{\partial \tilde{u}}{\partial y} + \frac{\partial \tilde{v}}{\partial x} \right) \\ \hat{\sigma}_{xz} &= \frac{\mu R}{\text{Re}_r} \left(\frac{\partial \tilde{u}}{\partial z} + \frac{\partial \tilde{w}}{\partial x} \right) \\ \hat{\sigma}_{yz} &= \frac{\mu R}{\text{Re}_r} \left(\frac{\partial \tilde{v}}{\partial z} + \frac{\partial \tilde{w}}{\partial y} \right). \end{aligned} \quad (2.94)$$

The heat flux vectors are

$$\begin{aligned}
\hat{q}_x &= \frac{c_p \mu R}{\text{Re}_r \text{Pr}} \frac{\partial \tilde{T}}{\partial x} \\
\hat{q}_y &= \frac{c_p \mu R}{\text{Re}_r \text{Pr}} \frac{\partial \tilde{T}}{\partial y} \\
\hat{q}_z &= \frac{c_p \mu R}{\text{Re}_r \text{Pr}} \frac{\partial \tilde{T}}{\partial z}.
\end{aligned} \tag{2.95}$$

The subgrid scale stress tensors are

$$\begin{aligned}
\tau_{xx} &= \frac{1}{3} q^2 R - \frac{2\mu_t R}{3} \left(2 \frac{\partial \tilde{u}}{\partial x} - \frac{\partial \tilde{v}}{\partial y} - \frac{\partial \tilde{w}}{\partial z} \right) \\
\tau_{yy} &= \frac{1}{3} q^2 R - \frac{2\mu_t R}{3} \left(2 \frac{\partial \tilde{v}}{\partial y} - \frac{\partial \tilde{u}}{\partial x} - \frac{\partial \tilde{w}}{\partial z} \right) \\
\tau_{zz} &= \frac{1}{3} q^2 R - \frac{2\mu_t R}{3} \left(2 \frac{\partial \tilde{w}}{\partial z} - \frac{\partial \tilde{u}}{\partial x} - \frac{\partial \tilde{v}}{\partial y} \right) \\
\tau_{xy} &= \mu_t R \left(\frac{\partial \tilde{u}}{\partial x} + \frac{\partial \tilde{v}}{\partial y} \right) \\
\tau_{xz} &= \mu_t R \left(\frac{\partial \tilde{u}}{\partial z} + \frac{\partial \tilde{w}}{\partial x} \right) \\
\tau_{yz} &= \mu_t R \left(\frac{\partial \tilde{v}}{\partial z} + \frac{\partial \tilde{w}}{\partial y} \right),
\end{aligned} \tag{2.96}$$

and the SGS heat flux vector components are

$$\begin{aligned}
Q_x &= -\frac{c_v \mu_t R}{\text{Pr}_t} \frac{\partial \tilde{T}}{\partial x} \\
Q_y &= -\frac{c_v \mu_t R}{\text{Pr}_t} \frac{\partial \tilde{T}}{\partial y} \\
Q_z &= -\frac{c_v \mu_t R}{\text{Pr}_t} \frac{\partial \tilde{T}}{\partial z}.
\end{aligned} \tag{2.97}$$

2.6 Finite Volume Approach

The finite volume approach is particularly flexible for use in discretization. This approach allows the domain to be decomposed into any number of arbitrarily shaped cells, with the restriction that the cells completely fill the domain. The principle used in the finite volume approach converts a volume integration into a surface integral using Gauss divergence theorem. The equation for the conservation of mass in divergence form is

$$\frac{\partial \rho}{\partial t} + \frac{\partial \rho u}{\partial x} + \frac{\partial \rho v}{\partial y} + \frac{\partial \rho w}{\partial z} = 0, \quad (2.98)$$

which may be integrated on a control volume by

$$\int_{\Omega} \frac{\partial \rho}{\partial t} d\Omega + \int_{\Omega} \left(\frac{\partial \rho u}{\partial x} + \frac{\partial \rho v}{\partial y} + \frac{\partial \rho w}{\partial z} \right) d\Omega = 0, \quad (2.99)$$

where Ω represents the volume of the cell. An alternate notation uses the divergence operator,

$$\nabla = \frac{\partial}{\partial x} \vec{i} + \frac{\partial}{\partial y} \vec{j} + \frac{\partial}{\partial z} \vec{k}, \quad (2.100)$$

and represents the flux vector as

$$\vec{F} = \begin{bmatrix} \rho u \\ \rho v \\ \rho w \end{bmatrix}. \quad (2.101)$$

Thus, Eq. 2.99 can be written as

$$\int_{\Omega} \frac{\partial \rho}{\partial t} d\Omega + \int_{\Omega} \nabla \cdot \vec{F} d\Omega = 0. \quad (2.102)$$

Using the Gauss divergence theorem on the second term, it may be recast as

$$\int_{\Omega} \frac{\partial \rho}{\partial t} d\Omega + \int_{\partial\Omega} \vec{F} d\vec{S} = 0, \quad (2.103)$$

where the cell face area vector is $d\vec{S} = \vec{n} dS$, dS is the magnitude of the area and \vec{n} is the unit normal vector. For simplification, S is used instead of dS for the rest of this

thesis when the integration symbol is not present. By using the Gauss divergence theorem, the contribution of the surrounding cells may be evaluated at the surface of the control volume. With consistent treatment of fluxes, the finite volume formulation enforces conservation.

2.7 Dependent Variables

Although the most common set of dependent variables for the Navier-Stokes equations are the conservative variables $(\rho, \rho u_i, \rho E_t)$, there are several advantages in using primitive variables. Working with primitive variables simplifies the gradient calculations and implementation of the boundary conditions. For LES, using primitive variables simplifies the statistics collecting process. For the current work, the set of primitive variables chosen is (ρ, u_i, T) . This choice of primitive variables is convenient for the derivation of the preconditioned governing equations. (Pletcher and Chen, 1993; Choi and Merkle, 1993)

2.8 Integral Approximations

The cell-centered finite volume formulation was applied to the filtered governing equations in conservation law integral form given by Eq. 2.87

$$\int_{\Omega} [T] \frac{\partial W}{\partial t} d\Omega + \int_{\partial\Omega} [E\hat{i} + F\hat{j} + G\hat{k}] dS = \int_{\Omega} B d\Omega. \quad (2.104)$$

The volume integral in the first term was approximated by using the mean value theorem

$$\int_{\Omega} [T] \frac{\partial W}{\partial t} d\Omega \approx \left([T] \frac{\partial W}{\partial t} \right)_{i,j,k} \Omega_{i,j,k}. \quad (2.105)$$

The face values used in the surface integral were evaluated using the mid-point rule

$$\int_{\partial\Omega} (E\vec{i} + F\vec{j} + G\vec{k}) \cdot d\vec{S} \approx C(W), \quad (2.106)$$

where

$$C(W) = \sum_{\beta=1}^6 \left\{ (En_x + Fn_y + Gn_z) \right\}_{\beta}, \quad (2.107)$$

and β denotes the six faces of the hexahedral cell.

The flux vector on a cell face between the cell center (i, j, k) and $(i+1, j, k)$, for example, was calculated by

$$E_{\beta} = E(W_{i+1/2, j, k}), \quad (2.108)$$

where

$$W_{i+1/2, j, k} = \frac{1}{2} (W_{i, j, k} + W_{i+1, j, k}). \quad (2.109)$$

2.9 Gradients

A face-based gradient approach was used in this work to calculate the gradients. The gradients of u , v , w , and T were calculated to evaluate the viscous and subgrid scale contributions to the flux vectors. The gradients were calculated by the Gauss divergence theorem on an auxiliary control volume obtained by shifting the main volume one-half index in the direction of the particular cell face. For example, to calculate the gradients on the face between cells (i, j, k) and $(i+1, j, k)$, an auxiliary control volume is created denoted by Ω' , the volume of which is given by

$$\Omega' = \frac{1}{2} \left[\Omega_{(i, j, k)} + \Omega_{(i+1, j, k)} \right]. \quad (2.110)$$

The gradient is found by

$$\int_{\Omega'} \nabla \phi d\Omega' = \int_{\gamma\Omega'} \phi d\vec{S}' . \quad (2.111)$$

For the Cartesian control volume, $\nabla \phi \Omega' = \phi_x \vec{i} + \phi_y \vec{j} + \phi_z \vec{k}$. Using the mean value theorem, Eq. 2.111 is approximated by

$$\nabla \phi \Omega' = \sum_{\beta'=1}^6 (\phi \vec{S}'_{\beta'}) . \quad (2.112)$$

The face areas on the auxiliary control volume are

$$S'_i = \Delta y \Delta z \quad S'_j = \Delta x \Delta z \quad S'_k = \Delta x \Delta y . \quad (2.113)$$

On an orthogonal Cartesian grid the gradient calculations reduce to second order central differences. Because the problems addressed in this work were all based on orthogonal Cartesian grids, this simplification was used to reduce the computational cost of the simulations.

2.10 Low Mach Number Preconditioning

This research was concerned with computing flows with significant regions of low Mach number. This could occur from recirculation zones, flows near a stagnation point or low speed flows with high heat transfer. These flows lead to significant density and property variations, so that it is convenient to use the compressible form of the governing equations. Moreover, flows used to validate compressible formulations are often incompressible benchmark computations or low speed experimental data. Traditional compressible flow solvers exhibit convergence problems at low Mach numbers due to the wide disparity between the convective and acoustic signal speeds leading to large differences in the magnitudes of the eigenvalues of the system.

Use of time derivative preconditioning reduces the difference in the magnitudes of the eigenvalues, and leads to convergence rates nearly independent of Mach number. Turkel (1987) was one of the first to discuss preconditioning, especially for

the Euler equations. Feng and Merkle (1990) later applied preconditioning methods to the Euler equations using the conserved variables with an approximate factorization scheme. Choi and Merkle (1993) extended preconditioning to viscous flows. Withington et al. (1991) applied preconditioning to chemically reacting flows using a dual time step formulation for time accuracy. Pletcher and Chen (1993) developed a similar preconditioning formulation, which was adopted here.

Preconditioning is employed by adding a pseudo-time derivative that is premultiplied by a preconditioning matrix. The preconditioning matrix is constructed in such a way as to modify the system eigenvalues. The goal is to keep the magnitude of eigenvalues closer together, at speeds closer to the convective speed, thereby improving convergence rates for the time marching algorithm.

For the present formulation, the preconditioning was incorporated by adding a pseudo-time derivative to the left hand side of momentum equation as

$$[\Gamma] \frac{\partial W}{\partial \tau} \Omega + [T] \frac{\partial W}{\partial t} + C(W) = 0, \quad (2.114)$$

where τ is the pseudo-time, and $[\Gamma]$ is the preconditioning matrix, which is given in Appendix A. The addition of a pseudo-time derivative is termed the dual time step approach, and involves iterating in pseudo-time for each step in physical time. Upon convergence of the subiteration process in pseudo-time, the pseudo-time term vanishes and the original unsteady governing equations are satisfied.

2.11 Lower-Upper Symmetric Gauss-Seidel

The lower-upper symmetric Gauss-Seidel (LU-SGS) scheme is used for this work as the integration method. It was originally developed by Yoon and Jameson (1987) for the Euler and Navier-Stokes equations without preconditioning. Dailey and Pletcher (1996) used this scheme for code development that included preconditioning and multigrid. The pseudo-time derivative was discretized with a Euler backward

difference, and the physical time derivative was discretized with a three point backward difference, yielding

$$\Gamma\Omega \frac{\Delta W}{\Delta\tau} + T(W^{n+1}) + C(W^{n+1}) = B(W^{n+1})\Omega, \quad (2.115)$$

where $\Delta W = W^{m+1} - W^m$ and $\Delta\tau = \tau^{m+1} - \tau^m$. The inviscid flux vectors were linearized about the pseudo-time level m as

$$\begin{aligned} E_i^{m+1} &\approx E_i^m + [A]^m \Delta W \\ F_i^{m+1} &\approx F_i^m + [B]^m \Delta W \\ G_i^{m+1} &\approx G_i^m + [C]^m \Delta W, \end{aligned} \quad (2.116)$$

where $[A] = \partial E_i / \partial W$, $[B] = \partial F_i / \partial W$ and $[C] = \partial G_i / \partial W$, which are listed in Appendix A. The viscous and subgrid scale stress fluxes are lagged. Multiplying by Γ^{-1} we can obtain

$$\left(\frac{\Omega}{\Delta\tau} [I] + [\Gamma]^{-1} [T]^m \frac{3}{2} \frac{\Omega}{\Delta t} + [\Gamma]^{-1} \sum_{\beta=1}^6 [([A]n_x + [B]n_y + [C]n_z)S] \right) \Delta W = -[\Gamma]_m^{-1} R^m. \quad (2.117)$$

The $(i \pm \frac{1}{2}, j, k)$ faces are labeled as $\beta = 1$ and 2 . The $(i, j \pm \frac{1}{2}, k)$ faces are labeled as $\beta = 3$ and 4 , and $(i, j, k \pm \frac{1}{2})$ faces are labeled as $\beta = 5$ and 6 , respectively.

Inviscid flux Jacobians in the directions normal to faces 1 and 2 are denoted as $[\hat{A}]$. The inviscid Jacobians in the directions normal to faces 3 and 4 are denoted as $[\hat{B}]$, and the inviscid Jacobians in the directions normal to faces 5 and 6 are denoted as $[\hat{C}]$.

$$\begin{aligned} [\hat{A}] &= ([A]n_x + [B]n_y + [C]n_z)_{\beta=1,2} \\ [\hat{B}] &= ([A]n_x + [B]n_y + [C]n_z)_{\beta=3,4} \\ [\hat{C}] &= ([A]n_x + [B]n_y + [C]n_z)_{\beta=5,6}. \end{aligned} \quad (2.118)$$

For an orthogonal Cartesian grid, the matrices simplify so that $[\hat{A}] = [A]$, $[\hat{B}] = [B]$ and $[\hat{C}] = [C]$. Letting $\Delta\tau \rightarrow \infty$,

$$\begin{aligned} & \left([\Gamma]^{-1} [T]^m \frac{3}{2} \frac{\Omega}{\Delta t} + [\Gamma]^{-1} \left[[\hat{A}]_1 S_1 - [\hat{A}]_2 S_2 + [\hat{B}]_3 S_3 - [B]_4 S_4 + [\hat{C}]_5 S_5 - [\hat{C}]_6 S_6 \right] \right) \Delta W \\ & = -[\Gamma]^{-1} R. \end{aligned} \quad (2.119)$$

To apply the LU-SGS algorithm to the preconditioned system of equations, the flux Jacobians were modified (Chen and Shuen, 1994) to accommodate the preconditioned matrix as

$$[\hat{A}] = [\Gamma][\Gamma]^{-1}[\hat{A}] = [\Gamma][\tilde{A}] \quad (2.120)$$

$$[\tilde{A}] = [\Gamma]^{-1}[\hat{A}]. \quad (2.121)$$

The flux Jacobian, $[\tilde{A}]$, is split as

$$[\tilde{A}] = [\tilde{A}]^+ + [\tilde{A}]^-, \quad (2.122)$$

where

$$[\tilde{A}]^\pm = \frac{1}{2} \omega \left([\tilde{A}] \pm \gamma_A [I] \right). \quad (2.123)$$

$$\gamma_A = r_A \cdot \max \left(\left| \lambda_{[\tilde{A}]} \right| \right), \quad (2.124)$$

where $\lambda_{[\tilde{A}]}$ is the maximum eigenvalue of $[\tilde{A}]S$, and ω and r_A are relaxation factors greater than or equal to unity. This splitting of the flux Jacobians is done to ensure diagonal dominance. Multiplying by the preconditioning matrix $[\Gamma]$ yields

$$[\Gamma][\tilde{A}]^\pm = \frac{1}{2} \omega \left([\Gamma][\tilde{A}] \pm \gamma_A [\Gamma] \right) = \frac{1}{2} \omega \left([\hat{A}] \pm [\Gamma] \right). \quad (2.125)$$

The flux Jacobians on the control volume faces are approximated as

$$\left([\Gamma][\tilde{A}]\Delta W \right)_1 = \left([\Gamma][\tilde{A}]^+ \Delta W \right)_{i,j,k} + \left([\Gamma][\tilde{A}]^- \Delta W \right)_{i+1,j,k}$$

$$\left([\Gamma][\tilde{A}]\Delta W \right)_2 = \left([\Gamma][\tilde{A}]^+ \Delta W \right)_{i-1,j,k} + \left([\Gamma][\tilde{A}]^- \Delta W \right)_{i,j,k}$$

$$\begin{aligned}
([\Gamma][\tilde{B}]\Delta W)_3 &= ([\Gamma][\tilde{B}]^+ \Delta W)_{i,j,k} + ([\Gamma][\tilde{B}]^- \Delta W)_{i,j+1,k} \\
([\Gamma][\tilde{B}]\Delta W)_4 &= ([\Gamma][\tilde{B}]^+ \Delta W)_{i,j-1,k} + ([\Gamma][\tilde{B}]^- \Delta W)_{i,j,k} \\
([\Gamma][\tilde{C}]\Delta W)_5 &= ([\Gamma][\tilde{C}]^+ \Delta W)_{i,j,k} + ([\Gamma][\tilde{C}]^- \Delta W)_{i,j,k+1} \\
([\Gamma][\tilde{C}]\Delta W)_6 &= ([\Gamma][\tilde{C}]^+ \Delta W)_{i,j,k-1} + ([\Gamma][\tilde{C}]^- \Delta W)_{i,j,k}. \quad (2.126)
\end{aligned}$$

Eq. 2.119 can be written as

$$([L] + [D] + [U])\Delta W = -[\Gamma]^{-1} R, \quad (2.127)$$

where matrices $[L]$, $[D]$ and $[U]$ are

$$[L] = -[\Gamma]^{-1} \left[([\Gamma][\tilde{A}]^+)_{i-1,j,k} S_2 + ([\Gamma][\tilde{B}]^+)_{i,j-1,k} S_4 + ([\Gamma][\tilde{C}]^+)_{i,j,k-1} S_6 \right] \quad (2.128)$$

$$\begin{aligned}
[D] = [\Gamma]^{-1} [T] \frac{3}{2} \frac{\Omega}{\Delta t} + [\Gamma]^{-1}_{i,j,k} \left[([\Gamma][\tilde{A}]^+)_{i,j,k} S_1 - ([\Gamma][\tilde{A}]^-)_{i,j,k} S_2 + \right. \\
\left. ([\Gamma][\tilde{B}]^+)_{i,j,k} S_3 - ([\Gamma][\tilde{B}]^-)_{i,j,k} S_4 + ([\Gamma][\tilde{C}]^+)_{i,j,k} S_5 - ([\Gamma][\tilde{C}]^-)_{i,j,k} S_6 \right] \quad (2.129)
\end{aligned}$$

$$[U] = -[\Gamma]^{-1} \left[([\Gamma][\tilde{A}]^-)_{i+1,j,k} S_1 + ([\Gamma][\tilde{B}]^-)_{i,j+1,k} S_3 + ([\Gamma][\tilde{C}]^-)_{i,j,k+1} S_5 \right]. \quad (2.130)$$

Note that $[D]$ is only a function of quantities defined at the center point (i, j, k) , $[L]$ is only a function of quantities at the lower points and $[U]$ is only a function of quantities at the upper points. These facts are utilized in the solution procedure described below.

Due to the splitting of the flux Jacobians,

$$[\Gamma][\tilde{A}]^+ - [\Gamma][\tilde{A}]^- = \omega\gamma_A [\Gamma] \quad (2.131)$$

$$[\Gamma][\tilde{B}]^+ - [\Gamma][\tilde{B}]^- = \omega\gamma_B [\Gamma] \quad (2.132)$$

$$[\Gamma][\tilde{C}]^+ - [\Gamma][\tilde{C}]^- = \omega\gamma_C [\Gamma]. \quad (2.133)$$

It is assumed that $S_1 \approx S_2$, $S_3 \approx S_4$ and $S_5 \approx S_6$, such that Eq. 2.129 reduces to

$$[D] = [\Gamma]^{-1} [T] \frac{3}{2} \frac{\Omega}{\Delta t} + \Omega (\gamma_A S_{12} + \gamma_B S_{34} + \gamma_C S_{56}) [I], \quad (2.134)$$

where $S_{12} = \frac{1}{2}(S_1 + S_2)$, $S_{34} = \frac{1}{2}(S_3 + S_4)$ and $S_{56} = \frac{1}{2}(S_5 + S_6)$. For the orthogonal Cartesian grid, $S_1 = S_2$, $S_3 = S_4$ and $S_5 = S_6$. Due to the nature of the preconditioning matrix employed here, the product of $[\Gamma]^{-1} [T]$ is a diagonal matrix, and $[D]$ is diagonal. This is not generally true for other preconditioners, such as those of Choi and Merkle (1993), or Lee and van Leer (1993).

To solve the system efficiently, Eq. 2.127 is approximately factorized as

$$([L] + [D])[D]^{-1}([D] + [U])\Delta W = -[\Gamma]^{-1} R \quad (2.135)$$

and solved in three steps as follows:

Step 1:

$$\begin{aligned} ([L] + [D])\Delta W^* &= -[\Gamma]^{-1} R \\ \Delta W^* &= [D]^{-1} \left(-[\Gamma]^{-1} R - [L]\Delta W^* \right) \end{aligned} \quad (2.136)$$

Step 2:

$$\begin{aligned} ([D] + [U])\Delta W &= [D]\Delta W^* \\ \Delta W &= \Delta W^* - [D]^{-1} [U]\Delta W \end{aligned} \quad (2.137)$$

Step 3:

$$W^{m+1} = W^m + \Delta W \quad (2.138)$$

The solution process for Step 1 involves sweeping on $i + j + k = \text{constant}$ planes from the lower corner, $(i, j, k) = (1, 1, 1)$, to the upper corner, $(i, j, k) = (ni, nj, nk)$, of the grid, where ni , nj and nk are the number of interior control volumes in the x , y and z directions. Since $[L]\Delta W^*$ is always known during this process, it is moved

to the right hand side in Step 1. For Step 2, the solution is swept from the upper corner to the lower corner of the grid. Since $[U]\Delta W$ is always known during this process, it is moved to the right hand side in Step 2. Note that $[D]$ is diagonal. The inversion of $[D]$ requires very little computational effort.

An algorithm explained by Dailey (1997) is used to sweep on $i + j + k = \text{constant}$ planes. The boundary conditions are determined by setting $\Delta W = 0$ at ghost cells and explicitly setting W at the beginning of each iteration. The same algorithm is used for this research.

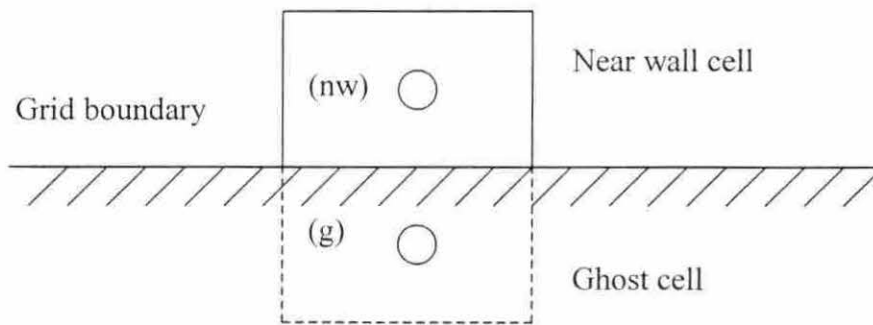


Figure 2.1 Typical ghost cell

2.12 Convergence Criteria

The convergence criteria is based on

$$R = \frac{\sum_{i,j,k} |R_2|}{N_{cells}} < TOL \quad (2.139)$$

where R_2 reflects the residual of the u-momentum equation in the system, and N_{cells} represents the total number of cells. For the two-dimensional formulations, TOL is set so that R decreases four orders of magnitude (Dailey, 1997). For time-accurate three-dimensional formulations, TOL is set so that R decreases two orders of magnitude.

2.13 Boundary Conditions

Boundary conditions are enforced explicitly by using “ghost” or “image” cells. The ghost cells are generated by mapping the control volume on the boundary about the grid boundary itself. The ghost cells have the same volume and surface areas as their respective fluid cells on the boundary. Equation 2.109 is used with boundary condition information, such as the no-slip boundary condition, zero normal pressure boundary condition, and isothermal wall conditions. From this information, the ghost cell values can be calculated so that these boundary conditions are enforced. Figure 2.1 depicts a typical ghost cell.

2.13.1 Solid Wall Boundary Conditions

For solid walls, the no-slip boundary condition was used. For stationary walls, all three velocity components were zero. By using Eq. 2.109, the relationship between the variables in the ghost cell and the fluid cell becomes

$$\begin{aligned}
p_g &= p_{nw} \\
u_g &= -u_{nw} \\
v_g &= -v_{nw} \quad , \\
w_g &= -w_{nw} \\
T_g &= 2T_{iso} - T_{nw}
\end{aligned} \tag{2.140}$$

where T_{iso} is the isothermal temperature to be enforced at the boundary.

2.13.2 Periodic Boundary Condition

Periodic boundary conditions were used extensively in this work. For incompressible flows, the ghost cells were simply transposed copies of the fluid cells at the matching periodic boundary. The relationship between the ghost and fluid variables is given by

$$\begin{aligned}
p_p(0, y, z, t) &= p_p(L_x, y, z, t) \\
u(0, y, z, t) &= u(L_x, y, z, t) \\
v(0, y, z, t) &= v(L_x, y, z, t) \quad . \\
w(0, y, z, t) &= w(L_x, y, z, t) \\
T(0, y, z, t) &= T(L_x, y, z, t)
\end{aligned} \tag{2.141}$$

For compressible flow with heat transfer, a quasi-developed assumption is used, and the corresponding periodicity is

$$\begin{aligned}
p_p(0, y, z, t) &= p_p(L_x, y, z, t) \\
\rho u(0, y, z, t) &= \rho u(L_x, y, z, t) \\
v(0, y, z, t) &= v(L_x, y, z, t) \quad , \\
w(0, y, z, t) &= w(L_x, y, z, t) \\
T(0, y, z, t) &= T(L_x, y, z, t) - \Delta T_x
\end{aligned} \tag{2.142}$$

where L_x is the length of the computational domain in the streamwise direction, and p_p is the periodic component of the pressure, $p(x, y, z, t) = \beta x + p_p(x, y, z, t)$. β is the streamwise gradient of pressure, which will be further explained in Chap. 3.

The temperature difference, ΔT_x , is related to the net heat transferred to the flow in the solution domain, and is found by integrating the energy equation around the boundaries. More specifically, for constant properties ΔT_x is given by

$$\Delta T_x = \frac{q_w P L_x}{\dot{m}}, \quad (2.143)$$

where P is the perimeter of the cross section.

2.13.3 Symmetry Boundary Condition

Symmetry boundary conditions, which are often used in RANS computations to reduce the size of the domain, are usually not applicable in DNS or LES, because the instantaneous flow is not symmetric about any particular plane, although the mean flow may be. By applying this type of boundary condition, some important physical effects may be removed. More often, symmetry boundary conditions have been used to represent free surfaces.

2.13.4 Thermal Boundary Condition

Basically, there are three different common types of thermal boundary conditions: adiabatic, isothermal, and isoflux. Adiabatic wall means $\frac{\partial T}{\partial y} = 0$ and it is implemented by a first-order approximation

$$T_g = T_{nw}. \quad (2.144)$$

The isothermal boundary condition is easily implemented as below

$$T_g = 2T_{wall} - T_{nw}, \quad (2.145)$$

where T_{wall} is a predefined value for the wall temperature. The isoflux thermal boundary condition is usually invoked by using the following formula

$$\left(-k \frac{\partial T}{\partial y} \right)_w = q_w, \quad (2.146)$$

and

$$T_{wall} = T_{nw} + \frac{\Delta y \cdot q_w}{k}. \quad (2.147)$$

Sometimes, it is to our advantage to use an alternative method: specify a linear distribution of temperature to achieve the same effect as isoflux. The parameters for the linear distribution can be determined by running several trials with thermal BC expressed by Eq. 2.147. This alternative can remove the unrealistic non-zero fluctuations near the solid walls (Kasagi, 1989).

CHAPTER 3. LARGE EDDY SIMULATION OF INCOMPRESSIBLE TURBULENT FLOW IN A DUCT OF SQUARE CROSS-SECTION

3.1 Introduction

Turbulent flow in a straight duct is an interesting topic in that it has many applications in aeropropulsion systems, building systems, and electronics cooling devices. The study of this kind of flow will enable better design and application of these systems and devices. This was the motivation for studying this topic. Furthermore, this topic is also valuable from a fundamental point of view. Turbulent flow in a duct has some complicated features because the flow is bounded in both the cross-stream and spanwise directions, which creates corners along the flow. According to Gavrilakis (1992), in the vicinity of such a corner, the turbulent flow field is subjected to a remarkable structural change. The consequence of this is that a mean velocity field in planes perpendicular to its boundaries is generated, which is recognized as secondary flows of Prandtl's second kind (Prandtl, 1926). This kind of secondary flow is the result of turbulence itself and cannot be found in laminar duct flow. Secondary flows of Prandtl's first kind stem from the skewing of the mean cross-stream vorticity and the associated secondary velocities are generally much stronger than those induced by turbulence (Bradshaw, 1987).

Secondary flow plays an important role in duct flow. Although the flow in the cross-section is relatively weak with its maximum magnitude being only 2-3% of the streamwise bulk velocity, its effects on the wall shear stress distribution, heat transfer rates, and transport of passive tracers are quite significant (Demuren, 1990). So one of the major goals of this work was to capture the characteristics of secondary flow

correctly so that other features such as mean flow structure, statistics distribution and wall shear stress distribution can be predicted correctly as well. Large eddy simulation is used as the tool for the investigation. Since the turbulent flow is inhomogeneous in two directions – cross-stream direction and spanwise direction, and it is expected to lose its homogeneity in the streamwise direction in the further work with the addition of heat transfer, a locally based model is better to interpret the physics of the flow. The model has been described in Chapter 2, so it will not be mentioned more here.

Many researchers have been interested in turbulent flow in a duct in the recent ten years. Among them, quite a few employed direct numerical simulations and large eddy simulations. Gavrilakis (1992) simulated a duct flow at bulk Reynolds number 4410 using direct numerical simulation. Because of the low Reynolds number and subsequent large integral length, the domain was chosen to be $20\pi\delta \times 2\delta \times 2\delta$, with $20\pi\delta$ in the streamwise direction and 2δ in both cross-stream and spanwise directions. δ is the half duct diameter. The grid used was $1000 \times 127 \times 127$ in these three directions, respectively. The work has achieved very good agreement with existing experimental data. Due to the easy availability of this DNS data, Gavrilakis' results have been used as benchmark data by many researchers. This work also uses his data for comparison and code validation. Huser and Biringen (1993) conducted another direct numerical simulation of duct flow at bulk Reynolds number 10320. Furthermore, they proposed a possible explanation for the secondary flow. However, due to the apparent difference between Gavrilakis' and Huser's results, the author has some doubt about the validity of the latter because Gavrilakis utilized a much denser grid. For this reason, Huser's results were not compared with in this work.

The forerunner in large eddy simulation of duct flow was Madabhushi and Vanka (1991), who utilized the traditional Smagorinsky model in their simulation. The Re_b of the flow was 5810. Su and Friedrich (1994, 1994a) also reported the application of LES in the simulation of duct flow in both straight and curved ducts, of which the

former one is of interest here. The subgrid scale model used was Schumann's SGS model and their Re_b was 49,000. Most recently, Pallares and Davidson (2000) reported their large eddy simulation of turbulent square duct flow, and the Re_b in their simulation was also 4410, the same as used by Gavrilakis. A localized one-equation dynamic SGS model developed by Kim and Menon (1997) was used in their investigation.

So the present work will be the first one to use a localized dynamic Smagorinsky model to simulate turbulent duct flow. Compared with the traditional Smagorinsky model, its dynamic counterpart is believed to be more accurate and capable of capturing more features. Also, the dynamic Smagorinsky model is simpler and easier to implement than the other two models utilized by Su and Friedrich (1994, 1994a) and Pallares and Davidson (2000). And compared with the localization method of the model employed by Pallares and Davidson, the localization method in this work is more straightforward and efficient, yet has proved to be sufficient for the current work. Moreover, the numerical method in this work uses a coupled approach to handle the momentum equation and energy equations, which is different from other LES researchers. This methodology will allow more efficient and accurate handling of heat transfer problem, which will be addressed in future work.

3.2 Problem Description

In this study, turbulent flow in a duct with square cross section is studied since it is believed that an aspect ratio of unity will show the effects of walls and corners to the utmost extent. Although studies on other aspect ratios are also worthwhile, they

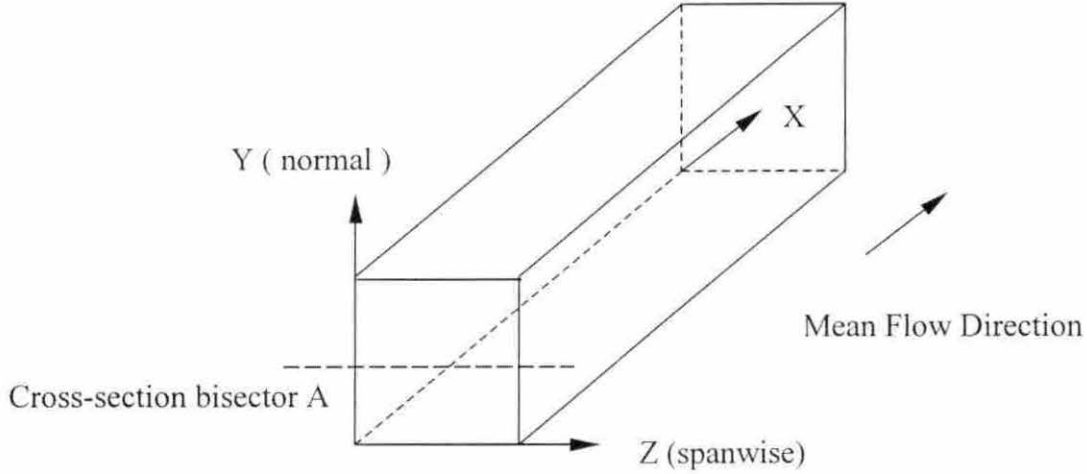


Figure 3.1 Geometry of the domain.

are not conducted in this work. After nondimensionalization, the dimensions of the cross-stream and spanwise directions are both 2, while the streamwise length of the domain varies according to the Re_b of the simulation. A representative domain is depicted in Figure 3.1.

The governing equations for turbulent duct flow are as below

$$\frac{\partial \rho}{\partial t} + \frac{\partial(\rho u_i)}{\partial x_i} = 0 \quad (3.1)$$

$$\frac{\partial(\rho u_i)}{\partial t} + \frac{\partial(\rho u_i u_j)}{\partial x_j} = -\frac{\partial p}{\partial x_i} + \frac{\partial \sigma_{ij}}{\partial x_j} \quad (3.2)$$

$$\frac{\partial(\rho E)}{\partial t} + \frac{\partial(\rho E u_j)}{\partial x_j} = -\frac{\partial(\rho u_i)}{\partial x_i} - \frac{\partial q_j}{\partial x_j} + \frac{\partial(\sigma_{ij} u_i)}{\partial x_j}, \quad (3.3)$$

where the shear stress tensor is

$$\sigma_{ij} = \frac{2\mu}{Re_\tau} (S_{ij} - \frac{1}{3} S_{kk} \delta_{ij}), \quad (3.4)$$

the strain rate tensor is

$$S_{ij} = \frac{1}{2} \left(\frac{\partial u_i}{\partial x_j} + \frac{\partial u_j}{\partial x_i} \right), \quad (3.5)$$

and the Reynolds number based on reference quantities is $Re_r = \rho_r V_r L_r / \mu_r$. The heat flux vector is given by Fourier's law of heat conduction as

$$q_j = -\frac{c_p \mu}{Re_r Pr} \frac{\partial T}{\partial x_j}. \quad (3.6)$$

Here the bulk velocity U_b is chosen as the reference velocity and reference Reynolds number is Re_b . Although Eq. 3.3 is not useful for these incompressible simulations, it is still solved together with continuity equation and momentum equation because the algorithm utilizes a coupled approach. After Favre filtering, the equations become

$$\frac{\partial \bar{\rho}}{\partial t} + \frac{\partial \bar{\rho} \tilde{u}_i}{\partial x_i} = 0 \quad (3.7)$$

$$\frac{\partial \bar{\rho} \tilde{u}_i}{\partial t} + \frac{\partial \bar{\rho} \tilde{u}_i \tilde{u}_j}{\partial x_j} = -\frac{\partial \bar{p}}{\partial x_i} + \frac{\partial \hat{\sigma}_{ij}}{\partial x_j} - \frac{\partial \tau_{ij}}{\partial x_j} \quad (3.8)$$

$$\frac{\partial \bar{\rho} \hat{E}}{\partial t} + \frac{\partial \left[(\bar{\rho} \hat{E} + \bar{p}) \tilde{u}_i \right]}{\partial x_i} = -\frac{\partial \tilde{u}_i \hat{\sigma}_{ij}}{\partial x_j} - \frac{\partial \hat{q}_j}{\partial x_j} - \frac{\partial Q_j}{\partial x_j} - \alpha - \pi + \varepsilon. \quad (3.9)$$

The subgrid terms, τ_{ij} and Q_j , are evaluated using the dynamic Smagorinsky model and can be written as

$$\tau_{ij} - \frac{2}{3} \delta_{ij} q^2 = -2C_d \bar{\rho} \Delta^2 |\tilde{S}| \left(\tilde{S}_{ij} - \frac{1}{3} \delta_{ij} \tilde{S}_{kk} \right) \quad (3.10)$$

$$q^2 = \frac{1}{2} \tau_{kk} = C_l \bar{\rho} \Delta^2 |\tilde{S}|^2 \quad (3.11)$$

and

$$Q_j = -\frac{\mu_t c_p}{Pr_t} \frac{\partial \tilde{T}}{\partial x_j}. \quad (3.12)$$

C_d , C_l and Pr_t are model coefficients and supposed to be computed dynamically. It

is worth mentioning here that although turbulent Prandtl number Pr_t is modeled as a dynamic coefficient, it is assigned a predefined value 0.9 because there is no mean temperature gradient in the flow. C_f is assigned to be 0 since the isotropic part of the subgrid stress is neglected. Only C_d is computed during the simulation in the cases in this chapter.

The turbulent flow in the duct is assumed to be fully developed, which has brought great convenience to the study. One of the most important benefits from this assumption is that periodic boundary conditions can be used for the streamwise direction so that the domain size can be tremendously decreased. Since the flow is incompressible, the velocity components \tilde{u}_i and temperature \tilde{T} are periodic

$$\begin{aligned}\tilde{u}(0, y, z, t) &= \tilde{u}(L_x, y, z, t) \\ \tilde{v}(0, y, z, t) &= \tilde{v}(L_x, y, z, t) \\ \tilde{w}(0, y, z, t) &= \tilde{w}(L_x, y, z, t) \\ \tilde{T}(0, y, z, t) &= \tilde{T}(L_x, y, z, t)\end{aligned}\tag{3.13}$$

where L_x is the streamwise length of the domain.

However, the pressure cannot be regarded as periodic because there is a negative streamwise pressure gradient that drives the flow. So the pressure can be decomposed into periodic and aperiodic components as

$$\bar{p}(x, y, z, t) = \beta x + \bar{p}_p(x, y, z, t),\tag{3.14}$$

where β is the average pressure gradient and the subscript p indicates periodic component, which satisfies

$$\bar{p}_p(0, y, z, t) = \bar{p}_p(L_x, y, z, t).\tag{3.15}$$

This decomposition would have made the governing equations equation of state much more complicated had it not been for the fact that βx is negligibly small compared with \bar{p}_p for moderate Reynolds numbers and moderate domain lengths. Therefore, it is assumed that

$$\bar{\rho} \approx \frac{\bar{P}_p}{RT}. \quad (3.16)$$

The governing equations are consequently unchanged, except that the equations are in terms of \bar{p}_p , and the streamwise momentum equation contains an additional pressure gradient parameter, β , as a body force.

The streamwise pressure gradient parameter is adjusted at each time step to provide the desired mass flow rate. This has often been done for turbulent channel flow simulations (Benocci and Pinelli, 1990; Dailey, 1997). The equation for β can be written as

$$\beta^{n+1} = \beta^n - \frac{1}{\Delta t} \left[\left(\frac{\dot{m}}{A_c} \right)^0 - 2 \left(\frac{\dot{m}}{A_c} \right)^n + \left(\frac{\dot{m}}{A_c} \right)^{n-1} \right], \quad (3.17)$$

where \dot{m}^n is the average mass flow rate for the duct flow at time level n , Δt is the physical time step, and A_c is the cross-area of the duct. The average mass flow rate is defined as

$$\frac{\dot{m}}{A_c} = \frac{1}{L_y L_z} \int_{-1}^1 \int_{-1}^1 \langle \rho u \rangle_x dy dz, \quad (3.18)$$

where $\langle \rangle_x$ denotes the average in x direction. The desired mass flow rate is $(\dot{m}/A_c)^0$.

3.3 Simulation Details

The discretization and numerical solution process is well described in Chapter 2 and will not be mentioned here. For the numerical process, meshes are generated to partition the duct into small control volumes. The grid is uniform in the x direction and clustered toward the walls using algebraic hyperbolic tangent stretching in the y and z directions. Using the y direction as example, the stretching method is

$$y_i = \frac{\tanh(a\xi_i)}{\tanh(a)}, \quad (3.19)$$

where

$$\xi_i = -1 + 2 \frac{i-1}{i_{\max}-1} \quad \text{for } i = 1, \dots, i_{\max} \quad (3.20)$$

$$a = \frac{1}{2} \ln \left[\frac{(1+b)}{(1-b)} \right] \quad \text{for } 0 \leq b < 1. \quad (3.21)$$

The parameter b controls the stretching of the grid, and typically $b = 0.7 - 0.95$. In cases of this chapter, 0.94 is chosen for b in both y and z directions to ensure enough resolution near the wall. Figure 3.2 shows a mesh for a quadrant of the cross-section seen from the outlet direction.

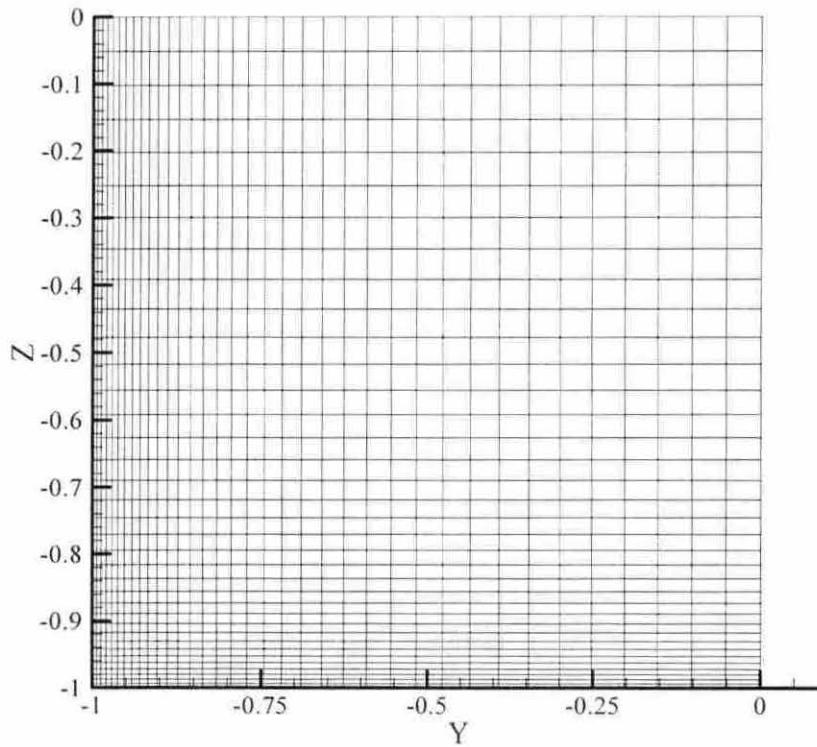


Figure 3.2 Mesh of a quadrant of the cross-section

The length of the domain is found to be very dependent on the Reynolds number. It is the author's belief that the streamwise length of the domain should be large enough so that the longitudinal two-point correlation coefficient between the inlet and outlet

$$f(x) = \frac{\overline{u(0)u(L_x)}}{u'^2} \quad (3.22)$$

becomes zero. With enough domain length, the velocity fields at the inlet and outlet become uncorrelated and the periodic boundary condition can be used with justification. Findings of Gavrilakis (1992) support this very well. The final domain length used in his work is 20π . However, when 16π and 8π were used by Gavrilakis for the simulations, the maximum intensity of streamwise velocity (u_{rms}) were 2% and 6% lower, respectively. Similar phenomena are observed in this work. Reynolds numbers of 6,000, 8,000 and 10,000 were used in cases of this chapter. When the domain length 6.4 was used, satisfactory results can be obtained only for $Re_b = 10,000$. For simulations run using this length for Reynolds number 8,000 and 6,000, peak intensities of all three velocity components were significantly lower than the DNS results of Gavrilakis (1992). More interestingly, the differences between intensities of these LES simulations and those of DNS simulations grow larger when Re_b decreases. This is consistent with the observation that correlation length increases with the decrease of Reynolds number. More intuitively, this means that flow structures grow larger when the Reynolds number is dropping. Through numerical trials, appropriate domain length was found for each Reynolds number. The domain dimensions for all three Reynolds numbers are listed in Table 3.1 together with grid sizes.

It should be noticed that Reynolds numbers used in this work are different from those used by Gavrilakis. This is because high Reynolds numbers are more often to be encountered in practical applications. On the other hand, although Reynolds take

Table 3.1 Simulation domain dimensions and grid sizes

Re_b	Nondimensional size	Grid Size
10,000	$6.4 \times 2 \times 2$	$72 \times 72 \times 72$
8,000	$14.1 \times 2 \times 2$	$108 \times 72 \times 72$
6,000	$24.0 \times 2 \times 2$	$108 \times 72 \times 72$

numbers are different, the profiles and mean velocity and turbulent intensities should on similar looks after being normalized using friction velocity. So different Reynolds numbers disclose the same nature of the flow. Moreover, using higher Reynolds number can reduce the requirement of streamwise domain length, and consequently computational resources.

Initial velocities were generated through applying a two-dimensional parabolic mean velocity field in the domain with background random fluctuations. The initial mean flow field was

$$\begin{aligned}
 u(x, y, z) &= \frac{9}{4}(1 - y^2)(1 - z^2) \\
 v(x, y, z) &= 0 \\
 w(x, y, z) &= 0
 \end{aligned}
 \tag{3.23}$$

where $9/4$ was the initial centerline velocity, which was calculated to ensure that the initial mass flow rate was the same as the target mass flow rate so that there would not be a great change in streamwise pressure gradient, which may cause instabilities in the simulation. A uniform streamwise velocity of unity was also given as an initial condition in some trials. No differences in results have been observed, but it took more simulation time.

The nondimensional physical time step was chosen to be 0.01, and the reference Mach number was 0.001 to ensure the terms discarded are negligible in the Favre filtered equations. In the first stage of simulation, the SGS model was turned off to speed up the simulation. 10,000 – 20,000 time steps were involved in this step. Then

the model was activated and the simulation took around another 15,000 time steps to collect mean flow and turbulence statistics. Since the friction velocity u_τ was around 0.063, 15,000 time steps meant around 10 large eddy turn over times, t_c , which is defined as $t_c = 1/u_\tau$. It is assumed that this is long enough to collect all the temporal information of the flow.

The whole domain was divided into several blocks that were simulated on several processors. The short domain of $6.4 \times 2 \times 2$ was divided into 8 blocks, while the other two domains were divided into 12 blocks. The simulations are run on both the Origin 3800 and Origin 2000 using the message passing interface (MPI).

3.4 Results and Discussion

Through the simulations, it was found that all three cases yielded similar features. For example, the velocity contours were very close to each other. So were the secondary flow patterns. Also, the turbulent kinetic energy level in all three cases was all around $2.1u_\tau^2$, where u_τ is the friction velocity. For this reason, the mean velocity field is presented here only for the $Re_b = 6000$ case to study the secondary flow field in the duct. However, turbulent statistics are shown for both $Re_b = 6000$ and $Re_b = 8000$ cases to compare with those of the DNS results from Gavrilakis (1992).

3.4.1 Mean Velocity Field

Mean velocity is first averaged in the streamwise direction since a fully developed velocity field is assumed for this flow. This instantaneous mean velocity field is used for the computation of mass flow rate and friction velocity. The instantaneous mean velocity field is further ensemble averaged in time as the simulation proceeds to

obtain the final mean velocity field, which is used to produce ensemble averaged global quantities, such as friction velocity and velocity profiles.

In the simulation, it is desirable that friction velocity be computed accurately, as a natural consequence of a successful simulation. A correlation, which was originally for circular pipe flows, was adapted by Jones (1976) and is used here for comparison purpose for duct flow

$$1/f^{\frac{1}{2}} = 2 \log \left(\text{Re}_j f^{\frac{1}{2}} \right) - 0.8. \quad (3.24)$$

f is the friction factor and can be expressed as $f = 8u_\tau^2/U_b^2$. Although this correlation was originally used for circular pipes, it is also applicable to a duct, too. Gavrilakis (1992) showed that Re_j , the modified Reynolds number for a duct, needs to be defined to account for the difference of cross-sections between duct and circular pipe. For a square duct, $\text{Re}_j = 1.125 \text{Re}_b$. For $\text{Re}_b = 6,000$, u_τ is 6.55×10^{-2} based on this correlation and the simulation yields an ensemble averaged friction velocity of 6.69×10^{-2} . Considering the error involved in the discretization and modeling process, as well the uncertainty of the correlation itself, this 2% difference is regarded as excellent agreement.

Figure 3.3 shows the mean streamwise velocity along a cross-section bisector A for $\text{Re}_b = 6000$. Bisector A is in the spanwise direction, as shown in Fig. 3.1. Because of symmetry of the flow in all four quadrants, DNS results by Gavrilakis only show the streamwise velocity profile in a quadrant. So the data of the current LES simulation were also quadrant averaged to compare with the DNS results. Gavrilakis' DNS data are also presented in Fig. 3.3. Both DNS and LES velocities are normalized by the friction velocity and denoted as u^+ . It is believed that this normalization will show similar profiles for the same type of flows under different Reynolds numbers. Through normalization, the essential features of the turbulent flows can be captured.

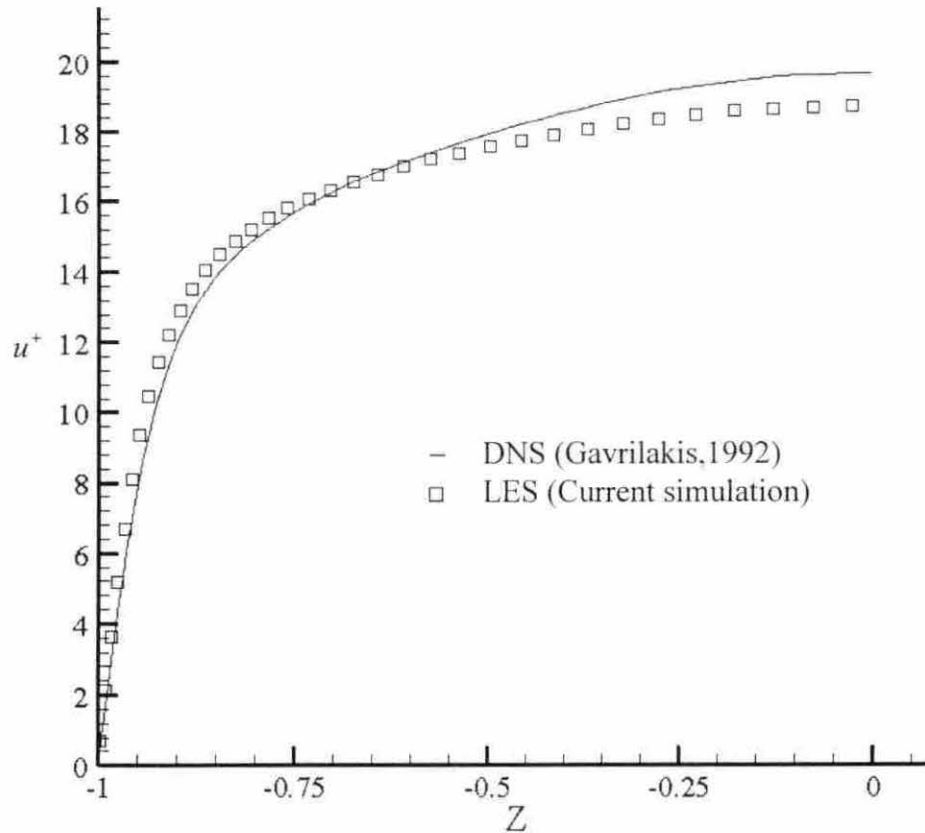


Figure 3.3 Mean streamwise velocity along the bisector A.

From the figure, it can be seen that the LES result matches that of DNS fairly well. Differences can be observed between the two profiles, which is believed mainly to be induced by the discrepancy in Reynolds number. For the LES case, since Re_b is higher than that in the DNS case, the velocity profile is observed to be flatter in the central region of the cross-section, as well as steeper near the wall. Although the different grid resolution may also account for the disagreement, Reynolds number difference is the main cause for the disagreement between the LES and DNS results.

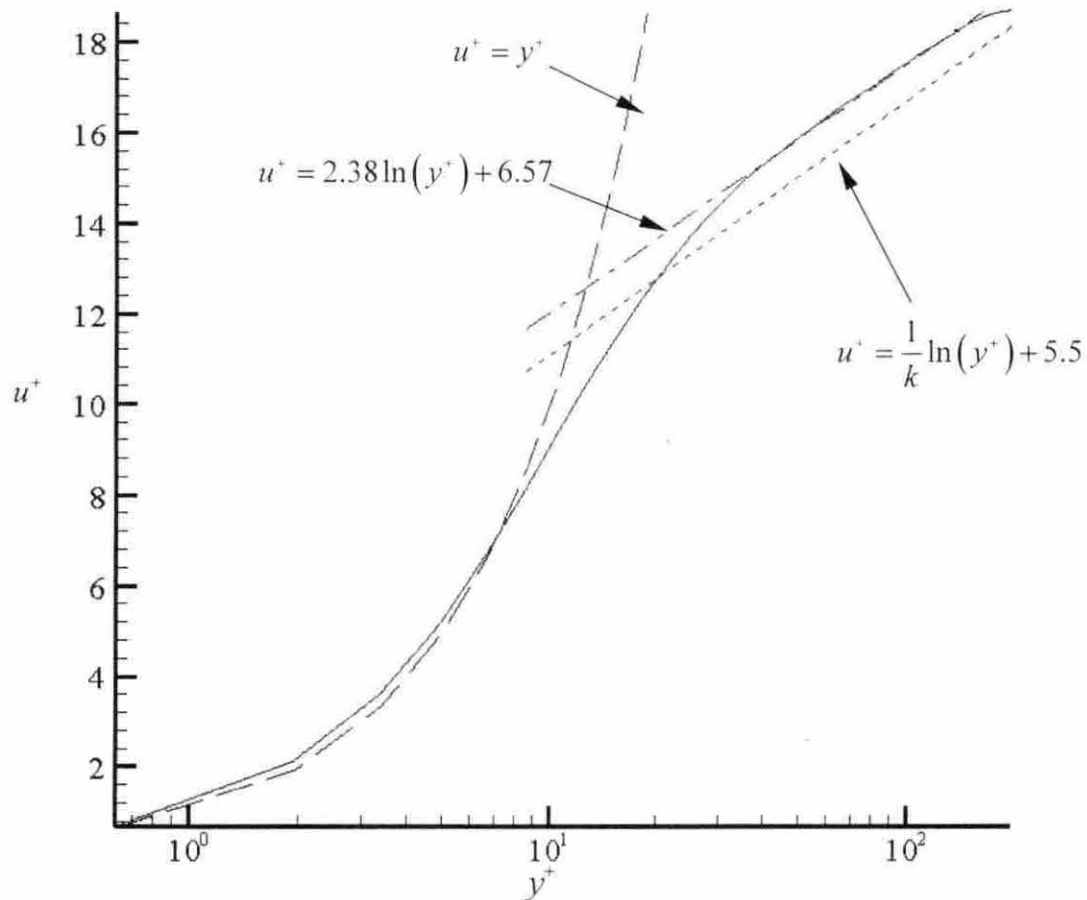


Figure 3.4 u^+ distribution with respect to logarithmic coordinate.

To understand the result of the simulation better, streamwise velocity, normalized by friction velocity, is depicted against distance along the wall bisector in the logarithmic sense, as shown in Fig. 3.4, together with law of the wall:

$$u^+ = \frac{1}{k} \ln(y^+) + 5.5, \quad (3.25)$$

where $k = 0.41$ is the von Karman constant and $y^+ = zu_t \text{Re}_h$. This equation is

regarded to be governing the law of the wall region of a turbulent boundary layer. From Fig. 3.4, it can be seen that the viscous sublayer has been predicted very well, which means the good near wall resolution of the grid ($y_{min}^+ = 0.628$) plus the excellent behavior of the model close to the wall is very effective in capturing the flow structure in this layer. However, overshooting is apparent in the law of wall region, compared with Eq. 3.25. This phenomenon is very similar to the result of Huser and Birigen (1993), and it seems to be induced from the stronger turbulence production near the walls away from the corners compared with turbulent boundary layer flows. The consequence is that buffer zone, which is between the viscous sublayer and law of the wall region, is quite big, ranging from $y^+ = 8 - 40$. Since buffer zone is where turbulence production is most intensive, the peak of turbulent intensity of streamwise velocity, u_{rms} , is expected to occur in this region.

Contours of streamwise velocity in the cross-section are shown in Figure 3.5. It can be seen that the streamwise velocity is not perfectly symmetric about the bisectors. This is the natural result from numerical simulation – Gavrilakis also found apparent asymmetry in his results, even though with much higher grid resolution. In Figure 3.6, the secondary flow field in the cross-section in the duct also shows some asymmetry. The secondary flow for a turbulent duct is composed of four pairs of countering rotating cells at the four corners, each pointing to a corner of the cross-section. In each pair, the two cells are symmetric to each other about the diagonal of the cross-section. This is the most important feature of turbulent duct flow and has been captured with great accuracy. So it is safe to claim that large eddy simulation using the dynamic Smagorinsky model with a simple localization method is able to predict the mean characteristics of turbulent duct flow successfully.

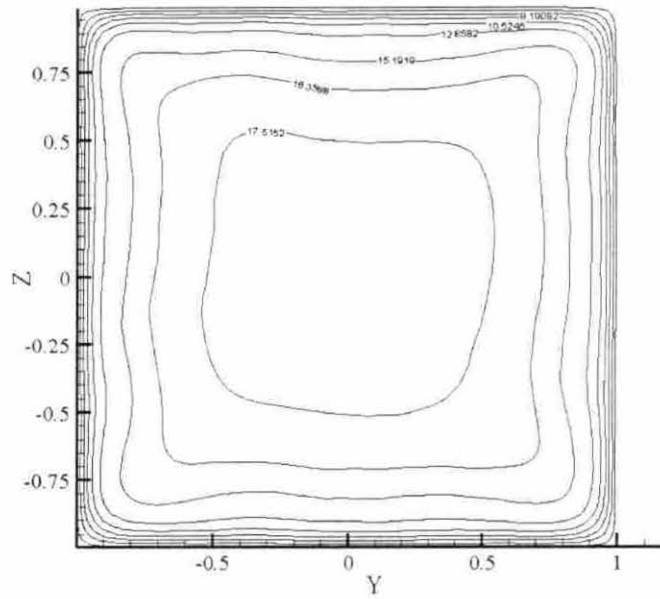


Figure 3.5 Contours of streamwise velocity normalized by friction velocity.

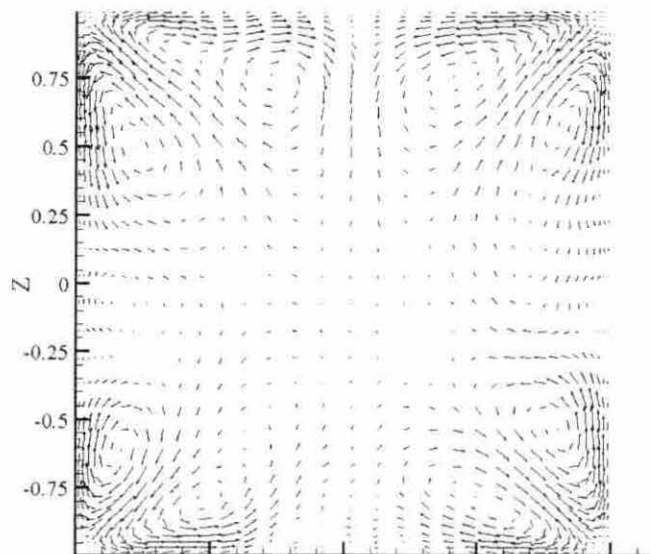


Figure 3.6 Secondary flow field in the cross-section.

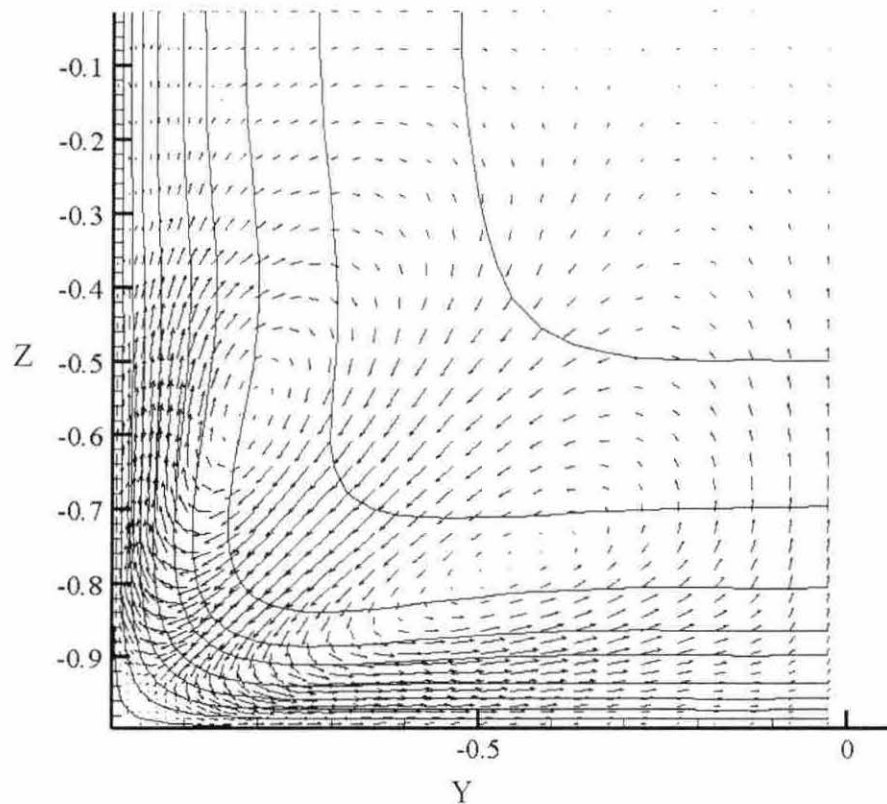


Figure 3.7 Streamwise velocity contour and secondary flow field in a quadrant

Secondary flow and streamwise mean flow are shown together in Fig. 3.7 to show the effects of the secondary velocity field on the streamwise flow. To get rid of the asymmetry in the flow, a quadrant averaging was performed to obtain flow information only in one quadrant of the cross-section by averaging the whole cross-section about the bisectors. The two counter rotating cells are very symmetric to each other in the quadrant averaged flow. The maximum magnitude of the secondary flow velocity is only about 2% of the bulk velocity based on the results of this simulation,

which is in the range of a normal value for a typical secondary flow in the duct. Despite the small velocity, secondary flow does play an important role in the flow; as can be seen, it has distorted the contours of the streamwise velocity. The secondary flow is very active in transporting the high momentum fluid from central region to the corner along the corner angle bisector and the low momentum fluid from the corner along the walls and bisectors to the central region, which greatly enhances the mixing and scalar transport capability of the flow. Gavrilakis (1992) also reported a small cell near the wall bisector, which, however, cannot be found in Fig. 3.7. This might be due to the relatively large grid spacing utilized in the large eddy simulation. Compared with the main secondary flow, its effects on the global features should be smaller, and its contribution to transport can be neglected.

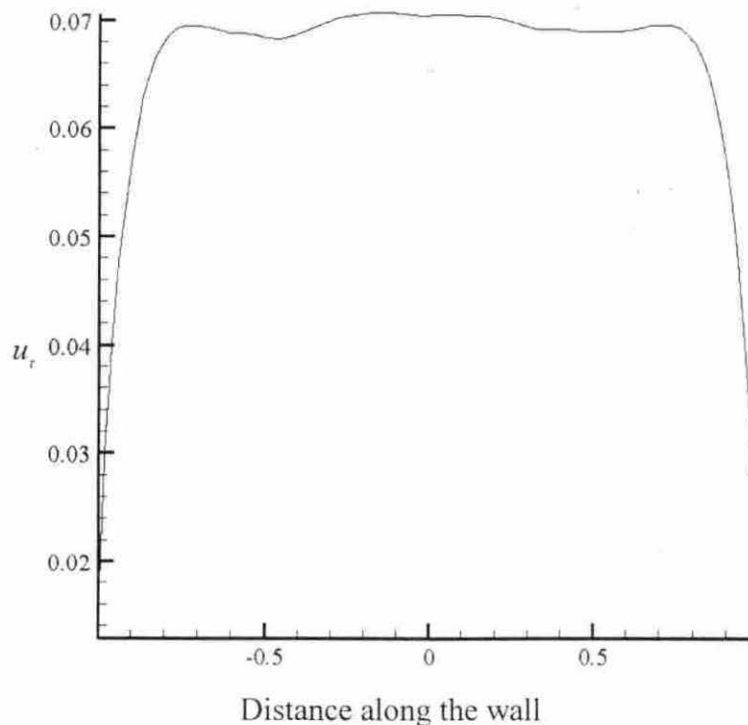


Figure 3.8 Friction velocity distribution along the wall

Due to the secondary flow, certain features are also present in the distribution of the friction velocity on the wall in the cross section, as shown in Figure 3.8. The friction velocity distribution is averaged on all four walls because the distributions should be symmetric about the corner. Because the secondary flow transports the high speed fluid from the central region to the region near the corner, it can be seen that there exist two peaks of friction velocity near the ends of the wall. In the middle of the wall, a higher value is also found because part of the high momentum fluid is transported to the corner region and further moved to this region through the rotating cells. The distribution of friction velocity is in very good agreement with that of Gavrilakis (1992) qualitatively. However, the ratio of peak to mean value on the distribution found by Gavrilakis is larger than of the present case by about 10%. Upon further examination, the maximum magnitude of secondary flow of the DNS case is found to be around 3% of the mean velocity, about 50% larger than in LES case. This contributes to the higher ratio between peak value and mean value in the DNS case and it further illustrates the importance of secondary flow in the momentum transport in duct flow. The reason for this difference is not known yet, although it may be partly attributed to the difference in Reynolds numbers.

The formation of secondary flow field in the turbulent duct flow is closely related with the rectangular shape of the cross-section, since secondary flow is not observed in turbulent circular pipe flow. So intuitively, the strong inhomogeneity in the cross-stream and spanwise directions produced by the walls and corners has caused the secondary flow. Moreover, the secondary flow is also the consequence of turbulence as it can not be observed in laminar duct flow – that is why it is called secondary flow of Prandtl's second kind. So this secondary flow is the combined consequence of geometry and turbulent transport. However, up to now, the mechanism responsible for the existence of such secondary flow has not been explained very clearly. Huser and Birnigen (1993) performed a quadrant analysis to study to origin of this kind of secondary flow. They found that ejection structures are produced during a burst event and contain two streamwise counter-rotating vortices. Due to the reduced mean shear

at the corner angle bisector, ejections from the corners are prohibited. Thus, a mean secondary flow from the core toward the corner is formed. Meanwhile, the strong ejections along the walls away from the corner promote a relatively low streamwise velocity compared with the streamwise velocity at the corner bisector, explaining the distorted velocity contours. So by creating the off diagonal Reynolds stresses, ejection events contribute much to the generation of this secondary flow field. An instantaneous secondary flow field is given in Figure 3.9, on which some ejections can be seen on the walls away from the corners.

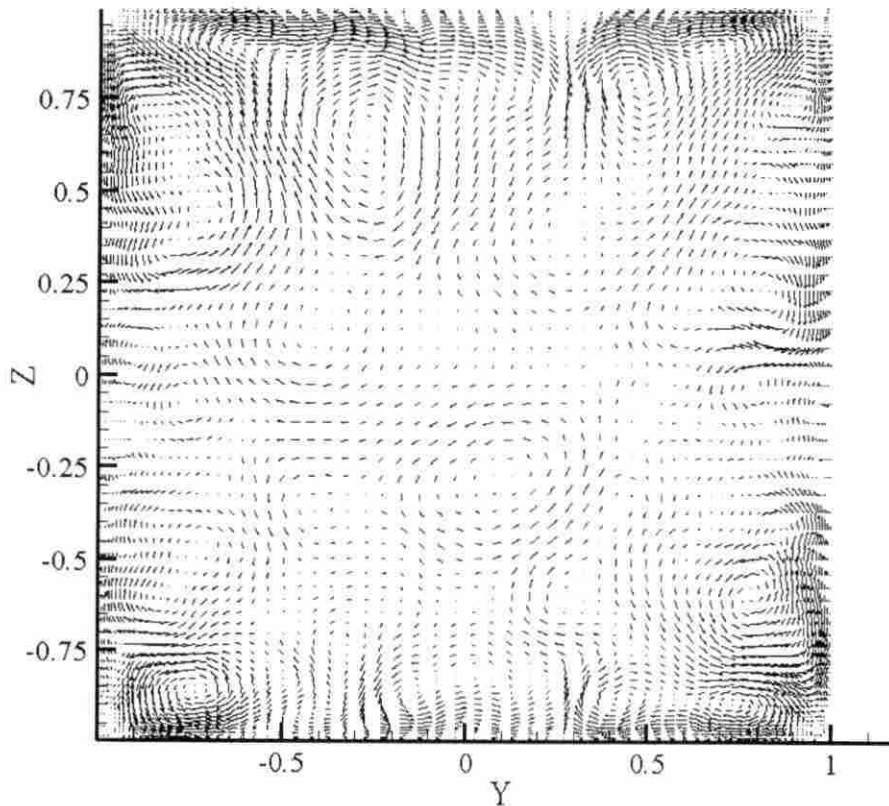


Figure 3.9 Instantaneous secondary flow field

3.4.2 Turbulence Statistics

Turbulent statistics, in many aspects, can show whether a simulation has captured the structure of the turbulent flow. Reynolds shear stress, for instance, can show evidence of the turbulent production events inside the flow to a very good extent. So this information is important to obtain and present in a successful prediction. The following paragraphs will discuss the turbulence statistics.

In this simulation, turbulence statistics were collected in the following way:

$$u_{i,rms} = \left\langle \sqrt{\left\langle \left(\tilde{u}_i(x, y, z, t) - \bar{\tilde{u}}_i(y, z, t) \right)^2 \right\rangle_x} \right\rangle_t \quad (3.26)$$

$$\overline{u'_i u'_i} = \left\langle \left(\tilde{u}_i(x, y, z, t) - \bar{\tilde{u}}_i(y, z, t) \right) \left(\tilde{u}_i(x, y, z, t) - \bar{\tilde{u}}_i(y, z, t) \right) \right\rangle_{x,t}, \quad (3.27)$$

where $\langle \rangle$ denotes ensemble averaging with respect to time or direction, and subscript x means averaging in the streamwise direction and the subscript t represents time averaging.

Figure 3.10 shows the streamwise turbulence intensity with respect to distance along the bisector A for a bulk Reynolds number of 6000. The results of Gavrilakis (1992) are also included for comparison purposes. Both results have been normalized by friction velocity. Very good agreement has been reached in this simulation, which shows that large eddy simulation with a simple localized dynamic model, plus proper grid resolution, is able to predict well the structure of wall bounded turbulent flow in a duct. Large eddy simulation again proves to be a powerful predictive tool. The slope of u_{rms} near the wall is steeper than that of DNS result, which is regarded as the effect of Reynolds number. An overshooting exists at the peak value for LES and this may be due to lack of resolution in the streamwise direction of the numerical grid.

Furthermore, streamwise turbulence intensity is shown in Figure 3.11 with respect to the wall units along the bisector A. The maximum of u_{rms} , as expected, occurs at $y^+ \approx 15$, which verifies that buffer zone is where most of the turbulence production

takes place. In both the viscous sublayer and the law of the wall regions, the turbulence intensity drops very quickly from its peak value.

The streamwise turbulence intensity along the wall bisector for $Re_b = 8000$ is also shown in Figure 3.12. A similar trend is found as the former case except that the peak value moves closer to the wall due to the Reynolds number effect. The peak value of u_{rms} is also found to be at around $y^+ \approx 15$ for $Re_b = 8000$, as shown in Figure 3.13.

Through Fig. 3.14 to 3.17, v_{rms} and w_{rms} distributions for both Reynolds numbers are shown. Good agreement is found in every figure, which further verifies the ability of LES to make accurate prediction for turbulent duct flow.

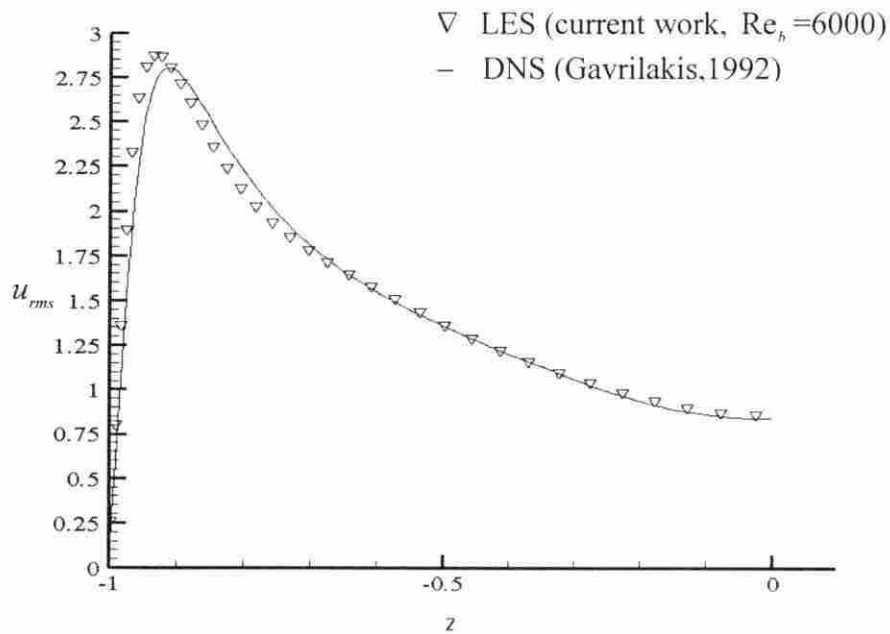


Figure 3.10 u_{rms} along the bisector A, $Re_b = 6000$

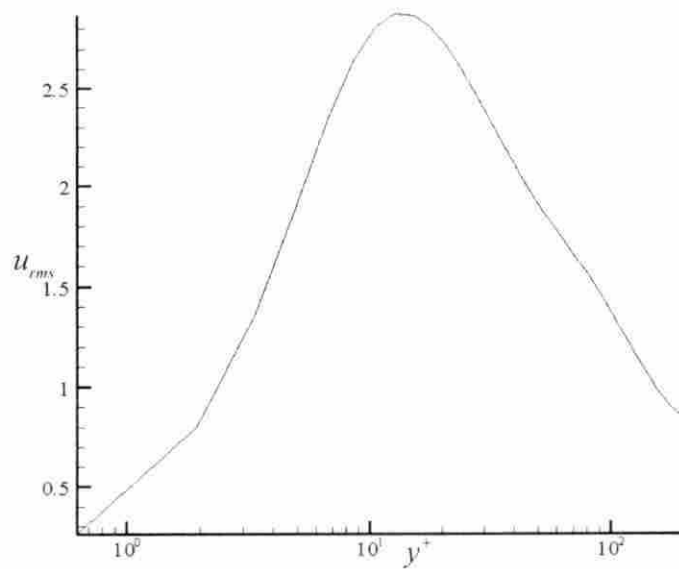


Figure 3.11 u_{rms} along the bisector A in wall units for $Re_b = 6000$

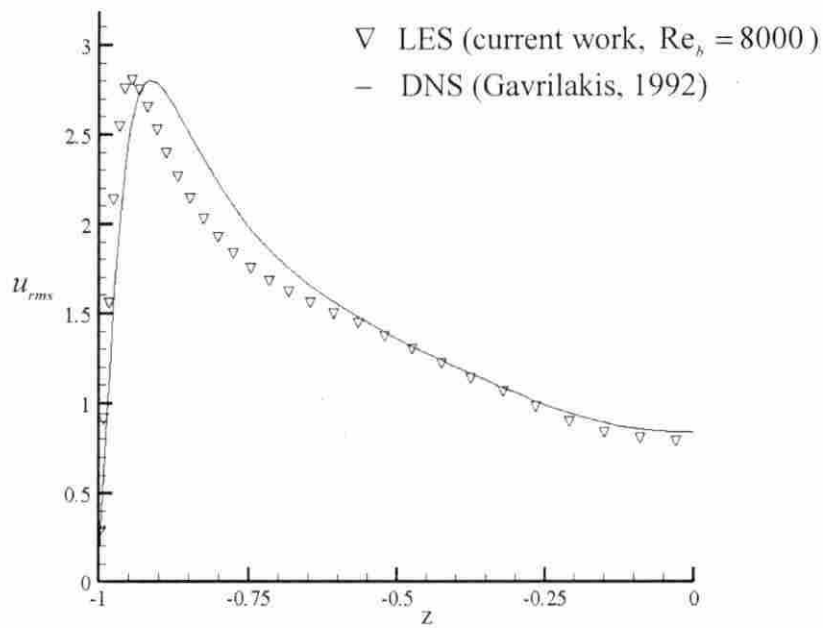


Figure 3.12 u_{rms} along the bisector A, $Re_b = 8000$

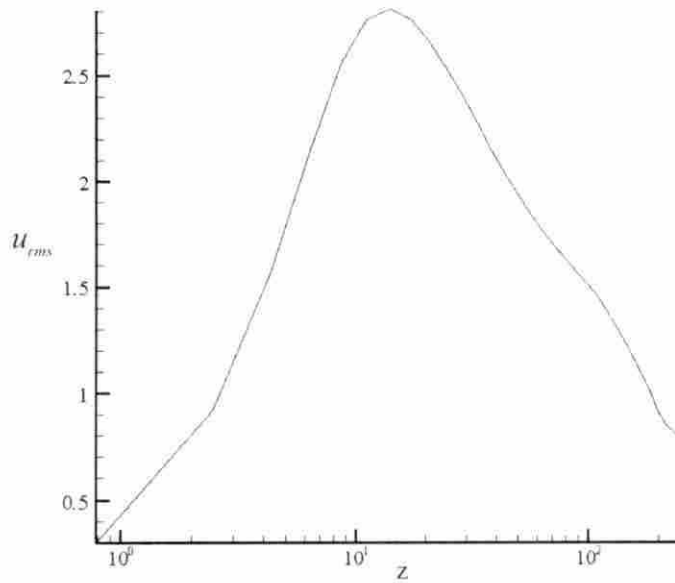


Figure 3.13 u_{rms} along the bisector A in wall units for $Re_b = 8000$

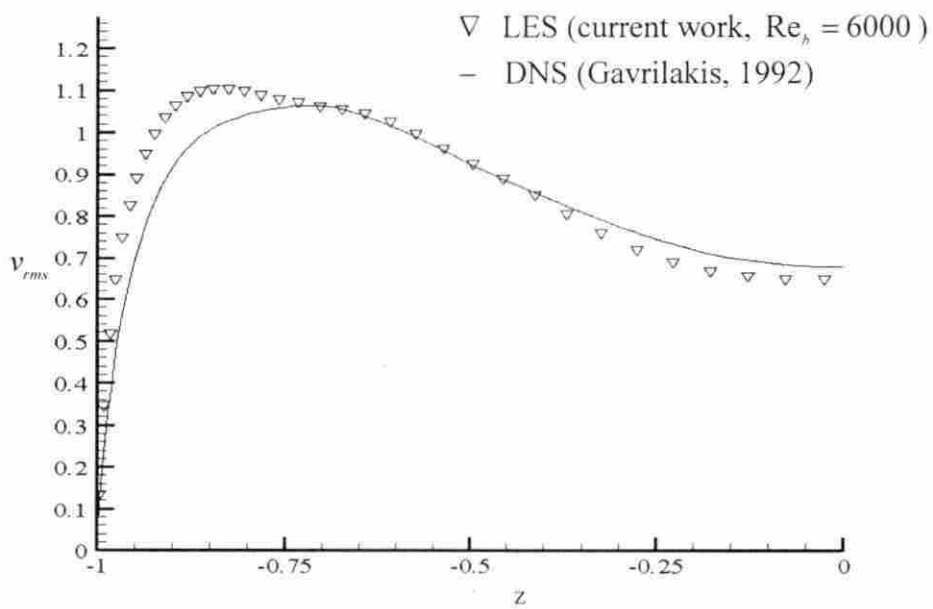


Figure 3.14 v_{rms} along the bisector A, $Re_b = 6000$

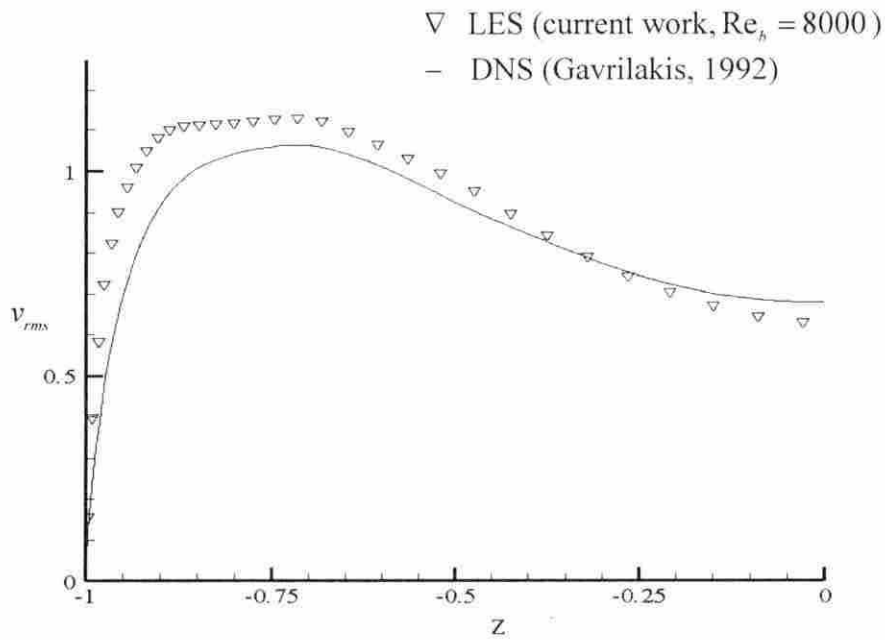


Figure 3.15 v_{rms} along the bisector A, $Re_h = 8000$

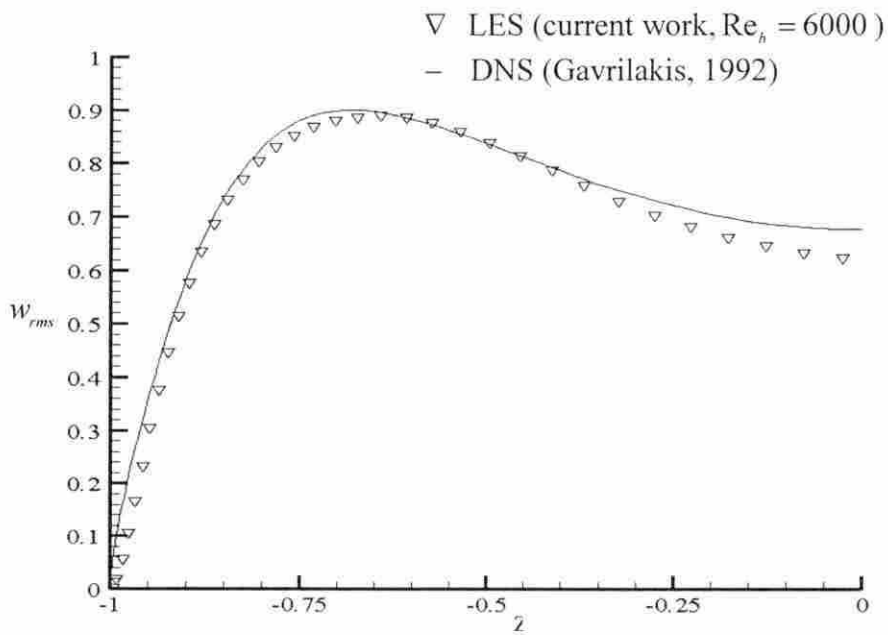


Figure 3.16 w_{rms} along the bisector A, $Re_h = 6000$

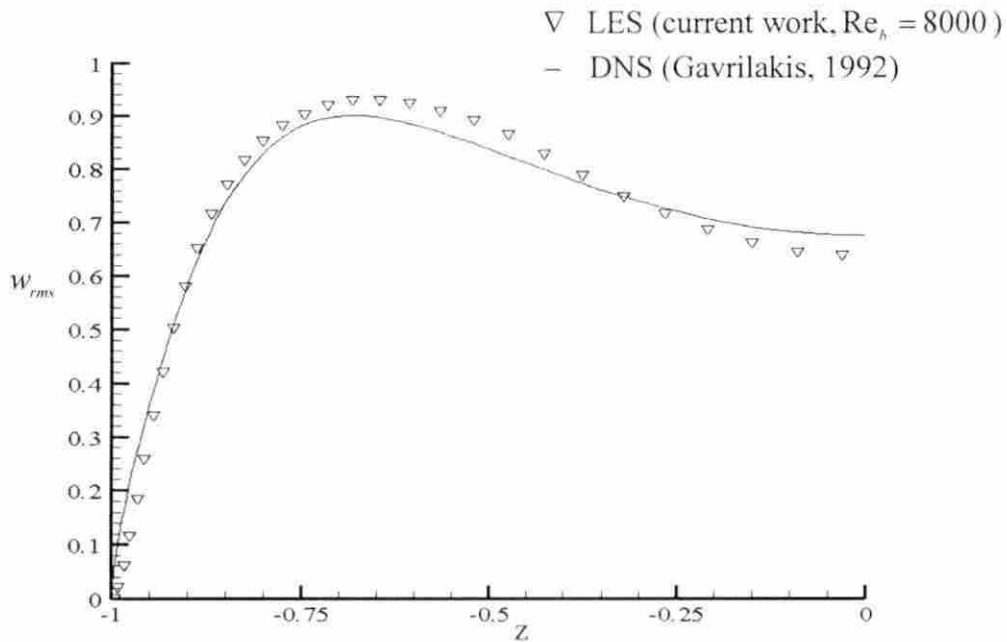


Figure 3.17 w_{rms} along the bisector A, $Re_b = 8000$

Figure 3.18 shows the contours of the Reynolds stress, $\overline{u'v'}$, for $Re_b = 6000$, which shows that the maximum magnitude of $\overline{u'v'}$ occurs at the middle of the two vertical walls in the figure. Since $\overline{u'v'}$ is mainly responsible for the turbulent transport of momentum in the flow, the figure shows where the turbulent production is the most intensive. Considering the symmetry in the flow, the maximum values of $\overline{u'w'}$ should occur at the middle of the two horizontal walls in the figure. So this means most of the ejection events happen at the middle of the wall, away from the corners. Because of the low shear stress at the corner, there is a net flow from the core region of the duct to the corners. Since the ejection events will move the fluid from the near wall region in the middle of the wall to the core region, there will be a flow from the corner to the middle. The above process can be continued as long as the ejection events are constantly happening, which is the case for turbulent flow with an external

energy supply. This explains how a secondary flow can be formed in a turbulent duct flow.

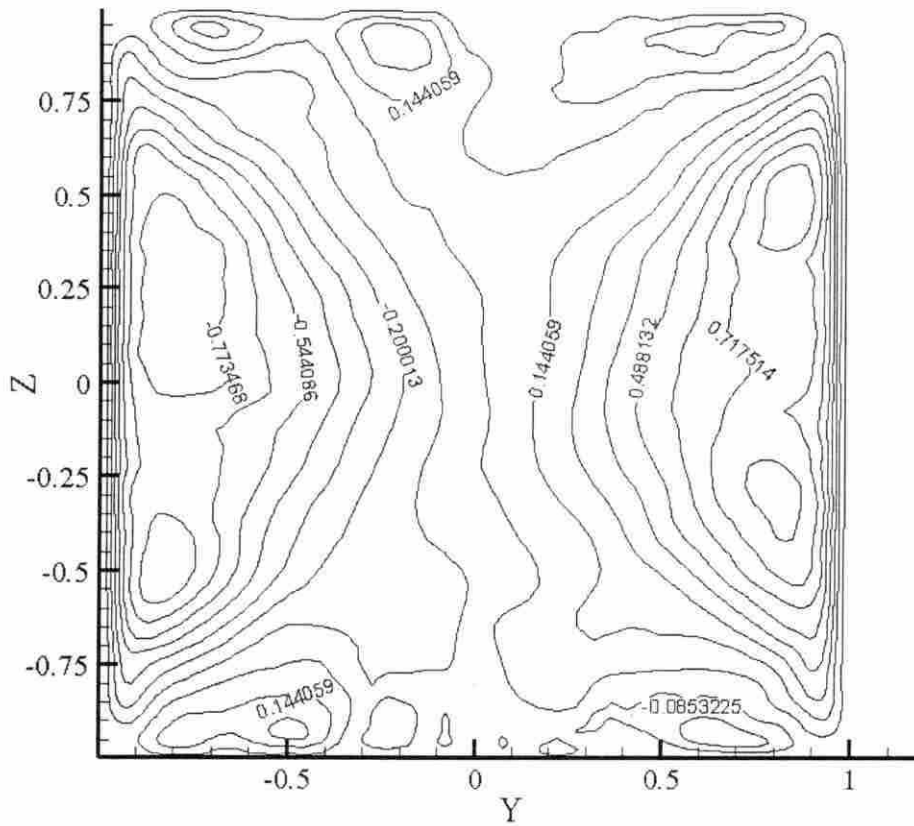


Figure 3.18 Contours of $\overline{u'v'}$ in the cross section

3.5 Conclusions

In this chapter, results were presented for the large eddy simulation of incompressible turbulent flow in a duct with square cross-section. A localized dynamic Smagorinsky model was used to account for the subgrid-scale contributions. A series of cases at different Reynolds numbers were simulated. The flow was assumed to be fully developed so that periodic boundary condition could be applied, which greatly conserves the required computation resources and simplifies the problem. Since turbulent flows at different Reynolds numbers will have different integral length scales, these cases employ different domain dimensions and correspondingly grid sizes, as shown in Table 3.1.

Due to the similarity of the results, mean flow results were only shown for $Re_h = 6000$ case, and turbulent statistics were shown for both $Re_h = 6000$ and $Re_h = 8000$ cases. Through comparison with results of direct numerical simulation by Gavrilakis (1992), the mean streamwise velocity was found to have been predicted well, both qualitatively and quantitatively. The structure of the boundary layer in the duct, including the viscous sublayer, buffer zone, and the law of the wall region, was captured very well, and consistent with that of Huser and Biringen (1993). The signature of turbulent duct flow – secondary flow field composed of four counter-rotating cells was predicted correctly, although the maximum magnitude of the secondary flow was smaller than that of the DNS results obtained at a lower Reynolds number. This indicates that LES can play an important role in predicting the characteristics of wall bounded turbulent flows in a duct.

Turbulent statistics are further shown to validate the simulation. Again, they are compared with results from Gavrilakis. Excellent agreement was observed between the two results, which strengthens the point that LES is a powerful tool even in capturing the characteristics of turbulent flows. The maximum values of streamwise turbulent intensity for both cases are found to occur in the buffer zone at around

$y^+ = 15$. This is very consistent with the classical turbulence theory about turbulent production.

In this chapter, an explanation for the formation of secondary flow in the cross-section was attempted. It is believed that the ejection events drive the flow near the middle of the wall to the core region of the flow, while the low shear stress at the corners induces a net flow from the core region to the corners. To conserve mass in the cross-section, a net transfer of fluid from the corners to the middle of the wall is formed, which combined with above fluid motions, forms a confined flow zone – or a cell. Each corner can produce two such zones that are counter rotating to each other and the flow field is shown as Figure 3.6. So ejection events are the driving force for the formation and existence of secondary flow field. This is consistent with the explanation of Huser and Biringen (1993).

CHAPTER 4. LARGE EDDY SIMULATION OF FULLY DEVELOPED TURBULENT ROTATING DUCT FLOWS

4.1 Introduction

Turbulent rotating flows are of considerable interest in a variety of industrial, geophysical and astrophysical applications. Examples are natural flows like ocean currents, estuaries, and atmospheric boundary layers, and engineering flows in rotating devices such as turbines, pumps, compressors, and cyclone separators. System rotation is well known to affect both the mean motion of the fluid and the turbulence statistics. Many rotational-induced flow phenomena have been reviewed by Tritton (1978, 1985) and Hopfinger (1989).

System rotation influences turbulence in several ways: for example, it may decrease the energy transfer from large scales to small scales or reduce the turbulence dissipation and decay rate of turbulent kinetic energy. In a rotating duct, system rotation both stabilizes and destabilizes the flow. On the stabilized side, turbulence production is suppressed by the Coriolis force and turbulence intensity is observed to be reduced. At the same time, the Coriolis force enhances the turbulence production and increases the turbulence intensity on the destabilized side. The other two walls perpendicular to the axis of rotation are providing the transition between the stabilized and destabilized sides.

Up to now, the literature on turbulent rotating duct flows is quite limited. There has not been any report on direct numerical simulation of such flows, while Pallares and Davidson (2000) and Murata and Mochizuki (2000, 2001) are among the limited researchers who have reported large eddy simulation of rotating duct flows.

Experiments wise, Han et al. (1994) and Bons and Kerrebrock (1999) are among the many who conducted experiments on this topic. However, the information that can be obtained from experiments is quite limited, usually restricted to surface averaged friction factor or heat transfer coefficients, and this has limited the practical application of experimental data to aid the optimal design of a cooling system. So the motivation of this work is to further expand the capability of numerical methods to correctly predict the phenomena in rotating ducts to aid the industrial design and understand the physics of the flow. Large eddy simulation, in which all large scales are computed accurately and small scales are modeled, seems to be a good candidate for this purpose.

So for this reason, large eddy simulations of rotating duct flows were performed and their results are presented in this chapter. Both mean flow results and turbulence statistics are reported to further aid understanding of the characteristics of the flow. Due to the lack of detailed data, most of the results will only be compared in a qualitatively sense, rather than quantitatively.

4.2 Problem Description

This simulation will be for incompressible fully developed duct flow, as described in Chapter 3, except for a system rotation around the axis parallel to the z direction, as shown in Fig. 4.1. In this simulation, the localized dynamic Smagorinsky model utilized in the non-rotating flow will still be used. Although system rotation exists in the flow, it is believed that a dynamic procedure is able to adjust the model so that the subgrid-scale stress can be predicted well on both stabilized and destabilized sides. This has been shown by Meng (2000).

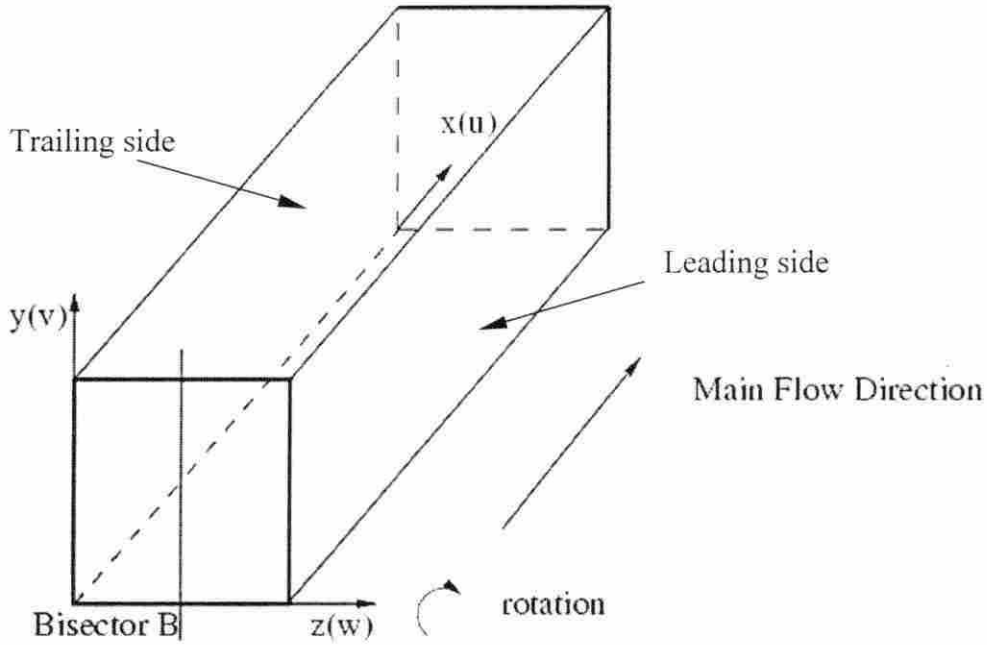


Figure 4.1 Geometry of the domain

The governing equations for this problem are almost the same as those of its non-rotating counterpart, except that there exists a term in the momentum equation to account for the contribution of Coriolis force to the momentum. The contribution of Coriolis force to the energy equation can be absorbed into the neglected terms and is neglected here. By using the effective streamwise pressure gradient β to ensure a constant mass flow rate in the duct, the centrifugal effects are accounted for and do not appear explicitly in the governing equations. So the governing equations after filtering can be shown as below in nondimensional form.

$$\frac{\partial \bar{p}}{\partial t} + \frac{\partial \bar{p} \tilde{u}_i}{\partial x_i} = 0 \quad (4.1)$$

$$\frac{\partial \bar{p} \tilde{u}_i}{\partial t} + \frac{\partial \bar{p} \tilde{u}_i \tilde{u}_j}{\partial x_j} = -\frac{\partial \bar{p}}{\partial x_i} + \frac{\partial \hat{\sigma}_{ij}}{\partial x_j} - \frac{\partial \tau_{ij}}{\partial x_j} + \varepsilon_{jil} Ro \tilde{u}_j \quad (4.2)$$

$$\frac{\partial \bar{\rho} \hat{E}}{\partial t} + \frac{\partial \left[(\bar{\rho} \hat{E} + \bar{p}) \tilde{u}_j \right]}{\partial x_j} = - \frac{\partial \tilde{u}_i \hat{\sigma}_{ij}}{\partial x_j} - \frac{\partial \hat{q}_j}{\partial x_j} - \frac{\partial Q_j}{\partial x_j} - \alpha - \pi + \varepsilon. \quad (4.3)$$

The definition of the terms in these equations have been given in Chapter 3, except $\varepsilon_{j13} Ro \tilde{u}_j$, which represents the role of Coriolis force in momentum equation. ε_{j13} is the Levi-Civita symbol defined as

$$\varepsilon_{ijk} = \begin{cases} 0, & \text{if any two labels are the same} \\ 1, & \text{if } i, j, k \text{ is an even permutation of } 1, 2, 3 \\ -1, & \text{if } i, j, k \text{ is an odd permutation of } 1, 2, 3 \end{cases} \quad (4.4)$$

and Ro is the rotation number based on bulk velocity and duct height as

$$Ro = \frac{\Omega D}{U}. \quad (4.5)$$

Since rotation is in the spanwise direction, it will only influence the momentum in the x and y directions. The contribution to the streamwise momentum by the Coriolis force is $-Ro \tilde{v}$, which is negligibly small compared to the streamwise pressure gradient as a body force since \tilde{v} is very small. On the other hand, the Coriolis force's contribution, $Ro \tilde{u}$, is important in the cross stream momentum equation since this term is two orders of magnitude larger than its streamwise counterpart and there are no other body force terms in the cross stream direction. It is this component of the Coriolis force that transports the low momentum fluid from the stable side (pressure side, trailing side) to the unstable side (suction side, leading side) along the two walls parallel to the rotation axis. To maintain conservation of mass in the cross-section, a net fluid flow from the leading side to the trailing side through the core region is formed, which carries high momentum of the core and increases the turbulence level on the trailing side. Thus, the flow in the cross section will form a pair of rotating cells called Taylor – Görtler vortices, analogous to those that develop due to the centrifugal instability arising from streamline curvature. Meanwhile, at high rotation speeds, a Taylor-Proudman regime occurs in the flow, which is characterized by the fact that axial velocity does not change along the direction of

axis of rotation. So together with the secondary flow of the second kind developed in the cross-section of turbulent duct flow, the turbulent flow in a rotating duct has very complicated characteristics.

The periodic boundary condition is still used for this study, as in the non-rotating case. Since the flow is incompressible, both velocity components and temperature are periodic:

$$\begin{aligned}
 \tilde{u}(0, y, z, t) &= \tilde{u}(L_x, y, z, t) \\
 \tilde{v}(0, y, z, t) &= \tilde{v}(L_x, y, z, t) \\
 \tilde{w}(0, y, z, t) &= \tilde{w}(L_x, y, z, t) \\
 \tilde{T}(0, y, z, t) &= \tilde{T}(L_x, y, z, t)
 \end{aligned} \tag{4.6}$$

where L_x is the streamwise length of the domain. Pressure is step periodic, which means it can be decomposed into the combination of a periodic component and an aperiodic component as

$$\bar{p}(x, y, z, t) = \beta x + \bar{p}_p(x, y, z, t), \tag{4.7}$$

where β is the effective streamwise pressure gradient parameter, in that it absorbs the centrifugal force in the streamwise direction. Thus in incompressible flows, βx naturally takes into account the centrifugal force in x direction, and this can explain why a much higher effective pressure gradient, β , was observed during the simulation than the non-rotating case. Subscript p denotes periodic component that satisfies

$$\bar{p}_p(0, y, z, t) = \bar{p}_p(L_x, y, z, t). \tag{4.8}$$

The effective streamwise pressure gradient parameter is adjusted at each time step to achieve the desired mass flow rate, which is

$$\beta^{n+1} = \beta^n - \frac{1}{\Delta t} \left[\left(\frac{\dot{m}}{A_c} \right)^0 - 2 \left(\frac{\dot{m}}{A_c} \right)^n + \left(\frac{\dot{m}}{A_c} \right)^{n-1} \right], \quad (4.9)$$

where Δt is the physical time step, \dot{m} is the mass flow rate and A_c is the cross-section area.

4.3 Simulation Details

The simulation of rotating duct flows was initiated using the data from non-rotating duct flow simulation at the same Reynolds number. The method of generation of the numerical grid was the same as for the non-rotating case.

Through this simulation, it was hoped to learn about the influence of both the Reynolds number and rotation number on the characteristics of rotating duct flow. For this reason, three cases were simulated and they are described in Table 4.1, in which δ is half the diameter of the duct.

The physical time step used in these rotating cases was the same as in the non-rotating cases, 0.01. Since the average friction velocity is significantly increased by system rotation, only 12,000 physical time steps were used to collect mean flow data and turbulent statistics. Meanwhile, the global averaged turbulent kinetic energy was observed to decline to a much lower level compared with the non-rotating case, which

Table 4.1 Case description for the rotating duct simulation

	Re_b	Ro	Domain	Grid
Case I	8,000	0.048	$14.1\delta \times 2\delta \times 2\delta$	$108 \times 72 \times 72$
Case II	8,000	0.144	$14.1\delta \times 2\delta \times 2\delta$	$108 \times 72 \times 72$
Case III	10,000	0.144	$6.4\delta \times 2\delta \times 2\delta$	$72 \times 72 \times 72$

was not observed in the rotating channel case, as noted by Meng (2000a). The data collecting method was the same as the non-rotating duct case, because it was believed that rotation would not influence the homogeneity in the streamwise direction. The results of all these three cases are provided to investigate the influence of both Reynolds number and rotation number on rotating duct flow, with the emphasis on rotation number. The whole domain was divided into 12 blocks for both $Re_b = 8,000$ and $Re_b = 6,000$ cases and 8 blocks for the $Re_b = 10,000$ case. The simulations were run on the Origin 2000 and Origin 3800 using MPI.

4.4 Results and Discussion

4.4.1 Effects of Rotation on Mean Flow Structure

Since the Coriolis force transports high momentum fluid from the core region to the trailing side and low momentum fluid from the boundary layer near the trailing side to the leading side, the streamwise velocity distribution is altered compared with the non-rotating case. Fig. 4.2 shows the streamwise velocity profile along the wall bisector B, which is perpendicular to the axis of rotation, for the $Ro = 0.048$ case. The trailing side is on the right and the leading side on the left, and the streamwise velocity is normalized by the friction velocity. It can be seen that peak value of the profile is shifted toward the trailing side. And the velocity gradient on the trailing side is larger than that on the leading side, which means the friction velocity will be higher on the trailing side. This effect is increased with rotation number, as shown in Fig. 4.3 for the $Ro = 0.144$ case.

As well as the streamwise velocity, the friction velocity distribution also experiences this effect. It is higher than that of the non-rotating case on the trailing

side as the streamwise velocity gradient is higher on the trailing side, and it is lower on the leading side. Through Fig. 4.4, it can be seen that for the $Ro = 0.048$ case there is an obvious, though not significant, difference between the friction velocity distributions on the leading side and the trailing side. The friction velocity distribution for non-rotating case lies between these two distributions. As for the $Ro = 0.144$ case presented in Fig. 4.5, the difference between the trailing side and leading side is much more apparent and significant with the average value on the trailing side being around twice that on the leading side. The above phenomena show that Coriolis force plays an important role in changing the flow field in a rotating-duct and this effect is increasing with the increase of rotation number.

The effects of Coriolis force are more easily seen by viewing streamwise velocity contours and secondary flows. In Fig. 4.6, which shows the streamwise velocity contours of the $Ro = 0.048$ case, it can be seen that the contours are slightly shifted to the trailing side and they bulge more toward the corners on the trailing side than on the leading side. Through the secondary flow field shown in Fig. 4.7, it is apparent that the secondary flow composed of four pairs of counter-rotating cells has been altered. On the leading side, each pair loses a cell and the remaining one is much larger than those on the trailing side. However, the well-known two counter rotating cells in the whole cross section are not formed yet and this may have something to do with the relatively low rotation number. When $Ro = 0.144$, the effects of the Coriolis force become more significant. Contours are shifted more to the trailing side compared with $Ro = 0.048$ case as can be seen in Figure 4.8. Two interesting features can be observed. Firstly, instead of one, two peak values of streamwise velocity are found in the figure. This is consistent with the findings of Pallares and Davidson (2000). The asymmetry between the two peak values may be induced by numerical errors in the scheme. Secondly, in the core region of the flow, a few straight vertical isovels are found, which means that, in this case, streamwise velocity does not change with respect to z , the direction parallel to the axis of rotation. This region is defined

as the Taylor-Proudman regime. There also exist two large bulges near the end of the leading side, and this can be explained through the secondary flow in the cross-section presented in Fig. 4.9 since the pair of counter rotating Taylor- Görtler vortices has been formed. Through its moving from trailing side to leading side, some high momentum fluids are also entrained into the cell and transported to the leading side, which increases the streamwise velocity of the fluid near the leading side and creates two large bulges there. As shown, the original secondary flow in the non-rotating duct has been totally destroyed and the cross-section is dominated by the Taylor- Görtler vortices. Also, a couple of minor and weak vortices are also found near the trailing side, which is the remaining effect of the corner, as in non-rotating case.

In summary, the Coriolis force greatly alters the structure of mean flow field in a turbulent rotating duct compared with a non-rotating duct. The streamwise velocity contours are shifted toward the trailing side and the friction velocity distribution has higher values on the trailing side. As the rotation number increases, a Taylor-Proudman regime is formed which is characterized by the feature that streamwise velocity does not change with respect to the direction parallel to the axis of rotation. Also, peak values of streamwise velocity are found to exist at two different locations, instead of one, the reason for which has not been explained clearly. Well documented Taylor- Görtler vortices are found for the higher rotation number case and they play an important role in influencing the structure of the flow field in the duct.

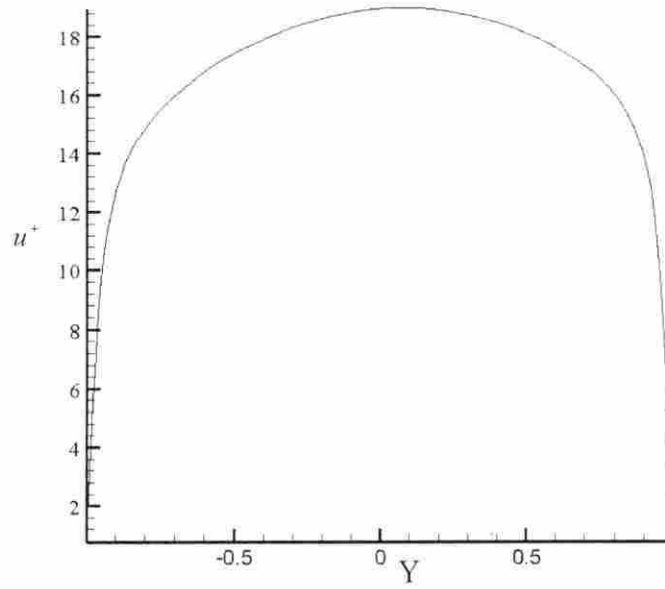


Figure 4.2 Streamwise velocity along bisector B for $Ro = 0.048$

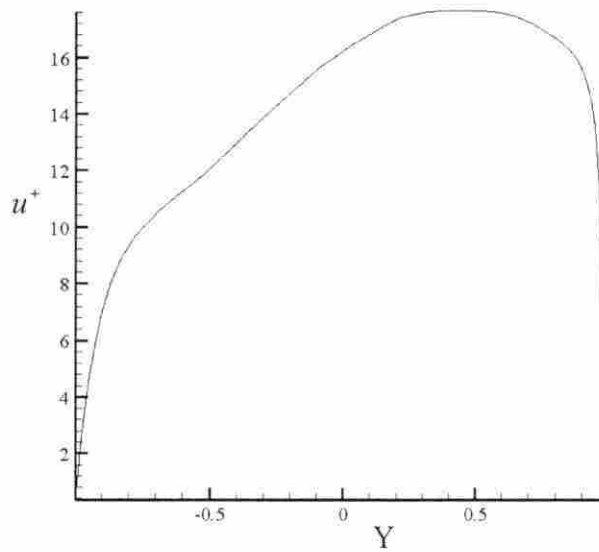


Figure 4.3 Streamwise velocity along bisector B for $Ro = 0.144$

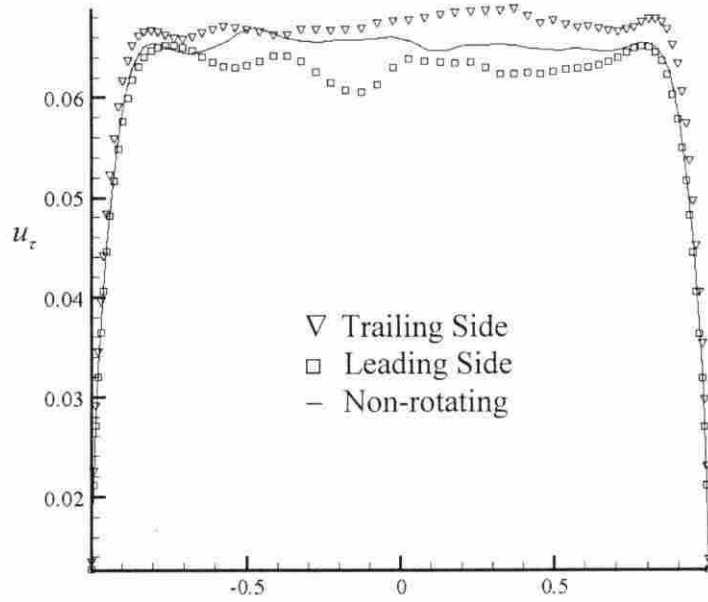


Figure 4.4 Friction velocity distributions for $Ro = 0.048$

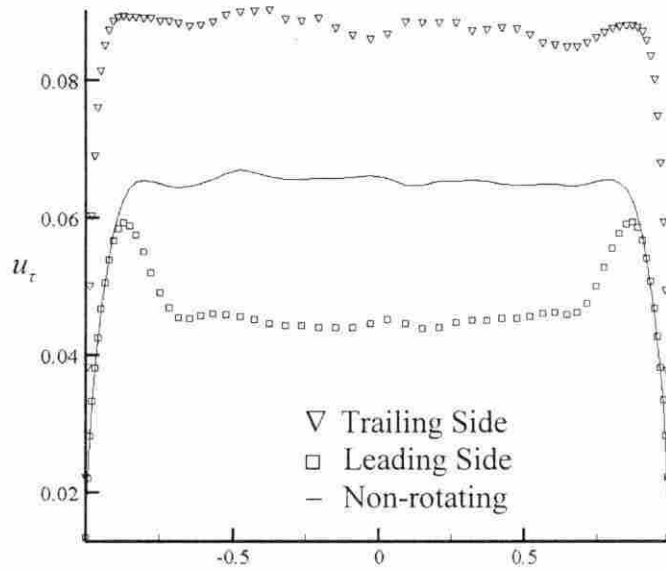


Figure 4.5 Friction velocity distributions for $Ro = 0.144$

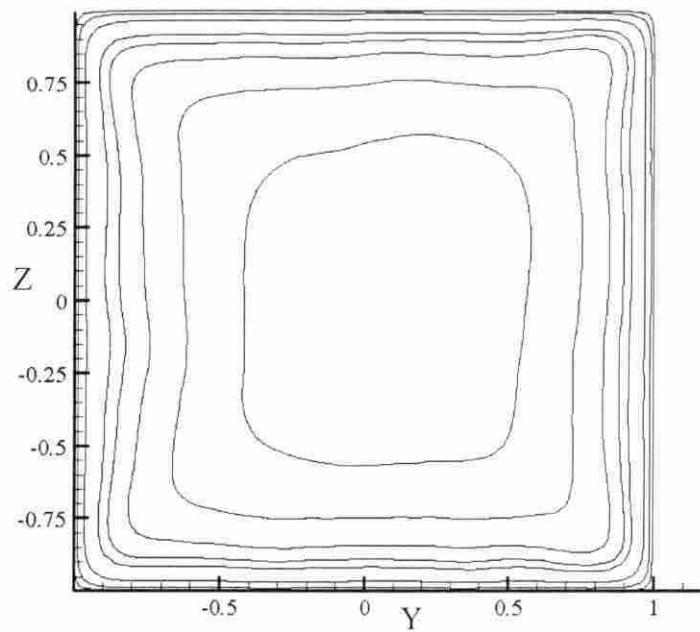


Figure 4.6 Streamwise velocity contours in the cross-section for $Ro = 0.048$

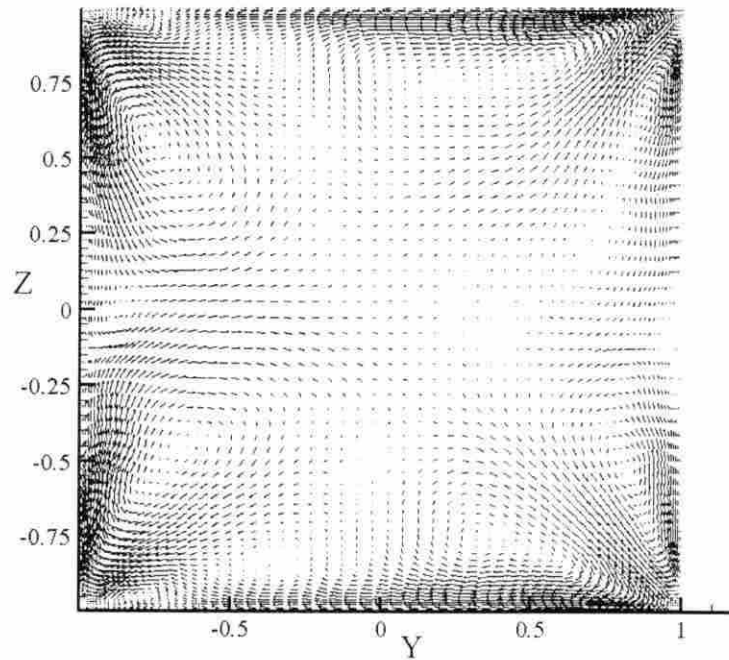


Figure 4.7 Secondary flow in the cross-section for $Ro = 0.048$

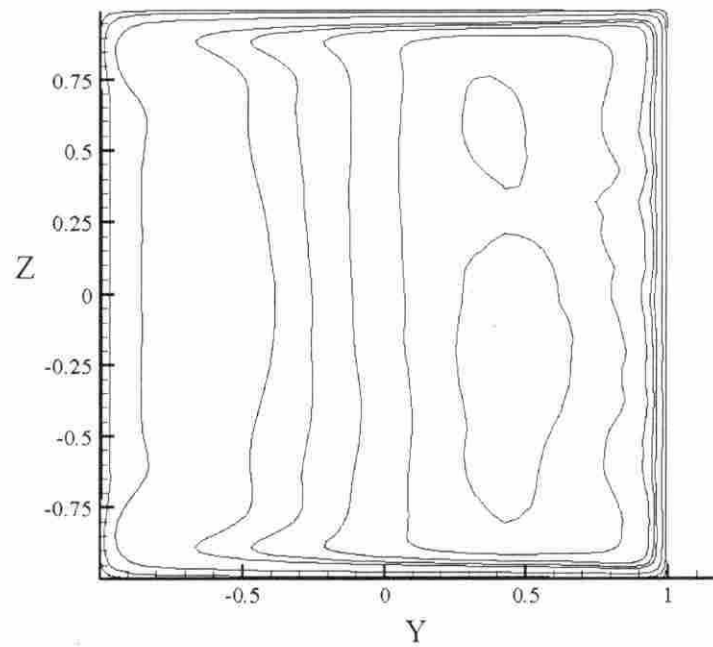


Figure 4.8 Streamwise velocity contours in the cross-section for $Ro = 0.144$

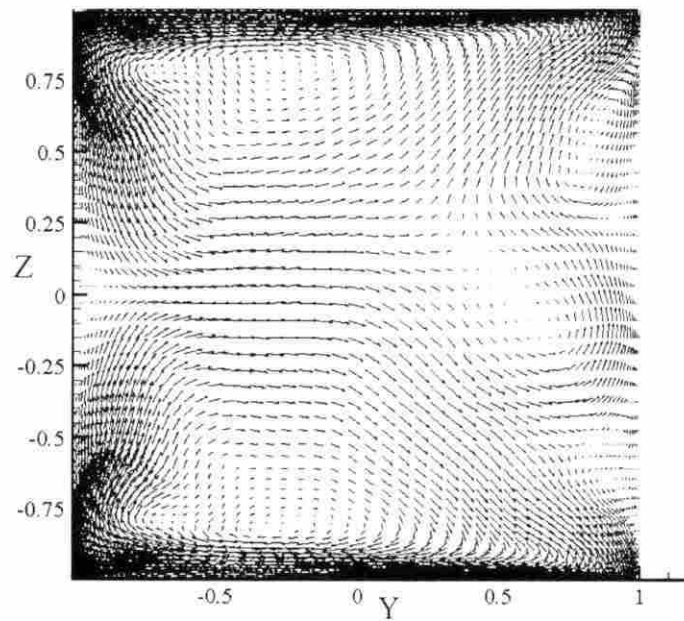


Figure 4.9 Secondary flow in the cross-section for $Ro = 0.144$

4.4.2 Effects of Rotation on Turbulence Statistics

As well as on mean flow field, rotation also has significant effects on the turbulence statistics. Rotation enhances the turbulence production and increases the turbulence level on the trailing side. On the other hand, turbulence production is suppressed and turbulence level is reduced on the leading side by the rotation effects. Figure 4.10 shows the turbulence intensity of the three velocity components for the $Ro = 0.048$ case. No major difference can be seen between the two sides except that the intensities on the trailing side are slightly higher than those on the leading side. This is because the rotation number is small and the effects of Coriolis force are not playing an important role in the flow. However, for the $Ro = 0.144$ case, the difference between the intensities on two sides is very obvious and significant, which is clearly shown in Fig. 4.11. The turbulence intensities are greatly reduced and the turbulent flow is almost laminarized on the leading side. Also, the level of turbulence is much enhanced on the trailing side. It is worth noting that compared with the non-rotating case, the turbulent intensity of the streamwise velocity is smaller in most parts of the flow. This is a sign of laminarization of the whole flow in the duct, except in the small region near the trailing side. To show this trend more clearly, the turbulent kinetic energy for $Ro = 0.144$ is around $0.7u_t^2$, which is only $1/3$ of that for the non-rotating case. This shows that rotation is suppressing the turbulence level in the rotating turbulent duct flow, which is not observed in the rotating turbulent channel case (Meng and Pletcher, 2000a). The same phenomenon was observed by Pallares and Davidson (2000). Compared with the non-rotating case, the pressure gradient in the streamwise direction was increased, which accounted for the streamwise centrifugal force.

Figures 4.12 and 4.13 show the contours of the Reynolds shear stress component $\overline{u'v'}$ for $Ro = 0.048$ and $Ro = 0.144$, respectively. For the $Ro = 0.048$ case, this term is slightly higher on the trailing side than on the leading side. However, for the

$Ro = 0.144$ case, a great difference can be observed with the values on the trailing side almost one order of magnitude higher than those on the leading side. As $\overline{u'v'}$ is mainly responsible for the generation of turbulence, these two plots vividly show that rotation suppresses turbulence production on the leading side and enhances turbulence production on the trailing side. And this effect increases with rotation number. For the $Ro = 0.144$ case, the small $\overline{u'v'}$ on leading side explains the laminarization of flow near the leading side. Furthermore, compared with the $Ro = 0.048$ case, $\overline{u'v'}$ has a smaller magnitude when $Ro = 0.144$, and this means the turbulence production in the whole duct is suppressed by rotation.

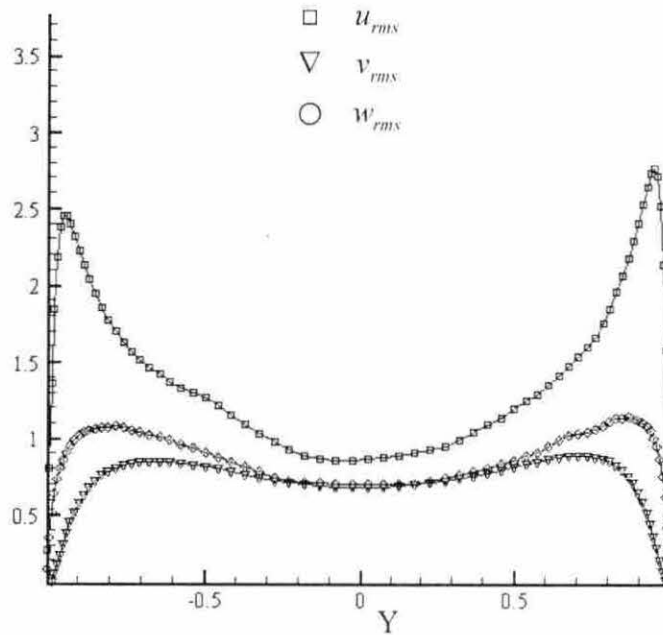


Figure 4.10 Distributions of turbulence intensities along bisector B for $Ro = 0.048$

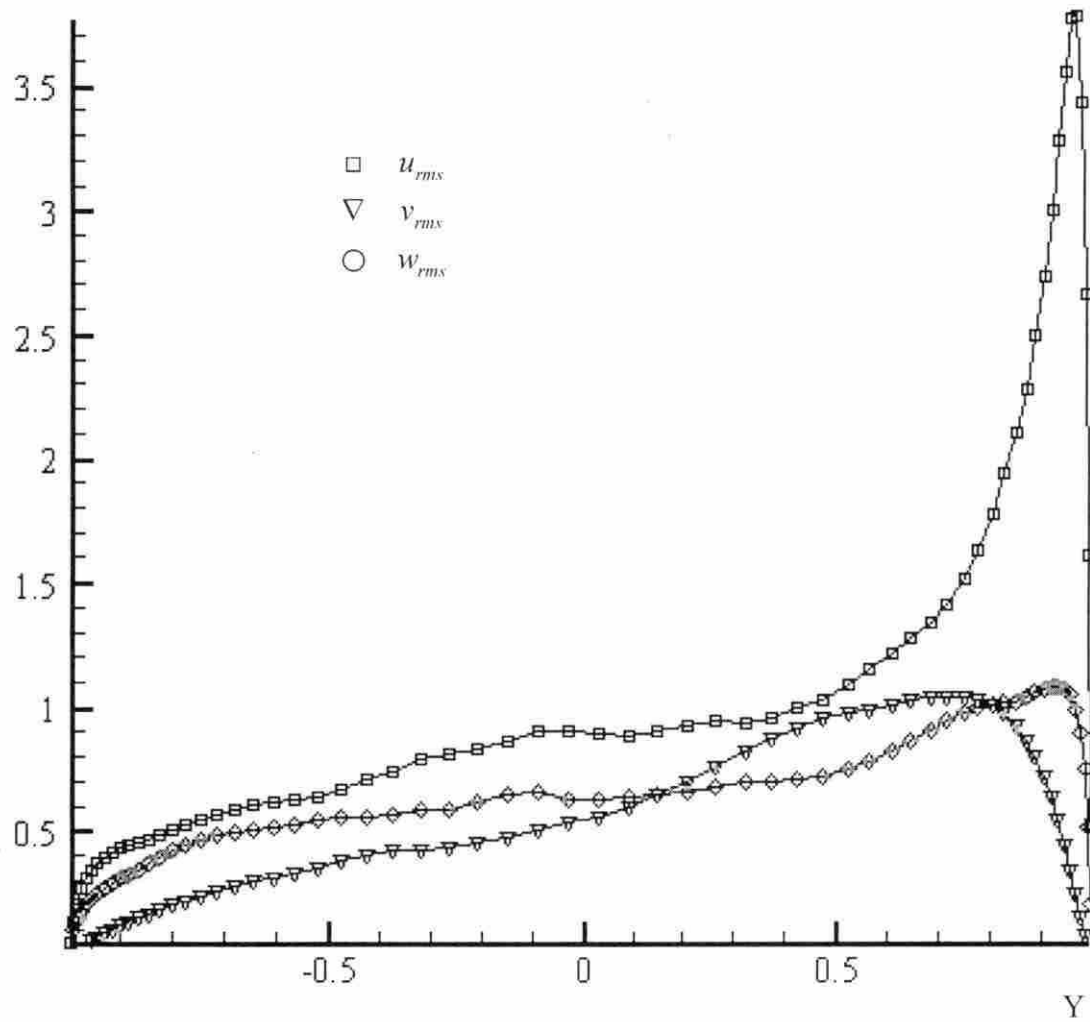


Figure 4.11 Distributions of turbulence intensities along bisector B for $Ro = 0.144$

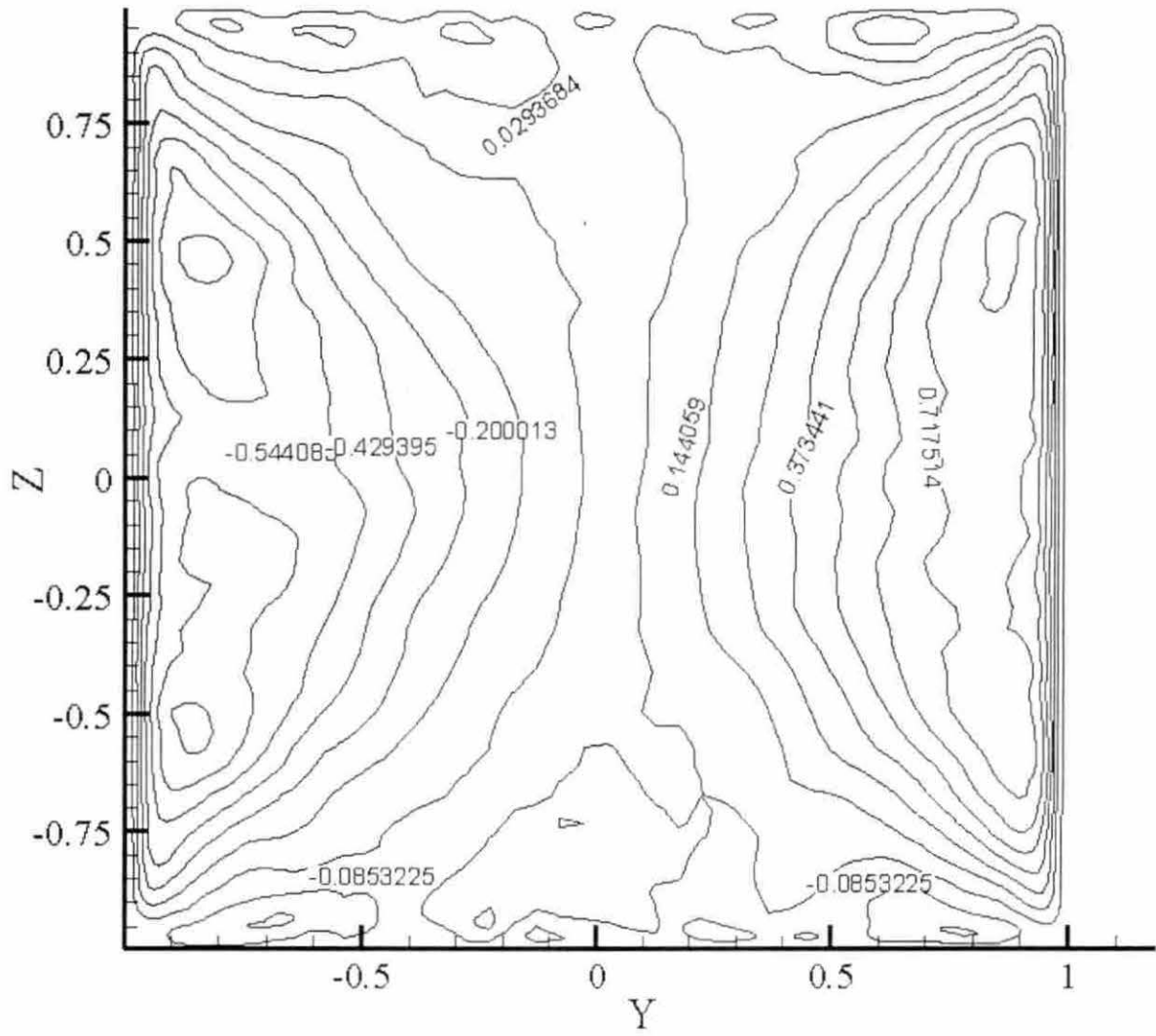


Figure 4.12 Contours of $\overline{u'v'}$ for $Ro = 0.048$

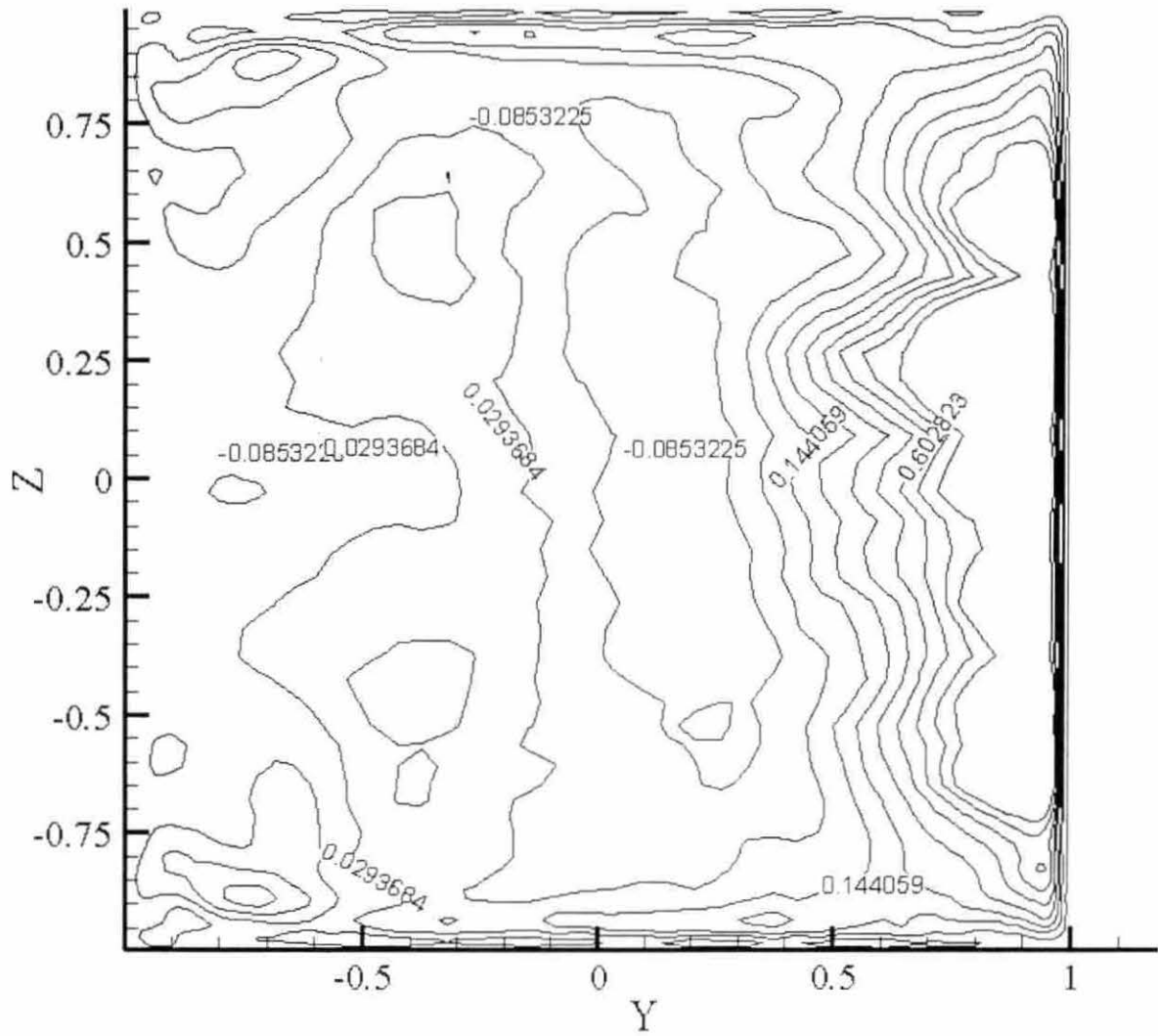


Figure 4.13 Contours of $\overline{u'v'}$ for $Ro = 0.144$

4.4.3 Effects of Reynolds Number on Rotating Duct Flow

In addition to rotation number, Reynolds number is another controlling parameter in the governing equations. So Reynolds number also controls the characteristics of rotating duct flow. For this reason, it is of interest to investigate the effects of Reynolds number on rotating duct flow. Two cases for $Ro = 0.144$ are simulated under different Reynolds numbers, with one at 8,000 and the other at 10,000. Their results are presented and compared here to study the effects of Reynolds number.

Fig. 4.14 shows the streamwise velocity distributions at these two Reynolds numbers along bisector B. Obviously, the peak of the profile is much closer to the trailing side for the $Re_b = 8,000$ case than for the $Re_b = 10,000$ case. The mean flow structure is less subjected to the rotational effects at higher Reynolds number than at lower Reynolds number. This also holds for turbulence statistics as shown in Figs. 4.15 – 4.17. For the turbulent intensity of every component, the difference between the values on the leading and trailing sides is smaller for $Re_b = 10,000$ case. This is also the case for $\overline{u'v'}$ plot in Fig. 4.18. So at higher Reynolds numbers, rotation has less influence on turbulence production and level of turbulence at both the leading side and the trailing side. In other words, at higher Reynolds numbers, the flow is less sensitive to rotation and is more able to preserve its characteristics as in the non-rotating case. So turbulent flow in a rotating duct tends to be more even and less asymmetric as Reynolds number increases. This trend was also captured in the experiments by Moore (1967). He found that by keeping the rotation number constant, the difference between the average friction factors on the trailing and leading sides tends to be smaller as Reynolds number increases. Friction is proportional to the square of the friction velocity, thus it is closely related to the mean flow structure and turbulence statistics distribution. So what Moore observed can also be interpreted as less asymmetry in the flow induced by rotation. Based on both simulation and experiments, it is safe to draw

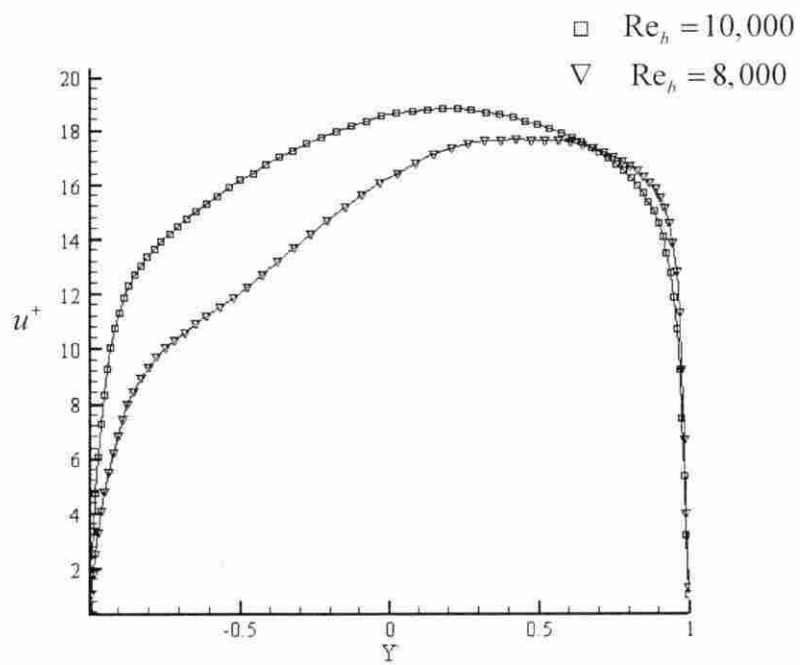
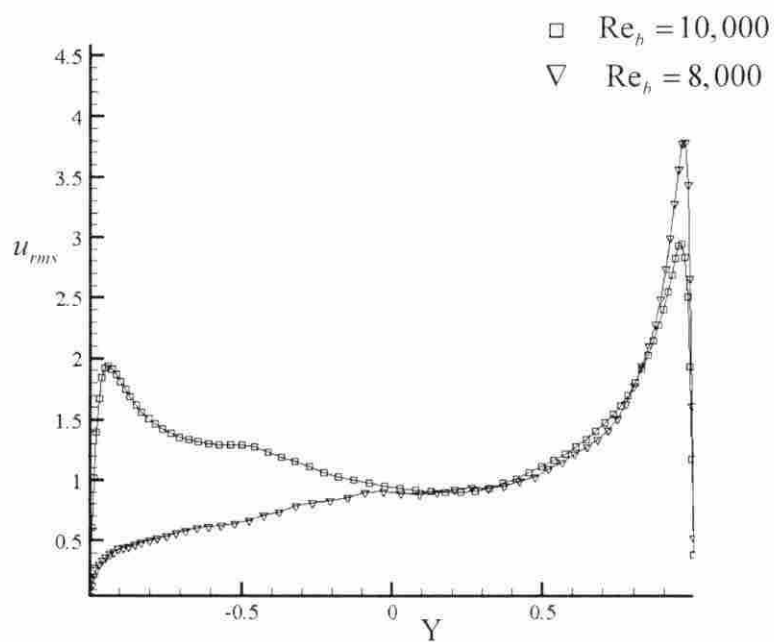
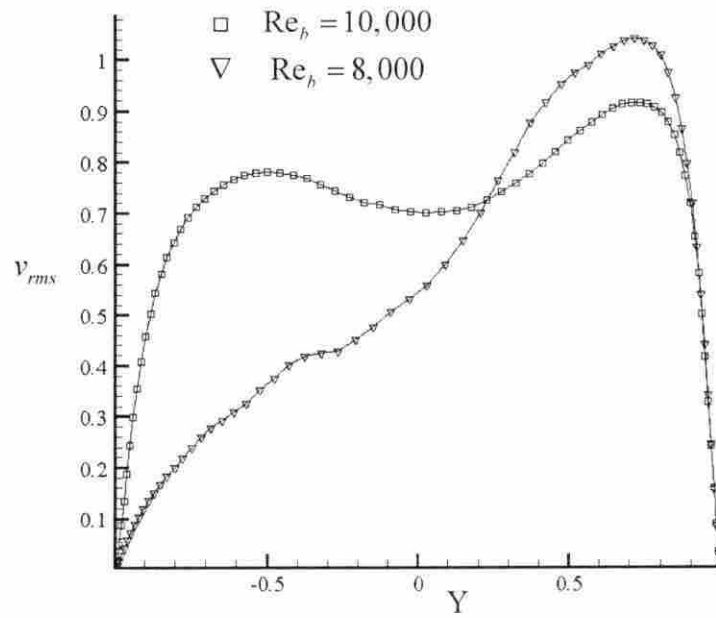
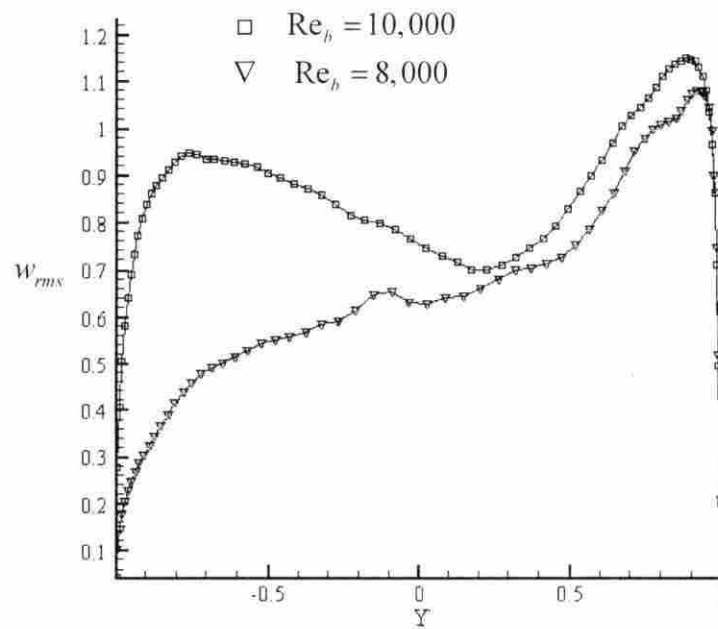


Figure 4.14 Streamwise velocity along bisector B

Figure 4.15 u_{rms} along the bisector B

Figure 4.16 v_{rms} along the bisector BFigure 4.17 w_{rms} along the bisector B

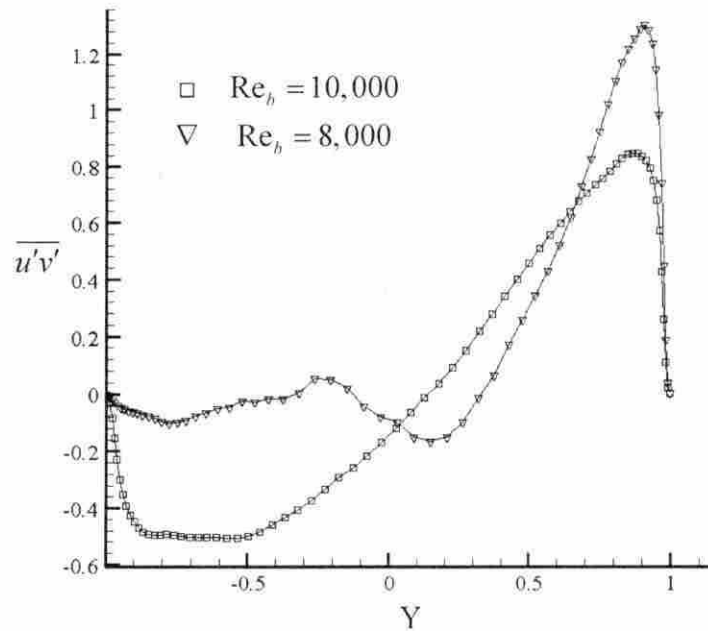


Figure 4.18 $\overline{u'v'}$ along the bisector B

a conclusion that a higher Reynolds number enables fluid through rotating duct to be less subjected to the influence of rotation.

4.5 Conclusions

In this chapter, simulation results were presented for three cases of turbulent flow through a rotating duct to investigate the influence of the rotation and Reynolds numbers on the flow. The simulations were initiated from the data of non-rotating cases and the numerical methods were almost the same as those described in Chapter 3. Through the investigation, several conclusions can be drawn.

Firstly, rotation has a strong influence on the mean flow field and this influence is an increasing function of rotation number. As the Coriolis force transports high speed fluid to the trailing side and low speed fluid to the leading side, the peak streamwise

velocity is shifted to the trailing side. As the rotation effect gets stronger, the peak region is split into two regions near the trailing side. Taylor- Görtler vortices and a Taylor-Proudman region are also observed in the case of a high rotation number.

Secondly, rotation has significant effects on the turbulence statistics as well. The turbulence level on the trailing side is one order of magnitude stronger than that on the leading side. The flow on the leading side can almost be considered as laminar due to the laminarization effect of the Coriolis force – an effect not observed in the rotating channel. Turbulence production is found to be much less active on the leading side than on the trailing side.

Thirdly and lastly, Reynolds number can also influence the flow in a rotating duct. Two cases at different Reynolds numbers but with the same rotation number were simulated to verify this. It was found that with a higher Reynolds number the difference in values of streamwise velocity, turbulence intensities and Reynolds shear stress between the two sides was significantly decreased. The same conclusion can be drawn from the experimental data of Moore (1967). So a higher Reynolds number makes the flow field less sensitive to rotational effects and leads to a less asymmetric flow field. And turbulence level is better preserved at higher Reynolds numbers.

CHAPTER 5. LARGE EDDY SIMULATION OF THE EFFECTS OF RIBS AND ROTATION ON HEAT TRANSFER IN A RIBBED CHANNEL

5.1 Introduction

The flow over two and/or three-dimensional obstacles of different shapes and sizes has been studied extensively by numerous investigators due to its importance to engineering applications. Among these are flows in turbines, pumps, diffusers and electronic components (Matsubara and Alfreson, 1996). In many of these applications, enhanced surfaces and rotation significantly alter the structure of the turbulence. Han et al. (1978) conducted an experimental study to investigate the effect of rib geometry on the friction factor and Stanton number for turbulent flow. It was found that the shape of the rib affected the friction factor, while a modest effect was observed on the heat transfer. Bergeles and Athanassiadis (1983) studied the influence of the streamwise length of a rib on reattachment length and showed that a sudden decrease in reattachment length from 11 to 3 rib heights was observed when the length to height ratio of a rib was greater than 4. Sparrow and Tao (1983) used the naphthalene sublimation technique to study the flow in flat rectangular channels of large aspect ratios with obstacles situated on one of the walls of the channel and oriented transversely to the flow direction. The results showed a substantial enhancement of Sherwood numbers (Sh) compared with results for a smooth-wall duct. Drain and Martin (1985) performed laser Doppler velocimetry (LDV) measurements on the fully developed water flow in a rectangular duct with one surface roughened with a periodic array of elements. They found that the $k-\varepsilon$ turbulence model tended to seriously underestimate the reattachment length, which is

an important indicator of turbulence structure. The interaction of the Coriolis force with the mean shear causes stabilization and destabilization near the two walls. The concept of stability (instability) is related to a decrease (increase) of the turbulence level with respect to the non-rotating case. Meng and Pletcher (2000a) studied rotating channel flows with and without heat transfer using large eddy simulation and found that the Coriolis forces enhanced turbulence production and increased the intensity of turbulence on the unstable side (trailing or pressure side), while the Coriolis forces reduced the production and the intensity of turbulence on the stable side (leading or suction side). The effects of rotation on secondary flow and the stability have been documented by Taslim et al. (1991). According to Wagner et al. (1992), approximately 75 per cent of the estimated uncertainty in calculating the heat transfer coefficient was due to the temperature measurement error. Furthermore, it can be very difficult and expensive to obtain detailed information about the flow distribution in a ribbed passage experimentally. Large eddy simulation presents an attractive alternative to experiments for studying details of such flows. The goal of this study was to perform a large eddy simulation of rotating/non-rotating turbulent flow in a plane channel with transverse square ribs on both walls. The ribs were directly opposed and aligned normal to the main flow direction. The ratio of rib spacing to rib height was 16 and rib height to channel height was 0.125. Such a configuration is shown in Fig. 5.1. The axis of system rotation was parallel to the z direction. Periodic and step periodic boundary conditions were used at the inflow and outflow boundaries as fully developed channel flows were assumed. This assumption allows the computed domain to be limited to the region between two adjacent ribs so that a reasonable computational grid can be used.

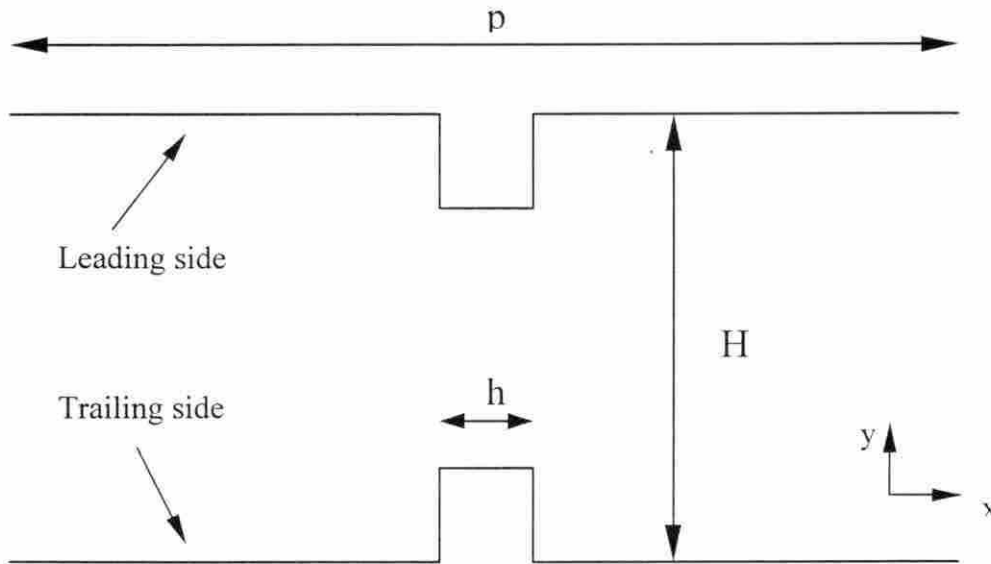


Figure 5.1 Schematic of the computational domain for the ribbed channel

5.2 Simulation Details

The governing equations are the same as those used for incompressible rotating duct flow since the energy equation was naturally included in the simulation. However, because of the heat addition, the thermal boundary conditions at the inlet and outlet are no longer periodic. With different types of heating, thermal boundary conditions at the inlet and outlet are different. For this study, a constant nondimensional heat flux q_w was applied, which is defined as

$$q_w = \frac{q_w^*}{C_p U_r \rho_r T_r}, \quad (5.1)$$

in which the subscript r denotes reference quantity. So the temperature was decomposed into a periodic component and an aperiodic component, as has been done for pressure.

$$\tilde{T}(x, y, z, t) = \phi x + \tilde{T}_p(x, y, z, t). \quad (5.2)$$

In the equation above, the subscript p denotes a periodic component, which satisfies

$$\tilde{T}_p(0, y, z, t) = \tilde{T}_p(L_x, y, z, t), \quad (5.3)$$

and ϕ is the streamwise temperature gradient, which is defined as

$$\phi = \frac{q_w}{(\dot{m}/A_c)} \frac{2}{L_y}, \quad (5.4)$$

where 2 means that heating is applied on both upper and lower walls of the channel at the same magnitude. Since in the nondimensionalization method used in this work, channel height, L_y , is defined as 2, Eq. 5.4 can be modified to

$$\phi = \frac{q_w}{(\dot{m}/A_c)}, \quad (5.5)$$

and the average temperature difference between inlet and outlet is

$$\Delta\tilde{T}_x = \phi L_x = \frac{q_w L_x}{(\dot{m}/A_c)}. \quad (5.6)$$

Thus the step periodic boundary condition for temperature becomes

$$\begin{aligned} \tilde{T}(0, y, z, t) &= \tilde{T}(L_x, y, z, t) - \Delta\tilde{T}_x \\ \tilde{T}(L_x, y, z, t) &= \tilde{T}(0, y, z, t) + \Delta\tilde{T}_x \end{aligned} \quad (5.7)$$

The Reynolds number is based on the half channel height and bulk properties. As heat is added into the flow, the definitions of the bulk properties are as below

$$\rho_b = \frac{1}{L_y} \int_{-1}^1 \rho dy, \quad (5.8)$$

$$u_b = \frac{1}{\rho_b L_y} \int_{-1}^1 \rho u dy, \quad (5.9)$$

$$T_b = \frac{1}{\rho_b u_b L_y} \int_{-1}^1 \rho u T dy. \quad (5.10)$$

An incompressible case without heat transfer was simulated for $Re_b = 5,600$, which

is 22,400 based on hydraulic diameter. Utilizing the results from this case, heating was applied, as well as rotation.

The data collection method in this case was different from that in duct flow cases because channel flow with transverse ribs and rotation is homogeneous in the spanwise direction, instead of the streamwise direction. So, at each time step, the data were averaged in the spanwise direction. The final ensemble averaged data were obtained through further averaging in time based on the spanwise averaged data. For example,

$$\bar{u}_i(x, y) = \langle \tilde{u}_i(x, y, z, t) \rangle_{z,t}, \quad (5.11)$$

where $\langle \rangle_{z,t}$ denotes ensemble averaging in both the z direction and time. Turbulent statistics were calculated based on the mean value and the method was the same as shown for duct flow cases, except that the turbulent intensities were also averaged in the spanwise direction instead of the streamwise direction.

This work started with the non-rotating case without heat transfer to briefly study the effects of ribs on the flow field. This case was started using a uniform velocity field. Due to the existence of ribs in the flow, random background fluctuations are not necessary. In around two to three thousand time steps, turbulence takes place and is formed in the flow, which is much faster than for duct flow cases. This was due to the turbulence promotion effects of ribs. It took another ten thousand time steps to collect the mean flow structure data and turbulence statistics. Based on the incompressible non-rotating data, heat was added into the flow to study the effects of ribs on the heat transfer. This also takes around ten thousand time steps. Finally, rotation was applied to study the effects of rotation on heat transfer and another ten thousand time steps were consumed for the flow field to become statistically steady and data collected. The summary of parameters for all these three cases is given in Table 5.1.

Table 5.1 Case summary for ribbed channel simulation

Case	Nondimensional Domain	Grid	Re_b	q_w	Ro
I	$4 \times 2 \times 5$	$60 \times 72 \times 72$	5,600	0	0
II	$4 \times 2 \times 5$	$60 \times 72 \times 72$	5,600	2×10^{-3}	0
III	$4 \times 2 \times 5$	$60 \times 72 \times 72$	5,600	2×10^{-3}	0.3

5.3 Results and Discussion

5.3.1 Effects of Ribs on Flow Field

Ribs were added into the domain to act as turbulence promoters. It is expected that ribs can enhance the turbulence level in the flow field and this has been observed in the simulations. Moreover, it will change the mean flow field as shown in Figure 5.1, which is a plot of the streamlines in the $x-y$ plane.

Very good symmetry is observed in the plot about the middle plane of the channel. It can be found from the figure that ribs accelerate the fluid going through it since mass should be conserved at all cross-sections. Since the ribs form a sudden expansion, a large recirculation zone can be found after each rib. The reattachment length for the recirculation zone is about five times the height. Furthermore, since the transverse ribs block the streamwise main flow, a small recirculation zone is also found between the front face of each rib and the wall. By creating these recirculation zones, ribs change the mean flow structure compared with plane channel flow (Dailey, 1997). The existence of recirculation zones greatly increases the energy

consumption to drive the flow through the channel. The pressure gradient along the streamwise direction for this case is an order of magnitude larger than in a plane channel case. So to enhance the turbulence in the flow, a price has to be paid on driving the flow. Moreover, these regions also have different characteristics for heat transfer than that in a plane channel, which will be shown in the next section.

In addition to the mean flow field, the distributions of turbulence statistics are also altered by the existence of two ribs. Figure 5.3 depicts the contours of turbulent kinetic energy in the channel, which is defined by $TKE = 1/2(u'_{rms}^2 + v'_{rms}^2 + w'_{rms}^2)$. Obviously, turbulent kinetic energy is much higher near the ribs, induced by the high turbulence production capability of the ribs. So the addition of the ribs produced two peak regions of turbulence level near the ribs. However, two regions of low turbulence level are also produced in the recirculation zones at the rear side of the ribs. Their effects on the transport of heat will be studied in the next section.

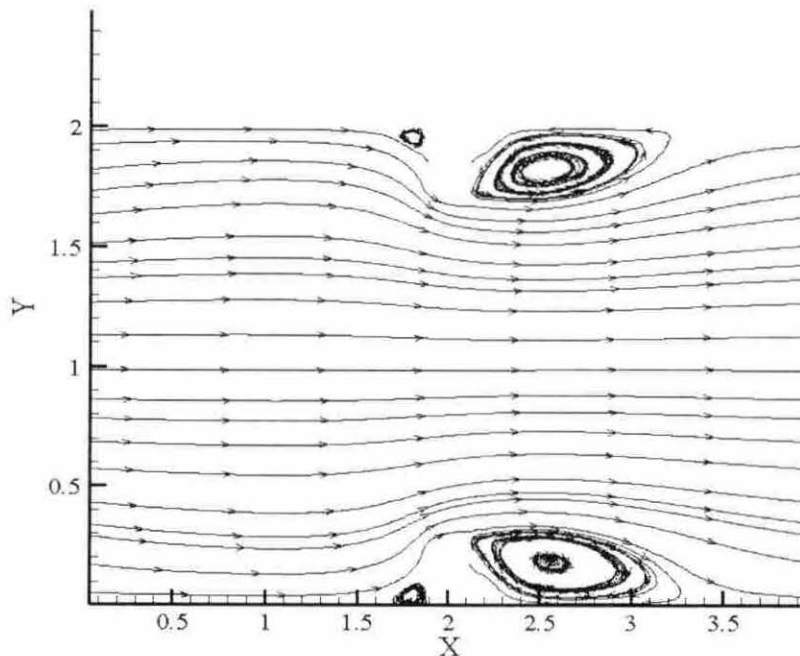


Figure 5.2 Streamlines in the incompressible non-rotating ribbed channel

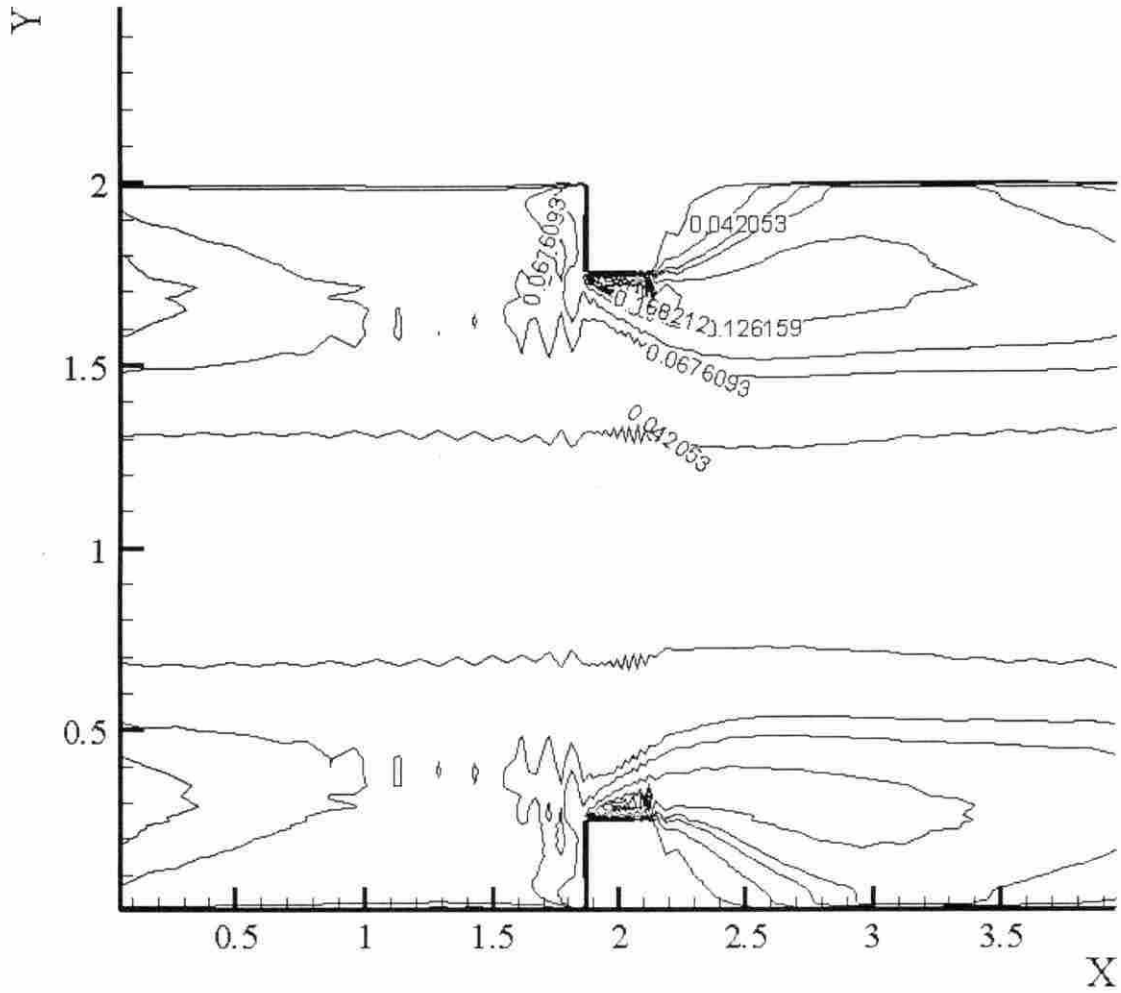


Figure 5.3 Contours of turbulent kinetic energy in a rotating incompressible ribbed channel flow

5.3.2 Heat Transfer in a Ribbed Channel Without Rotation

The original purpose of adding ribs into the channel is to enhance the turbulence level in the flow; thus, the heat transfer can be enhanced. For this reason, it is of interest to know the extent to which heat transfer is increased.

The nondimensional parameter characterizing heat transfer is the Nusselt number, Nu , which is formulated as

$$Nu = (hD)/k. \quad (5.12)$$

In Eq. 5.12, h is heat transfer coefficient, which is given by $h = q_w / (T_w - T_b)$, where T_b is the bulk temperature as given in Eq. 5.10, and k is the thermal conductivity of the fluid evaluated at bulk conditions of the flow. So Nu represents the relative magnitude of convection heat transfer in terms of conduction heat transfer.

Dailey (1997) found that for turbulent flow in a plane channel with $Re_D = 11,200$, the average Nusselt number was 34.2. And the McAdams correlation (Rohsenow and Choi, 1961) for a circular tube

$$Nu = 0.023 Re_D^{0.8} Pr^{0.4} \quad (5.13)$$

yields 34.6, which is very close to the result obtained by Dailey. So it is safe to use the correlation for circular tube as an approximation for the plane channel. In this study, the Reynolds number based on hydraulic diameter is 22,400. So for a plane channel with this Reynolds number, the average Nusselt number is 60.3. On the other hand, the averaged Nusselt number for a ribbed channel at $Re_D = 22,400$ is 93.4, which is about 55% greater than for the smooth wall case. In summary, the addition of ribs greatly enhanced the effectiveness of heat transfer.

However, not only the global heat transfer coefficient is of interest here. It is also important to know that detailed heat transfer coefficient distribution along the channel and the wall temperature distribution. To understand the effects of ribs better, the distribution of Nusselt number on the front side, top and rear side is also included.

Due to the symmetry of the flow about the middle plane, the distributions on the upper and lower walls were averaged. The entire distribution is shown in Figure 5.4.

As can be seen from the plot, Nu is larger than 60 for most of the channel, which means ribs enhance the heat transfer for most of the channel. The peak value of Nu is 146.2, which occurs on the front corner of rib, where the peak of turbulent kinetic energy takes place. This is consistent with the concept that turbulence accounts for a large part of the transport process. However, in the recirculation regions, where turbulent intensities are low, heat transfer is greatly reduced. At the rear corner between the rib and the wall, Nu drops to as low as 11.3, less than one fifth of the plane channel value. As a consequence of the thermal boundary condition and uneven distribution of heat transfer coefficient, the temperature varies significantly along the channel as shown in Figure 5.5, with the peak occurring at the corner with the lowest Nu and the minimum occurring at the front corner of the rib, where the Nu is the largest. Low wall temperature, or high Nusselt number, shows that the cooling effect has been achieved at this certain location. On the other hand, high wall temperature, or low Nusselt number, means that cooling is insufficient at this location and the material here is experiencing high thermal stress, which may leads to early local fatigue of the material. This needs some special treatment of the material, or the configuration of the ribs needs to be altered and optimized.

Also, the ribs have the same effects on the velocity field and turbulence statistics as in the incompressible ribbed channel case – producing major recirculation zones on the rear side and minor recirculation zones on the front side of the ribs and generating a high turbulence level on the top of the ribs. The addition of heat transfer does not alter the pattern of flow structure, although turbulence level is decreased because of the heating.

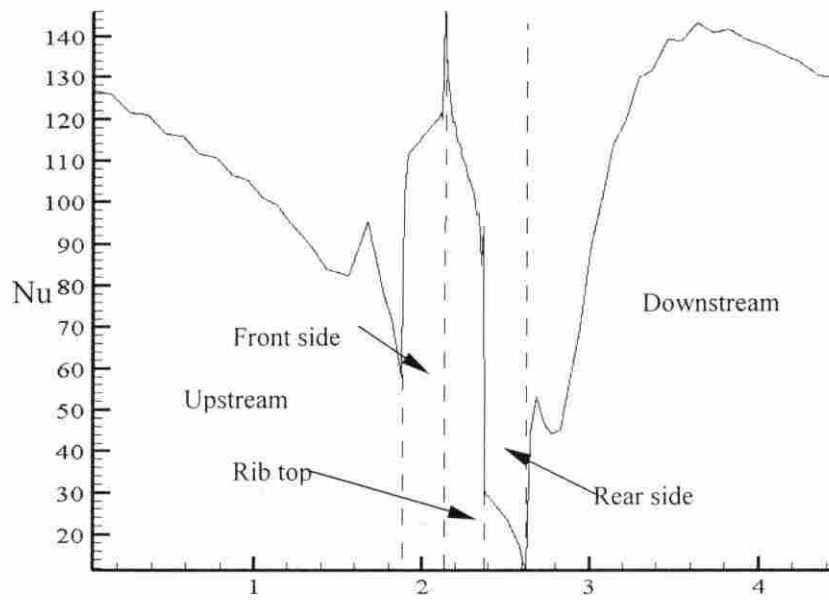


Figure 5.4 Nusselt number distribution along the channel

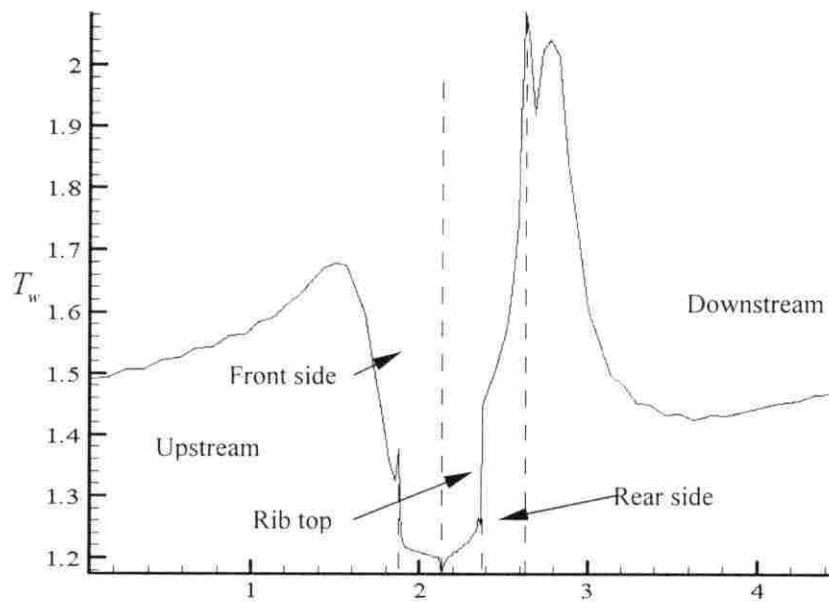


Figure 5.5 Wall temperature distribution along the channel

5.3.3 Heat Transfer in Ribbed Channel With Rotation

As in the rotating duct case, system rotation in a ribbed channel will alter the flow structure. The Coriolis force will enhance the turbulence production and increase the turbulence level on the trailing side, while suppressing the turbulence production and decreasing the turbulence level on the leading side. Furthermore, the mean velocity field will be shifted to the trailing side. Fig. 5.6 shows the vector plot of velocity in the $x-y$ plane. The lower wall here is the trailing side. From the plot, it can be seen that velocity is apparently higher near the trailing side than on the leading side. Since the Coriolis force drives high momentum fluid from the core region to the trailing side and the high speed fluid will interact with the fluid in the recirculation zone near the rear of the rib, the increased mixing will cause the recirculation zone to become smaller compared with that on leading side, as shown in the streamline plot in Fig. 5.7. The reattachment length on the trailing side is four times the rib height, while it is around seven times the rib height on the leading side. Also, the turbulent kinetic energy distribution shows that the trailing side has more and larger high energy regions, as seen in Fig. 5.8. The turbulent kinetic energy level is small compared with incompressible case since heating suppresses the turbulent production in the whole flow.

Due to the rotational effects on the flow field and the turbulent statistics, the temperature field is influenced in a similar way. The heat transfer coefficient is higher on the trailing side than on leading side, while temperature is higher on the leading side than trailing side, as shown in Fig. 5.9 and Fig. 5.10. Since heat transfer in a rotating ribbed channel is much alike the real situation in the internal cooling passages in a rotating turbine blade, this means the leading side needs more cooling than the trailing side, or fatigue will occur on leading side faster than on trailing side.

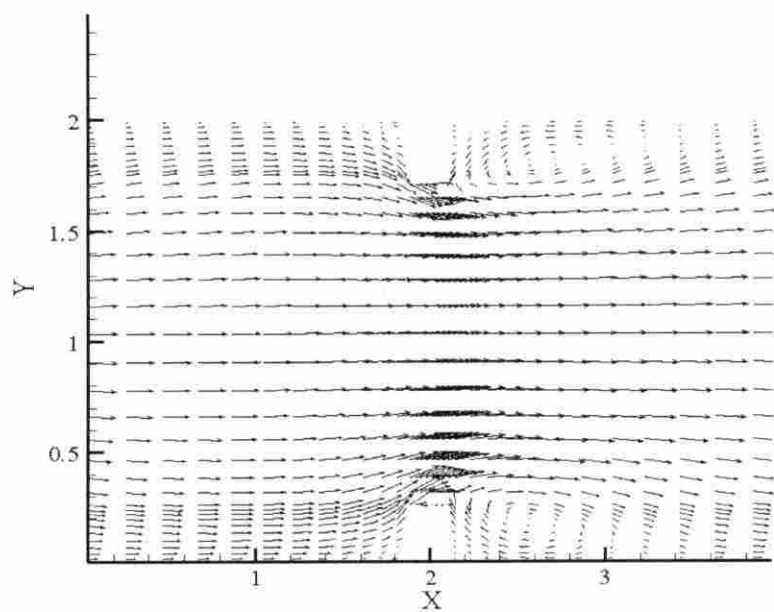


Figure 5.6 Velocity field in rotating compressible ribbed channel

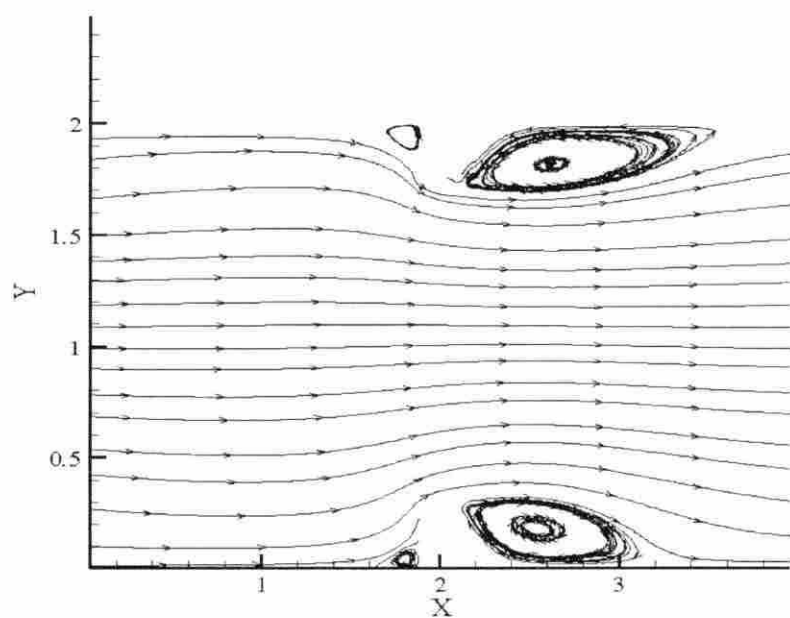


Figure 5.7 Streamlines in rotating compressible ribbed channel

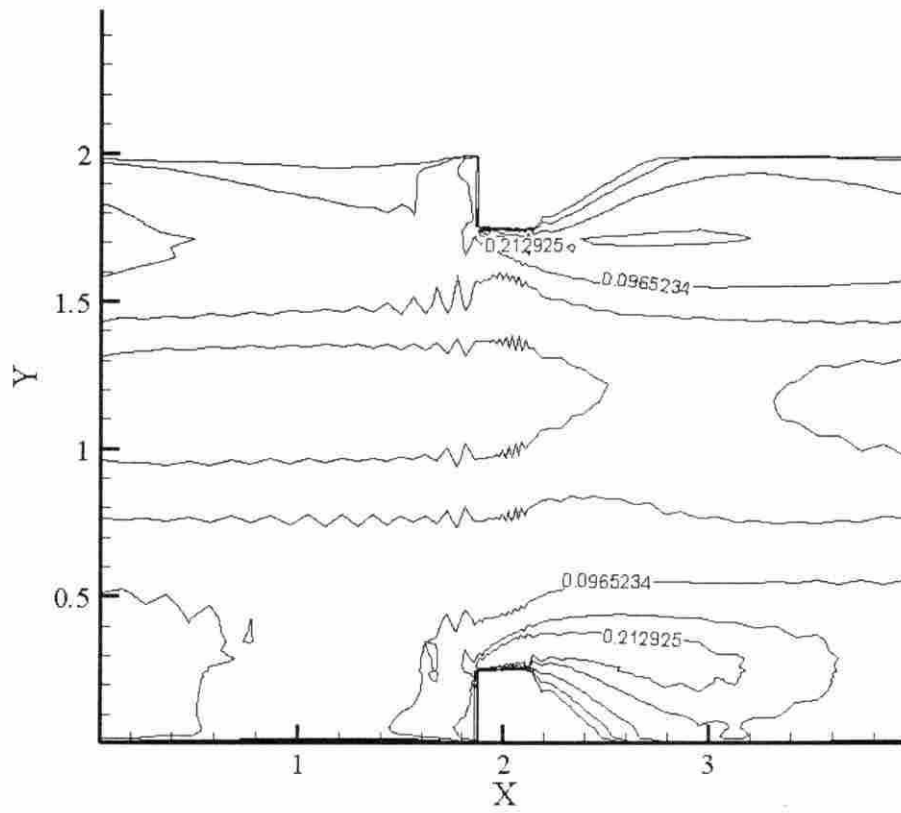


Figure 5.8 Turbulent kinetic energy in compressible rotating ribbed channel

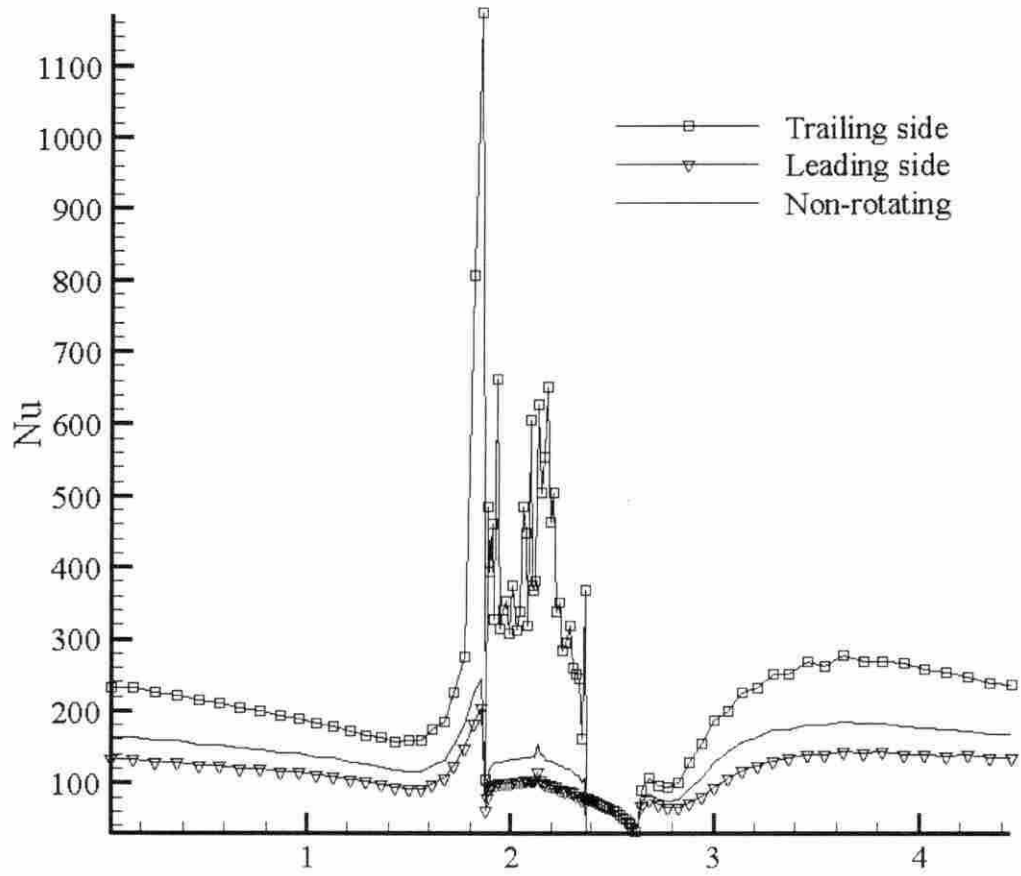


Figure 5.9 Distribution of Nu along the ribbed channel with heat transfer and system rotation

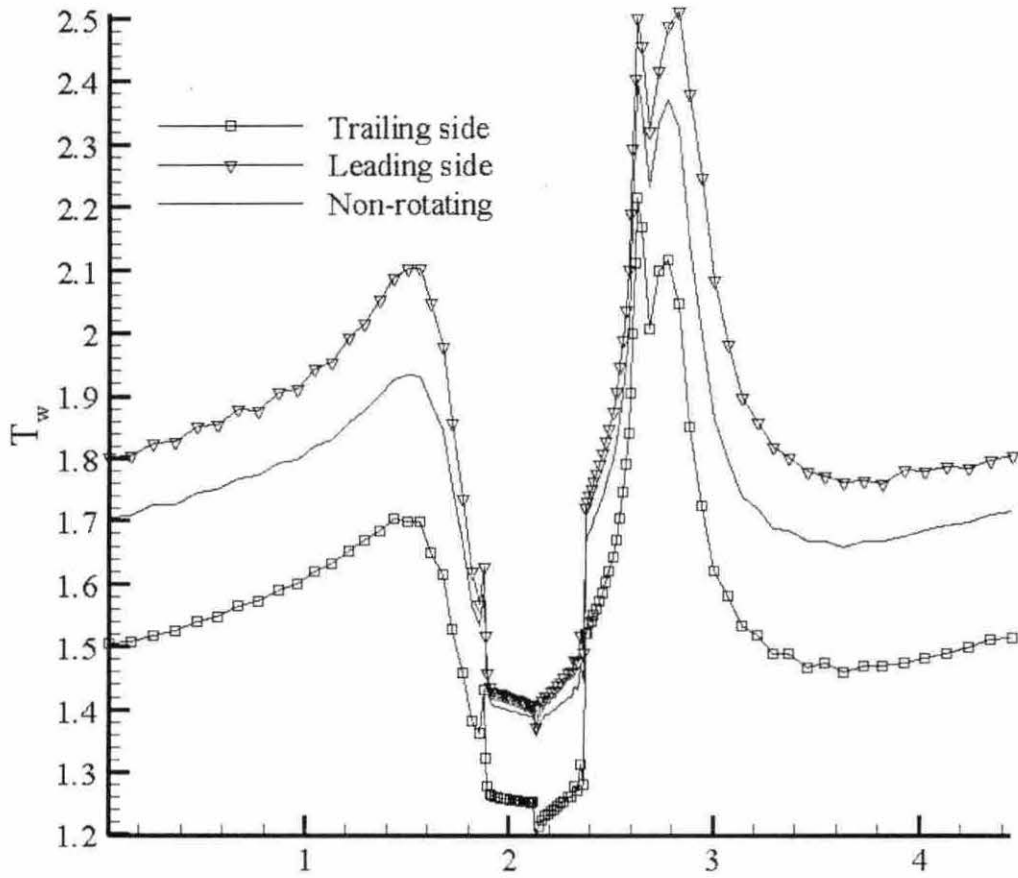


Figure 5.10 Distribution of wall temperature along the ribbed channel with heat transfer and system rotation

5.4 Conclusions

In this chapter, results were presented to study the influence of ribs and system rotation on heat transfer in the channel using large eddy simulation, which captures many interesting features in the flow. Firstly, it was found that ribs will change the flow structure by creating recirculating zones on both front and rear sides of the rib, with the one on the rear side much larger and stronger. As well as changing the mean flow field, ribs will create turbulent active regions on the top of the ribs, while the recirculation zones will see a very low turbulence level. Consequently, this will affect the temperature field in the flow and heat transfer effects. As a whole, the average Nusselt number is more than 50 per cent higher than its plane channel counterpart. An explanation for this phenomenon is that ribs create normal velocities in the channel, which greatly aid the transport of thermal energy by convection. However, in the recirculating zones, Nusselt number may drop to as low as less than $1/5$ of the plane channel value. So, although ribs enhance the overall heat transfer effect, they also create very thermally passive regions where some special attention is needed. Optimization between the overall and local heat transfer effectiveness has to be achieved for the ribs to become more effective as a cooling promoter. Finally, system rotation is applied to the flow and this creates some phenomena similar to those in rotating duct flow. It increases the turbulence level and enhances the heat transfer on the trailing side. Also, it decreases the turbulence level and suppresses heat transfer on the leading side. In summary, to achieve better cooling effects, a balance between the trailing side and leading side and optimization between overall and local heat transfer effectiveness have to be sought. Large eddy simulation, as has been proved, will continue to be very powerful in providing insight into the fluid flow and heat transfer in the cooling passage and enable designers to achieve more effective configurations for the next generation of cooling devices.

CHAPTER 6. CONCLUSIONS

6.1 Summary

A compressible finite volume formulation was used for the large eddy simulation of wall-bounded turbulent flows with heat transfer. The foundation code written by Dailey (1997) is an efficient, low-memory scheme that allows simulation of complex flows. The code was written in a multiblock framework so that it could be applied to complex geometries and efficiently parallelized. The code was further expanded by Meng (2000). More advanced MPI (message passing interface) replaced PVM (parallel virtual machine) for communication between blocks and the dynamic Smagorinsky model was implemented into the model, which greatly increased the flexibility and applicability of the code.

In this thesis work, the dynamic Smagorinsky model was further localized to study inhomogeneous turbulent flows. As well as the subgrid stress model, the dynamic turbulent Prandtl number model was also localized, which gives the code more flexibility and enables more choices for future researchers.

This localized dynamic Smagorinsky model was applied to the incompressible turbulent flow in a duct with a square cross-section. Both mean flow field and turbulent statistics were compared with DNS results. Due to the inhomogeneity of the flow, the filtering process also needed further expansion to gather information from all three dimensions. The effects of this special geometry on the generation of secondary flow and its influence on the characteristics of the flow were studied.

Based on the incompressible duct flow, system rotation was applied on the flow. The interaction between turbulence and rotation was investigated. Rotation also

interacts with the secondary flow field and generates new secondary flow in the cross-section and this was examined carefully.

Furthermore, to study the effects of rotation on heat transfer in a similar setting as in the internal cooling passages of a turbine blade, large eddy simulation was applied to the heat transfer in a ribbed channel with system rotation. The influence of the transverse ribs on the flow field and heat transfer was studied and compared to the plane channel results. Then the study was focused on the influence of system rotation on heat transfer.

In summary, large eddy simulation captured many interesting and fine features of the flows and enabled detailed analysis into the phenomena, while consuming far fewer resources than direct numerical simulation. In incompressible duct flow, results of both the mean flow field and turbulence statistics were predicted to be in excellent agreement with the DNS results. The secondary flow, which is composed of four pairs of counter rotating cells, was also predicted very well. All these show that the dynamic Smagorinsky model combined with a simple localization method can be successfully applied to complex turbulent flows. System rotation was found to suppress turbulence activities on the leading side and enhance the turbulence level on the trailing side. Different from rotation applied to a channel, system rotation in the duct creates the well known Taylor- Görtler vortices and Taylor-Proudman regime in the cross-section, overwhelming the former existing secondary flow for the non-rotating case. For the rotating rib-roughened channel flow, a large recirculation zone on the rear side of the rib and smaller recirculation zone on the front side were reproduced. And ribs greatly enhanced heat transfer compared with plane channel case. When system rotation was applied, the heat transfer on the trailing side was enhanced while heat transfer on leading side was suppressed. All these again confirm that large eddy simulation using the dynamic Smagorinsky model combined with a simple localization method can produce very accurate results in complex and inhomogeneous turbulent flows. According to the author's knowledge, this has never

been studied and recognized before. And this is the major contribution of this thesis work.

6.2 Recommendations for Future Work

Other than the Smagorinsky model, the mixed model can also be dynamically formulated and localized. It is believed by the author that the mixed model has deeper physical meaning than the Smagorinsky model and should be able to produce even better results. To the author's regret, the mixed model was not successfully implemented into the code, which suggests that the filtering method utilized now is not compatible with the requirements of the mixed model. Expanding our current filtering technique and enabling the mixed model will prove to be valuable. Meanwhile, further localization methods may prove necessary as the complexity of problems increases.

This work only simulated turbulent flow through a square duct. Although it provides a lot of insights, further study on duct flow with rectangular cross-section is an interesting work to pursue. Under different aspect ratios of the cross section, the corners and the walls will have different level of influence on the turbulent flow, which is worth further investigation.

Heat transfer in a duct, together with system rotation, is a very good representation of the cooling passage in a turbine blade. Studying about this topic will enable much better understanding of the physics of turbulent flow and heat transfer under this situation and provide an invaluable guide for the design of the next generation gas turbine machine, for which effective cooling is highly demanded. For this problem, centrifugal buoyancy generated by the heating and rotation must be taken into account. Furthermore, ribs or other turbulence promoters can be added into the duct to study their effects on turbulence and heat transfer.

APPENDIX A JACOBIAN MATRICES

The Jacobian matrices for the Favre filtered system of governing equations are given below.

$$[T] = \begin{bmatrix} 1/\tilde{T} & 0 & 0 & 0 & -\bar{p}/\tilde{T}^2 \\ \tilde{u}/\tilde{T} & \bar{p}/\tilde{T} & 0 & 0 & -\bar{p}\tilde{u}/\tilde{T}^2 \\ \tilde{v}/\tilde{T} & 0 & \bar{p}/\tilde{T} & 0 & -\bar{p}\tilde{v}/\tilde{T}^2 \\ \tilde{w}/\tilde{T} & 0 & 0 & \bar{p}/\tilde{T} & -\bar{p}\tilde{w}/\tilde{T}^2 \\ c_v + \frac{1}{2}(\tilde{u}^2 + \tilde{v}^2 + \tilde{w}^2)/\tilde{T} & \bar{p}\tilde{u}/\tilde{T} & \bar{p}\tilde{v}/\tilde{T} & \bar{p}\tilde{w}/\tilde{T} & -\frac{1}{2}(\bar{p}/\tilde{T}^2)(\tilde{u}^2 + \tilde{v}^2 + \tilde{w}^2) \end{bmatrix} \quad (\text{A.1})$$

$$[\Gamma] = \begin{bmatrix} R/\tilde{T} & 0 & 0 & 0 & -\bar{p}/\tilde{T}^2 \\ R\tilde{u}/\tilde{T} & \bar{p}/\tilde{T} & 0 & 0 & -\bar{p}\tilde{u}/\tilde{T}^2 \\ R\tilde{v}/\tilde{T} & 0 & \bar{p}/\tilde{T} & 0 & -\bar{p}\tilde{v}/\tilde{T}^2 \\ R\tilde{w}/\tilde{T} & 0 & 0 & \bar{p}/\tilde{T} & -\bar{p}\tilde{w}/\tilde{T}^2 \\ R\left[c_v + \frac{1}{2}(\tilde{u}^2 + \tilde{v}^2 + \tilde{w}^2)/\tilde{T}\right] & \bar{p}\tilde{u}/\tilde{T} & \bar{p}\tilde{v}/\tilde{T} & \bar{p}\tilde{w}/\tilde{T} & -\frac{1}{2}(\bar{p}/\tilde{T}^2)(\tilde{u}^2 + \tilde{v}^2 + \tilde{w}^2) \end{bmatrix} \quad (\text{A.2})$$

$$[A] = \begin{bmatrix} \bar{u}/\tilde{T} & \bar{p}/\tilde{T} & 0 & 0 & -\bar{p}\bar{u}/\tilde{T}^2 \\ \bar{u}^2/\tilde{T} + R & 2\bar{p}\bar{u}/\tilde{T} & 0 & 0 & -\bar{p}\bar{u}^2/\tilde{T}^2 \\ \bar{u}\bar{v}/\tilde{T} & \bar{p}\bar{v}/\tilde{T} & \bar{p}\bar{u}/\tilde{T} & 0 & -\bar{p}\bar{u}\bar{v}/\tilde{T}^2 \\ \bar{u}\bar{w}/\tilde{T} & \bar{p}\bar{w}/\tilde{T} & 0 & \bar{p}\bar{u}/\tilde{T} & -\bar{p}\bar{u}\bar{w}/\tilde{T}^2 \\ \bar{u}\hat{H}/\tilde{T} & \bar{p}/\tilde{T}(\hat{H} + \bar{u}^2) & \bar{p}\bar{u}\bar{v}/\tilde{T} & \bar{p}\bar{u}\bar{w}/\tilde{T} & -\frac{1}{2}(\bar{p}\bar{u}/\tilde{T}^2)(\bar{u}^2 + \bar{v}^2 + \bar{w}^2) \end{bmatrix} \quad (\text{A.3})$$

$$[B] = \begin{bmatrix} \bar{v}/\tilde{T} & 0 & \bar{p}/\tilde{T} & 0 & -\bar{p}\bar{v}/\tilde{T}^2 \\ \bar{v}\bar{u}/\tilde{T} & \bar{p}\bar{v}/\tilde{T} & \bar{p}\bar{u}/\tilde{T} & 0 & -\bar{p}\bar{u}\bar{v}/\tilde{T}^2 \\ \bar{v}^2/\tilde{T} + R & 0 & 2\bar{p}\bar{v}/\tilde{T} & 0 & -\bar{p}\bar{v}^2/\tilde{T}^2 \\ \bar{v}\bar{w}/\tilde{T} & 0 & \bar{p}\bar{w}/\tilde{T} & \bar{p}\bar{v}/\tilde{T} & -\bar{p}\bar{v}\bar{w}/\tilde{T}^2 \\ \bar{v}\hat{H}/\tilde{T} & \bar{p}\bar{u}\bar{v}/\tilde{T} & (\bar{p}/\tilde{T})(\hat{H} + \bar{v}^2) & \bar{p}\bar{v}\bar{w}/\tilde{T} & -\frac{1}{2}(\bar{p}\bar{v}/\tilde{T}^2)(\bar{u}^2 + \bar{v}^2 + \bar{w}^2) \end{bmatrix} \quad (\text{A.4})$$

$$[C] = \begin{bmatrix} \bar{w}/\tilde{T} & 0 & 0 & \bar{p}/\tilde{T} & -\bar{p}\bar{w}/\tilde{T}^2 \\ \bar{w}\bar{u}/\tilde{T} & \bar{p}\bar{w}/\tilde{T} & 0 & \bar{p}\bar{u}/\tilde{T} & -\bar{p}\bar{u}\bar{w}/\tilde{T}^2 \\ \bar{w}\bar{v}/\tilde{T} & 0 & \bar{p}\bar{w}/\tilde{T} & \bar{p}\bar{v}/\tilde{T} & -\bar{p}\bar{v}\bar{w}/\tilde{T}^2 \\ \bar{w}^2/\tilde{T} + R & 0 & 0 & 2\bar{p}\bar{w}/\tilde{T} & -\bar{p}\bar{w}^2/\tilde{T}^2 \\ \bar{w}\hat{H}/\tilde{T} & \bar{p}\bar{u}\bar{w}/\tilde{T} & \bar{p}\bar{v}\bar{w}/\tilde{T} & (\bar{p}/\tilde{T})(\hat{H} + \bar{w}^2) & -\frac{1}{2}(\bar{p}\bar{w}/\tilde{T}^2)(\bar{u}^2 + \bar{v}^2 + \bar{w}^2) \end{bmatrix} \quad (\text{A.5})$$

where

$$\hat{H} = c_p \tilde{T} + \frac{1}{2}(\bar{u}^2 + \bar{v}^2 + \bar{w}^2). \quad (\text{A.6})$$

APPENDIX B DISCRETE TEST FILTERS

In this appendix, the discrete form of the top hat filtering operation is derived. The filtering operation is defined by a convolution integral as

$$\tilde{f}(x, t) = \int_D \widehat{G}(\bar{x}, \bar{\xi}) f(\bar{\xi}, t) d\bar{\xi}, \quad (\text{B.1})$$

where \widehat{G} is the test filter function and the integration is performed over the entire domain. The top hat filter function is

$$\widehat{G}(x - \xi) = \begin{cases} \frac{1}{\Delta_r^3} & x_i - \Delta_r/2 \leq \xi_i \leq x_i + \Delta_r/2 \\ 0 & \text{otherwise} \end{cases}, \quad (\text{B.2})$$

where Δ_r is the test filter width.

For a one-dimensional grid with uniform spacing Δ , Eq. D.2 can be simplified by using numerical integration in the space. With $\Delta_r = 2\Delta$, which is the most common choice of test filter width, the trapezoidal rule applied to grid points $i-1$, i and $i+1$ yields

$$\tilde{f}_i = \frac{1}{\Delta_r} \int_{x-\Delta_r/2}^{x+\Delta_r/2} f(\xi) d\xi = \frac{1}{4} f_{i-1} + \frac{1}{2} f_i + \frac{1}{4} f_{i+1}. \quad (\text{B.3})$$

Similarly Simpson's rule gives

$$\tilde{f}_i = \frac{1}{\Delta_r} \int_{x-\Delta_r/2}^{x+\Delta_r/2} f(\xi) d\xi = \frac{1}{6} f_{i-1} + \frac{2}{3} f_i + \frac{1}{6} f_{i+1}. \quad (\text{B.4})$$

In general, the filter operation for these three uniform grid points can be expressed as

$$\tilde{f}_i = a_1 f_{i-1} + a_0 f_i + a_1 f_{i+1}. \quad (\text{B.5})$$

Using the test filtering operation in one direction as above, filtering operation in all three dimensions can be obtained by applying the one-dimensional filtering

operation successively in each coordinate direction. And this process can be summarized in three steps. In the first step, the 1- D filter in the x or i direction is applied to all points in the field. In the second step, the 1- D filter in the y or j direction is applied to all points. Finally the 1- D filter in the z or k direction is applied to all points. The equivalent operation can be performed by a single pass with formula given by

$$\begin{aligned} \bar{f}_{i,j,k} = & c_0 f_{i,j,k} + c_1 [f_{i\pm 1,j,k} + f_{i,j\pm 1,k} + f_{i,j,k\pm 1}] + \\ & c_2 [f_{i\pm 1,j\pm 1,k} + f_{i\pm 1,j,k\pm 1} + f_{i,j\pm 1,k\pm 1}] + c_3 [f_{i\pm 1,j\pm 1,k\pm 1}] \end{aligned} \quad (\text{B.6})$$

where

$$c_0 = a_0^3 ; \quad c_1 = a_0^2 a_1 ; \quad c_2 = a_0 a_1^2 ; \quad c_3 = a_1^3 . \quad (\text{B.7})$$

Consequently, for the trapezoidal filter, the coefficients are

$$c_0 = \frac{8}{64} ; \quad c_1 = \frac{4}{64} ; \quad c_2 = \frac{2}{64} ; \quad c_3 = \frac{1}{64} , \quad (\text{B.8})$$

and for Simpson filter, the coefficients are

$$c_0 = \frac{64}{216} ; \quad c_1 = \frac{16}{216} ; \quad c_2 = \frac{4}{216} ; \quad c_3 = \frac{1}{216} . \quad (\text{B.9})$$

Since Simpson filter is exact for second order polynomials, while the trapezoidal filter is exact only for linear functions, the Simpson filter is mainly used in this work to perform the test filter operation.

In addition to the 27-point test filter, a 7-point test filter is also used in this work. Using the trapezoidal filter, the coefficients for 7-point test filter are

$$c_0 = \frac{1}{2} ; \quad c_1 = \frac{1}{12} ; \quad c_2 = 0 ; \quad c_3 = 0 . \quad (\text{B.10})$$

It is worth noting that the above test filter coefficients are for uniform grids. In this work, to capture to turbulent structures near the wall, grids are stretched toward the wall, which makes the using of these coefficients inaccurate, although the quantities to be filtered have taken into the account the non-uniformity of the grid. Trapezoidal and Simpson integration can be generalized to account for the unequal

spacing in grids. However, that will significantly increase the requirement for computation and data storage. Moreover, on each pair of neighboring control volumes, the sizes are very close to each other due to the mesh generation method used in this work. So the error involved is considered to be small enough to be neglected and these coefficients are used directly throughout the domain without considering the differences between grid sizes.

BIBLIOGRAPHY

- Akselvoll, K. and Moin, P., 1993, Engineering Applications of Large Eddy Simulations, (S.A. Ragab and U. Piomelli, eds), Vol. 162, pp. 1-5, FED, ASME, New York.
- Akselvoll, K. and Moin, P., 1995, "Large Eddy Simulation of Turbulent Confined Coannular Jets and Turbulent Flow Over a Backward Facing Step," Report No. TF-63, Department of Mechanical Engineering, Stanford University.
- Amon, C., 1992, "Spectral Element Fourier Method for Transitional Flows in Complex Geometries," AIAA Journal, Vol. 31, pp. 42-48.
- Aupoix, B., 1986, Direct and Large Eddy Simulation of Turbulence, Vol. 15, pp. 37-66, (U. Schumann and R. Friedrich, eds), Notes on Numerical Fluid Mechanics, Vieweg-Verlag, Branschweig.
- Avancha, R., 2001, "A Study of the Heat Transfer and Fluid Mechanics of the Turbulent Separating and Reattaching Flow Past a Backward Facing Step Using Large Eddy Simulation", Doctoral Dissertation, Department of Mechanical Engineering, Iowa State University.
- Balaras, E. and Benocci, C., 1994, Application of Direct and Large Eddy Simulation to Transition and Turbulence, AGARD-CP-551, AGARD, Neilly-sur-Seine.
- Bardina, J., Ferziger, J.H., and Reynolds, W.C., 1984, "Improved Turbulence Models based on LES of Homogeneous Incompressible Turbulent Flows," Report No. TF-19, Department of Mechanical Engineering, Stanford University.
- Bardina, J., Ferziger, J., and Rogallo, R., 1985, "Effect of Rotation on Isotropic Turbulence; Computation and Modeling," Journal of Fluid Mechanics, Vol. 154, pp. 321-336.
- Baron, F. and Laurence, D., 1983, "Large Eddy Simulation of a Wall-bounded Turbulent Jet Flow and Homogeneous Shear Flow," Proc. 4th Symposium on Turbulent Shear Flows. Karlsruhe, Germany, 12-14 September, 1983.

- Benocci, C. and Pinelli, A., 1990, "The Role of the Forcing Term in the Large Eddy Simulation of Equilibrium Channel Flow," *Engineering Turbulence Modeling and Experiments*, (W. Rodi and E.N. Ganic, eds), Elsevier Science Ltd., New York, pp. 287-296
- Bergeles, G. and Athanassiadis, N., 1983, "The Flow Past a Surface-Mounted Obstacle," *Journal of Fluids Engineering*, Vol. 105, pp. 461-463.
- Biringen, S. and Reynolds, W., 1981, "Large Eddy Simulation of the Shear Free Turbulent Boundary Layer," *Journal of Fluid Mechanics*, Vol. 103, pp. 53-63.
- Bons, J.P. and Kerrebrock, J.L., 1999, "Complementary Velocity and Heat Transfer Measurements in a Rotating Cooling Passage With Smooth Walls," *Journal of Turbomachinery*, Transactions of ASME, Vol. 121, pp. 651-662.
- Bradshaw, P., 1987, "Turbulent Secondary Flows," *Annual Review of Fluid Mechanics*, Vol. 19, pp. 53-74.
- Cambon, C., Jeandel, D., and Mathieu, J., 1981, "Spectral Modeling of Homogeneous Non-isotropic Turbulence," *Journal of Fluid Mechanics*, Vol. 104, pp. 247-262.
- Chasnov, J., 1991, "On the Decay of Two-Dimensional Homogeneous Turbulence," *Physics of Fluids A*, Vol. 3, pp.188-200.
- Chen, K.H. and Shuen, J.S., 1994, "Three Dimensional Coupled Implicit Methods for Spray Combustion Flows at All Speeds," AIAA Paper 94-3047.
- Choi, H., Moin, P., and Kim, J., 1993, "Direct Numerical Simulation of Turbulent Flow Over Riblets," *Journal of Fluid Mechanics*, Vol. 255, pp. 503-539.
- Choi, Y.H. and Merkle, C.L., 1993, "The Application of Preconditioning in Viscous Flows," *Journal of Computational Physics*, Vol. 105, pp. 207-223.
- Chu, D., Hender, R., and Karniadakis, G., 1992, "Parallel Spectral Element-Fourier Simulation of Turbulence Over Riblet-Mounted Surfaces," *Theoretical Computational Fluid Dynamics*, Vol. 3, pp. 219-229.
- Ciofalo, M., 1994, "Large Eddy Simulation: A Critical Survey of Models and Applications," *Advances in Heat Transfer*, Vol. 25, pp. 321-419.
- Comte, P., Lesieur, M., and Fouillet, Y., 1990, *Topological Fluid Mechanics*, (H.K. Moffatt and A. Tsinober, eds), pp. 649-658, Cambridge University Press, Cambridge.

- Dailey, L.D. and Pletcher, R.H., 1996, "Evaluation of Multigrid Acceleration for Preconditioned Time-Accurate Navier-Stokes Algorithms," *Computer & Fluids*, Vol. 25, pp. 791-811.
- Dailey, L.D., 1997, "Large Eddy Simulation of Turbulent Flows with Variable Property Heat Transfer Using a Compressible Finite Volume Formulation," Doctoral Dissertation, Department of Mechanical Engineering, Iowa State University.
- Dailey, L.D. and Pletcher, R.H., "Large Eddy Simulation of Constant Heat Flux Turbulent Channel Flow With Property Variations," *36th AIAA Aerospace Science Meeting and Exhibit*, Jan. 12-15, Reno, NV, 1998
- Dang, K., 1985, "Evaluation of Simple Subgrid Scale Models for the Numerical Simulation of Homogeneous Turbulence," *AIAA Journal*, Vol. 23, pp. 221-227.
- Dang, K. and Roy, P., 1985a, "Direct and Large Eddy Simulation of Homogeneous Turbulence Submitted to Solid Body Rotation," *Proc. 5th Symposium on Turbulent Shear Flows*, Cornell University, Ithaca, NY, 7-9 August.
- Dang, K. and Roy, P., 1985b, *Microscopic Modeling of Turbulent Flows*, (U. Frisch et al. eds), pp. 134-147, Springer-Verlag, Berlin.
- Deardorff, J., 1970, "A Numerical Study of Three-Dimensional Turbulent Channel at Large Reynolds Number," *Journal of Fluid Mechanics*, Vol. 41, pp. 453-480.
- Demuren, A.O., 1990, "Calculation of Turbulence-Driven Secondary Motion in Ducts With Arbitrary Cross-Section," *AIAA Paper 90-0245*.
- Drain, L.E. and Martin, S., 1985, "Two-Component Velocity Measurement of Turbulent Flow in a Ribbed-Wall Flow Channel," *International Conference on Laser Anemometry Advances and Application*, Manchester, U.K., pp. 99-112.
- Eggels, J., Unger, F., Weiss, M., Westerwheel, J., Adrian, R., Friedrich, R., and Nieuwstadt, F., 1994, "Fully Developed Turbulent Pipe Flow: A Comparison Between Direct Numerical Simulation and Experiment," *Journal of Fluid Mechanics*, Vol. 268, pp. 175-209.
- Erlebacher, G., Hussaini, M.Y., Speziale, C.G., and Zang T.A., 1992, "Toward the Large Eddy Simulation of Compressible Turbulent Flows," *Journal of Fluid Mechanics*, Vol. 238, pp. 155-185.

- Esmaili, H. and Piomelli, U. 1992, Theoretical Computational Fluid Dynamics, Vol. 6, pp. 369.
- Favre, A., 1983, "Turbulence: Space-Time Statistical Properties and Behavior in Supersonic Flows," *Physics of Fluids*, Vol. 26, pp. 2851-2863.
- Feng, J. and Merkle, C.L., 1990, "Evaluation of Preconditioning Methods for Time-Marching Methods," AIAA Paper 90-0016.
- Ferziger, J.H., 1977, "Large Eddy Numerical Simulations of Turbulent Flows," *AIAA Journal*, Vol. 15, pp. 1261-1267.
- Ferziger, J., 1996, "Large Eddy Simulation," *Simulation and Modeling of Turbulent Flows*, (T.B. Gatski, M.Y. Hussaini, and J.L. Lumley, eds), Oxford University Press, New York, 1996, pp. 109-154.
- Friedrich, R. and Arnal, M., 1990, "Drag And Lift on Rectangular Bluff Bodies Immersed in Deep Boundary Layer Flow Over Rough Surfaces," *Journal of Wind Engineering and Industrial Aerodynamics*, Vol. 35, pp. 101-128.
- Friedrich, R. and Su, M., 1982, "Large Eddy Simulation of a Turbulent Wall Bounded Shear Layer with Longitudinal Curvature," *Proc. 8th International Conference on Numerical Methods in Fluid Dynamics*, (E. Krause, ed.), *Lecture Notes in Physics*, Vol. 170, pp.196-202, Springer-Verlag, Berlin.
- Gavrillakis, S., 1992, "Numerical Simulation of Low-Reynolds-Number Turbulent Flow Through a Straight Square Duct," *Journal of Fluid Mechanics*, Vol. 244, pp. 101-129.
- Germano, M., 1986, "A Proposal for a Redefinition of the Turbulent Stresses in Filtered Navier-Stokes Equations," *Physics of Fluids*, Vol. 29, pp. 2323.
- Germano, M., Piomelli, U., Moin, P. and Cabot, W., 1991, "A Dynamic Subgrid-Scale Eddy Viscosity Model," *Journal of Fluid Mechanics*, Vol. 177, pp. 133-166.
- Germano, M., 1992, "Turbulence: the Filtering Approach," *Journal of Fluid Mechanics*, Vol. 238, pp. 325-336.
- Ghosal, R., Lund, T., Moin, P., and Akselvoll, K., 1995, "A Dynamic Localization Model for Large Eddy Simulation of Turbulent Flow," *Journal of Fluid Mechanics*, Vol. 286, pp. 229-255.

- Gilbert, N. and Kleiser, L., 1991, Proc. 8th Symposium on Turbulent Shear Flows, Munich, 9-11 September, 1991.
- Grotzbach, G., 1987, Encyclopedia of Fluid Mechanics, Vol. 6, pp. 1337-1391, (N.R. Chermisinoff, ed.), Gulf Publisher, Houston, TX.
- Guo, Y. and Adams, N., 1994, Proc. 1994 CTR Summer Program, pp. 245-267, NASA Ames/Stanford University.
- Han, J.C., Glicksman, L.R., and Rohsenow, W.M., 1978, "An Investigation of Heat Transfer and Friction for Rib-Roughened Surfaces," International Journal of Heat and Mass Transfer, Vol. 21, pp. 1143-1155.
- Han, J.C., Zhang, Y.M., and Lee, C.P., 1994, "Influence of Surface Heating Condition on Local Heat Transfer in a Rotating Square Channel With Smooth Walls and Radial Outward Flow," Journal of Turbomachinery, Transactions of ASME, Vol. 116, pp. 149-158.
- Hartel, C. and Kleiser, L., 1992, Computational Fluid Dynamics' 92, Vol. 1, pp. 215-222, (C. Hirsch et al. eds), Elsevier Science Publishers, Amsterdam.
- Hartel, C., Kleiser, L., Unger, F. and Friedrich, R., 1994, "Subgrid-Scale Energy Transfer in the Near-Wall Region of Turbulent Flows," Physics of Fluids A, Vol. 6, pp. 3130-3143.
- Hartel, C., 1996, "Turbulent Flows: Direct Numerical Simulation and Large Eddy Simulation," Handbook of Computational Fluid Mechanics, pp. 283-338, Academic Press, San Diego, CA.
- He, J. and Song, C., 1993, Engineering Applications of Large-Eddy Simulations, pp. 147-154, (S.A. Ragab and U. Piomelli, eds), FED, ASME, New York.
- Hopfinger, E., 1989, "Turbulence and Vortices in Rotating Fluids," Theoretical and Applied Mechanics, pp. 117-138, Elsevier.
- Horiuti, K., 1985, "Large Eddy Simulation of Turbulent Channel Flow by One-Equation Modeling," Journal of Physics Society of Japan, Vol. 54, pp. 2855-2865.
- Horiuti, K., 1991, "A New Dynamic Two-Parameter Mixed Model for Large-Eddy Simulation," Physics of Fluids A, Vol. 9, pp. 3443-3462.

- Huser, A. and Biringen, S., 1993, "Direct Numerical Simulation of Turbulent Flow in a Square Duct," *Journal of Fluid Mechanics*, Vol. 257, pp. 65-95.
- Jones, O.C., 1976, "An Improvement in the Calculation of Turbulent Friction in Rectangular Ducts," *Journal of Fluids Engineering*, Vol. 98, pp. 173-181.
- Jordan, S. and Ragab, S., 1993, *Engineering Applications of Large Eddy Simulations*, pp. 127-146, (S.A. Ragab and U. Piomelli, eds), FED, ASME, New York.
- Karniadakis, G., Orszag, S., and Yakhot, V., 1990, *Engineering Turbulence Modeling and Experiments*, pp. 269-278, (W. Rodi and E.N. Ganic, eds), Elsevier Science Publishing Co., New York.
- Kasagi, N., Kuroda, A., and Hirata, M., 1989, "Numerical Investigations of Near-Wall Turbulent Heat Transfer Taking Into Account the Unsteady Heat Conduction in the Solid Wall," *Journal of Heat Transfer*, Vol. 111, pp. 385-392.
- Kim, J., Moin, P., and Moser, R., 1987, "Turbulence Statistics in Fully Developed Channel Flow at Low Reynolds Number," *Journal of Fluid Mechanics*, Vol. 177, pp. 133-166.
- Kim, J., 1983, "The Effect of Rotation on Turbulence Structure," *Proc. 4th Symposium on Turbulent Shear Flows*, Karlsruhe, 12-14 September, 1983.
- Kim, W. and Menon, S., 1997, "Application of the Localized Dynamic Subgrid-Scale Model to Turbulent Wall-Bounded Flows," *AIAA Paper 97-0210*.
- Klein, H. and Friedrich, R., 1990, *Turbulence Control by Passive Means*, pp. 41-65, (E. Coustols, ed.), Kluwer Academic Publishers, Amsterdam.
- Kobayashi, T., Kano, M. and Ishihara, T., 1984, "Prediction of Turbulent Flow in Two-Dimensional Channel With Turbulence Promoters," (3rd report, Numerical Prediction by $k-\varepsilon$ Model and Comparison With Experimental Results), *Bulletin of JSME*, Vol. 28, pp.2940-2947.
- Kral, L. and Zang, T., 1992, *Transitional and Turbulent Compressible Flows*, pp. 151, FED, ASME, New York.
- Kristoffersen, R. and Andersson, I., 1993, "Direct Simulations of Low-Reynolds-Number Turbulent Flow in Rotating Channel," *Journal of Fluid Mechanics*, Vol. 256, pp. 163-197.

- Laurence, D., 1986, Direct and Large Eddy Simulation of Turbulence, Vol. 15, pp. 147-160, (U. Schumann and R. Friedrich, eds), Notes on Numerical Fluid Mechanics, Vieweg-Verlag, Branschweig.
- Lee, D.L. and van Leer, B., 1993, "Progress in Local Preconditioning for the Euler and Navier-Stokes Equations," AIAA Paper 93-3328-CP.
- Leith, C., 1990, "Stochastic Backscatter in a Subgrid Scale Model: Plane Shear Mixing Layer," Physics of Fluids A, Vol. 2, pp. 297-299.
- Leonard, A., 1974, "Energy Cascade in Large Eddy Simulations of Turbulent Flows," Advances in Geophysics, Vol. 18A, pp. 237-248.
- Lesieur, M. and Rogallo, R., 1989, "Large Eddy Simulation of Passive Scalar Diffusion in Isotropic Turbulence," Physics of Fluids A, Vol. 1, pp. 718-722.
- Lilly, D., 1966, "On the Application of the Eddy Viscosity Concept in the Inertial Subrange of Turbulence," Report NCAR-123, National Center for Atmospheric Research, Boulder, Co.
- Liu, S., Meneveau, C., and Katz, J., 1994, "On the Properties of Similarity Subgrid-Scale Models As Deduced From Measurements in a Turbulent Jet," Journal of Fluid Mechanics, Vol. 275, pp. 83-119.
- Lumley, J.L., 1996, "Turbulence and Turbulence Modeling," Research Trends in Fluid Dynamics, pp. 167-177, American Institute of Physics Press, Woodbury, NY.
- Mansour, N., Ferziger, J., and Reynolds, W., 1978, "Large Eddy Simulation of a Turbulent Mixing Layer," Report No. TF-11, Department of Mechanical Engineering, Stanford University.
- Marayuma, Y., 1988, Trans. Jap. Soc. Aeronaut. Space Sci., Vol. 31, pp. 79-93.
- Mason, P. and Callen, N., 1986, "On the Magnitude of the Subgrid-Scale Eddy Coefficient in Large-Eddy Simulations of Turbulent Channel Flow," Journal of Fluid Mechanics, Vol. 162, pp. 439-462.
- Mason, P. and Thomson, D.J., 1992, "Stochastic Backscatter in Large Eddy Simulation of Boundary Layers," Journal of Fluid Mechanics, Vol. 242, pp. 51-78.

- Matsubara, M. and Alfreson, P. H., "Experiment Study of Heat and Momentum Transfer in Rotating Channel Flow," *Physics of Fluids A*, Vol. 8, pp. 2964-2973.
- Meneveau, C., Lund, T. and Cabot, W., 1996, "Lagrangian Dynamic Subgrid-Scale Model of Turbulence," *Journal of Fluid Mechanics*, Vol. 319, pp. 353-385.
- Meneveau, C. and Katz, J., 2000, "Scale-Invariance and Turbulence Models for Large-Eddy Simulation," *Annual Review of Fluid Mechanics*, 2000, pp. 1-32.
- Meng, N., Pletcher, R. and Dailey, L., 1999, "Compressible Large Eddy Simulation for Turbulent Channel Flow With Constant Heat Flux," AIAA Paper 99-3356, 14th AIAA Computational Fluid Dynamics Conference. June 29-July 2, 1999, Norfolk, VA.
- Meng, N., 2000, "Large Eddy Simulation of Turbulent Flows with Property Variation, Rotation and Complex Geometry," Ph.D. Dissertation, Department of Mechanical Engineering, Iowa State University.
- Meng, N. and Pletcher, R.H., 2000a, "Large Eddy Simulation of Rotating Channel Flows With and Without Heat Transfer," *Proceedings of the ASME Heat Transfer Division 2000*, Vol. 5, pp. 213-224.
- Metais, O. and Lesieur, M., 1992, "Spectral Large Eddy Simulation of Isotropic and Stably Stratified Turbulence," *Journal of Fluid Mechanics*, Vol. 239, pp. 157-194.
- Moin, P. and Kim, J., 1982, "Numerical Investigation of Turbulent Channel Flow," *Journal of Fluid Mechanics*, Vol. 118, pp.341-377.
- Moin, P., Squires, K., Cabot, W. and Lee, S., 1991, "A Dynamic Subgrid-Scale Model for Compressible Turbulence and Scalar Transport," *Physics of Fluids*, Vol. 3, pp. 2746-2757.
- Moin, P., Carati, D., Lund, T., Ghosal, S. and Akselvoll, K., 1994, Application of Direct and Large Eddy Simulation to Transition and Turbulence, AGARD-CP-551, AGARD, Neuilly-sur-Seine.
- Moin, P., 1996, "Direct and Large Eddy Simulation of Turbulence", *Research Trends in Fluid Dynamics*, pp. 188-193, American Institute of Physics Press, Woodbury, NY.

- Moore, J., 1967, "Effects of Coriolis on Turbulent Flow in Rotating Rectangular Channels," Gas Turbine Laboratory Report, Massachusetts Institute of Technology, Cambridge, MA.
- Morinishi, Y. and Kobayashi, T., 1990, Engineering Turbulence Modeling and Experiments, pp. 279-286, (W. Rodi and E.N. Ganic, eds), Elsevier Science Publishing Co. New York.
- Murata, A. and Mochizuki, S., 2000, "Large Eddy Simulation With a Dynamic Subgrid-Scale Model of Turbulent Heat Transfer in An Orthogonally Rotating Rectangular Duct With Transverse Rib Turbulators," International Journal of Heat and Mass Transfer, Vol. 43, pp. 1243-1259.
- Murata, A. and Mochizuki, S., 2001, "Large Eddy Simulation of Turbulent Heat Transfer in An Orthogonally Rotating Square Duct With Angled Rib Turbulators," Journal of Heat Transfer, Vol. 123, pp. 858-867.
- Neves, J., Moin, P., and Moser, R., 1992, "Numerical Study of Axial Turbulent Flow Over Long Cylinders," Report No. TF-54, Department of Mechanical Engineering, Stanford University.
- Nicoud, F., 1998, "Numerical Study of a Channel Flow With Variable Properties," Annual Research Briefs, Center for Turbulence Research, 00. 289-310, Stanford University.
- O'Sullivan, P., Biringen, S., and Huser, A., 1998, "DNS/LES of Turbulent Flow in a Square Duct: A Priori Evaluation of Subgrid Models," Industrial and Environmental Applications of Direct and Large Eddy Simulation, Proceedings of a Workshop Held in Istanbul, Turkey, 5-7 August 1998, Lecture Notes in Physics, Springer, Berlin, pp. 290-301.
- Pallares, J. and Davidson L., 2000, "Large Eddy Simulation of Turbulent Flows in Stationary and Rotating Channel And in a Stationary Square Duct," Report No.00/3, Department of Thermo and Fluid Dynamics, Chalmers University of Technology, Sweden.
- Pallares, J. and Davidson L., 2000, "Large Eddy Simulation of Turbulent Flows in a Square Duct," Physics of Fluids, Vol. 12, pp. 2878-2894.
- Piomelli, U., Cabog, W., Moin, P., and Lee, S., 1991, "A Dynamic Subgrid-Scale Eddy Viscosity Model," Physics of Fluids A, Vol. 3(7), pp. 1766-1771.

- Piomelli, U. and Liu, J., 1995, "Large Eddy Simulation of Rotating Channel Flow Using a Localized Dynamic Model", *Physics of Fluids*, Vol. 7(4), pp. 839-848.
- Pletcher, R.H. and Chen, K.H., 1993, "On Solving the Compressible Navier-Stokes Equations for Unsteady Flows at Very Low Mach Numbers," AIAA paper 93-3368.
- Pourquie, M. and Eggels, J., 1993, *Engineering Applications of Large Eddy Simulations*, Vol. 162, pp. 37-44, (S.A. Ragab and U. Piomelli, eds), FED, ASME, New York.
- Prandtl, L., 1926 *Über die ausgebildete Turbulenz*, *Berh. 2nd Intl Kong. für Tech. Mech.*, Zurich. [English Translation NACA Technical Memo. Vol. 435, pp. 62]
- Ragab, S. and Sheen, S., 1991, AIAA paper 91-0233, AIAA 29th Aerospace Sciences Meeting, Reno, NV.
- Salvetti, M. and Banerjee, S., 1995, "A priori Tests of a New Dynamic Subgrid-Scale Model for Finite Difference Large Eddy Simulations," *Physics of Fluids A*, Vol. 7, pp. 2831-2847.
- Sarghini, F., Piomelli, U., and Balaras, E., 1999, "Scale-Similar Models for Large Eddy Simulations," *Physics of Fluids A*, Vol. 11, pp. 1596-1607
- Schmitt, L. and Friedrich, R., 1984, *Proc. 5th GAMM Conference on Numerical Methods in Fluid Mechanics*, (M. Pandolfi and R. Riva, eds), pp. 399-406. *Notes on Numerical Fluid Mechanics*, Vol. 7, Vieweg-Verlag, Braunschweig.
- Schumann, U., 1973, "Ein Verfahren zur direkten numerischen Simulation turbulenter Strömungen in Platten und Ringspaltkanälen und über Seine Anwendung zur Untersuchung von Turbulenzmodellen," Doctoral Dissertation, Technical Univ. of Karlsruhe, Germany.
- Schumann, U., 1975, "Subgrid Scale Model for Finite Difference Simulations of Turbulent Flows in Plane Channels and Annuli," *Journal of Computational Physics*, Vol. 18, pp. 376-404.
- Sheen, S., Sreehar, M., and Ragab, S., 1993, *Engineering Applications of Large Eddy Simulations*, Vol. 162, pp. 53-64, (S.A. Ragab and U. Piomelli, eds), FED, ASME, New York.

- Silveira Neto, A., Grand, D., and Lesieur, M., 1991, "Large Eddy Simulation of the Turbulent Flow in the Downstream Region of a Backward Facing Step," *Physics Review Letter*, Vol. 66, pp. 2320-2323.
- Smagorinsky, J., 1963, "General Circulation Experiments With the Primitive Equations: Part I. The Basic Experiment," *Monthly Weather Review*, Vol. 91, pp. 99-164.
- Spalart, P. and Watmuff, U., 1993, "Experimental and Numerical Study of a Turbulent Boundary Layer with Pressure Gradients," *Journal of Fluid Mechanics*, Vol. 249, pp.337-371.
- Spalart, P., 1988, "Direct Numerical Simulation of Turbulent Boundary Layer Up To Re_θ Equals 1410," *Journal of Fluid Mechanics*, Vol. 187, pp.61-98.
- Sparrow, E.M. and Tao, W.Q., "Enhanced Heat Transfer in a Flat Rectangular Duct With Streamwise-Periodic Disturbances at One Principal Wall," *Transactions of ASME, Journal of Heat Transfer*, Vol. 105, pp. 851-861.
- Speziale, C.G., 1985, "Galilean Invariance of Subgrid-Scale Stress Models in the Large Eddy Simulation of Turbulence," *Journal of Fluid Mechanics*, Vol. 156, pp. 55-62.
- Spyropoulos, E.T. and Blaisdell, G.A., 1995, "Evaluation of the Dynamic Subgrid-Scale Model for Large Eddy Simulations of Compressible Turbulent Flows," *AIAA Paper 95-0355*.
- Squires, K., 1993, *Engineering Applications of Large-Eddy Simulations*, Vol. 162, pp. 65-71, (S.A. Ragab and U. Piomelli, eds), FED, ASME, New York.
- Su, M. and Friedrich, R., 1994, "Investigation of Fully Developed Turbulent Flow in a Straight Duct With Large Eddy Simulation," *Journal of Fluids Engineering*, Vol. 116, pp.677-684.
- Su, M. and Friedrich, R., 1994a, "Numerical Simulation of Fully Developed Flow in a Curved Duct of Rectangular Cross-Section," *International Journal of Heat and Mass Transfer*, Vol. 37, pp. 1257-1268.
- Taslim, M.E., Rahman, A., and Spring, S.D., 1991, "An Experimental Investigation of Heat Transfer Coefficients in a Spanwise Rotating Channel with Two Opposite Rib-Roughened Walls," *Journal of Turbomachinery*, Vol.113, pp. 75-82.

- Tennekes, H. and Lumley, J., 1972, *A First Course in Turbulence*, MIT Press, Cambridge, MA.
- Tritton, D., 1978, "Turbulence in Rotating Fluids," *Rotating Fluids in Geophysics*, pp. 105-138, Academic Press.
- Tritton, D., 1985, "Experiments on Turbulence in Geophysical Fluid Dynamics," *Turbulence and Predictability in Geophysical Fluid Dynamics and Climate Dynamics*, pp. 172-192, North Holland.
- Turkel, E., 1987, "Preconditioned Methods for Solving the Incompressible and Low Speed Compressible Equations," *Journal of Computational Physics*, Vol. 72, pp. 277-298.
- Turkel, E., 1992, "Review of Preconditioning Methods for Fluid Dynamics," NASA-CR-189712 or ICASE Report No. 92-47.
- Unger, F. and Friedrich, R., 1993, *Flow Simulation With High Performance Computers I*, pp. 38, (E.H. Hirschel, ed.), Notes on Numerical Fluid Mechanics, Vieweg-Verlag, Braunschweig.
- Van Driest, E.R., 1951, "Turbulent Boundary Layer in Compressible Fluids," *Journal of Aeronautical Science*, Vol. 18, pp. 145-160.
- Voke, P. and Gao, S., 1993, *Engineering Applications of Large Eddy Simulations*, Vol. 162, pp. 29-35, (S.A. Ragab and U. Piomelli, eds), FED, ASME, New York.
- Vremen, A., Geurts, B.J. and Kuerten, J., 1994, *Direct and Large-Eddy Simulations I*, pp. 133-144, (P.R. Voke et al. eds), Kluwer Academic Publishers, Dordrecht.
- Vremen, A., Geurts, B.J. and Kuerten, J., 1995, "Subgrid-Modeling in LES of Compressible Flow," *Applied Scientific Research*, Vol. 54, pp. 191-203.
- Wagner, C. and Friedrich, R., 1994, "Turbulent Flow in a Sudden Pipe Expansion," *Proceedings of the 1994 5th European Turbulence Conference*, Jul 5-8 1994, Siena, Italy, p 544.
- Wagner, J.H., Johnson, B.V., Graziani, R.A. and Yeh, F.C., 1992, "Heat Transfer in Rotating Serpentine Passage with Trips Normal to the Flow," *Journal of Turbomachinery*, Vol. 114, pp. 847-857.

- Wang, W. and Pletcher, R., 1996, "On the Large Eddy Simulation of a Turbulent Channel Flow With Significant Heat Transfer," *Physics of Fluids*, Vol. 8, pp. 3354-3366.
- Werner, H. and Wengle, H., 1989, *Advances in Turbulence 2*, pp. 418-423, (H.J. Fernholz and H.E. Fiedler, eds), Springer-Verlag, Berlin.
- Werner, H. and Wengle, H., 1993, *Turbulent Shear Flows*, pp. 155-168, (F. Durst et al. eds), Springer-Verlag, Berlin.
- Withington, J.P., Shuen, J.S., and Yang, V., 1991, "A Time Accurate, Implicit Method for Chemically Reacting Flows at all Mach Numbers," AIAA Paper 91-0581.
- Yakhot, A., Orszab, S., Yakhot, V., and Israeli, M., 1989, *Journal of Scientific Computing*, Vol. 4, pp. 139-158.
- Yang, K. and Ferziger, J., 1993, "Large Eddy Simulation of Turbulent Obstacle Flow Using Dynamic Subgrid-Scale Model," *AIAA Journal*, Vol. 31, pp. 1406-1413.
- Yoon, S. and Jameson, A., 1987, "An LU-SSOR Scheme for the Euler and Navier-Stokes Equations," AIAA Paper 87-600.
- Yoshizawa, A., 1986, "Statistical Theory for Compressible Turbulent Shear Flows, With the Application to Subgrid Modeling," *Physics of Fluids A*, Vol. 29, pp. 2152-2164.
- Zang, Y., Street, R. and Koseff, J., 1993, "A Dynamic Mixed Subgrid Scale Model and Its Application to Turbulent Recirculating Flows," *Physics of Fluids A*, Vol. 12, pp. 3186-3196.

ACKNOWLEDGEMENTS

It is with many people's help that this thesis can come into being. With this opportunity, I would like to express my gratitude to all those who have been so indispensable and invaluable to various aspects of my research, study and life in Ames.

First and the most important, Dr. Pletcher for his patient guidance and incisive directions. As my major professor, his insights and encouragement have constantly provided me with renewed inspiration and desire to achieve. As a friend, the talk between us is always lively and constructive. His example as a scholar and person of excellence will guide throughout my life.

I would also like to thank my committee to their efforts and contributions to my study and this thesis work: Drs. John Tannehill, Gerald Colver, and Gary Tuttle.

As the departure to the unforgettable time down in 95D of Black Engineering Building approaches, I want to say thanks to my colleagues who made this happy period possible: Ravikanth Avancha, Joonsang Lee, Xiaofeng Xu, Steve Sass, Chunjian Ni, Anup Gokarn, Nan Xie, John Mammoser, Farshid Bondar and Kunlun Liu. Our discussions about research, science, life and the future were always insightful, intriguing and humorous.

Special thanks go to Lyle Dailey and Ning Meng, who built the framework of my research. A lot of my knowledge and skills come from their publications and code.

A lot of computer resources were consumed to conduct and finish the research, majority of which are from IBM SP2 and SGI Origin 3800 at Minnesota Supercomputer Center at University of Minnesota. The generous help in providing constant computing facility is vital to this work. High-Performance Computing Partnership at Iowa State University also provides valuable assistance. Resources

were also used at San Diego supercomputer center of National Partnership for Advanced Computational Infrastructure.

The funding of this research was from Air Force Office of Scientific Research under Grants F49620-00-1-0229 and F49620-01-1-0113. Their support is gratefully acknowledged.

Last, but not the least, the encouragement across the Pacific Ocean from my parents, Yunchang Liu and Zhongyuan Sun, is highly appreciated. Their love for me has been and will always be part of my motivation to make more contributions in my life.